

Study of Quark-Gluon Plasma by Measuring the Upsilon Production in p-Pb and Pb-Pb Collisions at Forward Rapidity with ALICE at the LHC

by

Palash Khan

PHYS05200904002

**Saha Institute of Nuclear Physics
Kolkata, India**

*A thesis submitted to the
Board of Studies in Physical Sciences
In partial fulfillment of requirements
for the Degree of*

DOCTOR OF PHILOSOPHY

of

HOMI BHABHA NATIONAL INSTITUTE



February, 2015



Homi Bhabha National Institute

Recommendations of the Viva Voce Committee

As members of the Viva Voce Committee, we certify that we have read the dissertation prepared by Palash Khan entitled "Study of Quark-Gluon Plasma by Measuring the Upsilon Production in p-Pb and Pb-Pb Collisions at Forward Rapidity with ALICE at the LHC" and recommend that it may be accepted as fulfilling the thesis requirement for the award of Degree of Doctor of Philosophy.



Date : 22/07/15

Chairman : Prof. Pradip Kumar Roy, SINP



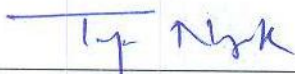
Date : 22/07/15

Guide & Convener : Prof. Sukalyan Chattopadhyay, SINP



Date : 22/7/2015

Examiner : Prof. Shashikant Dugad, TIFR



Date : 22/7/2015

Member : Prof Tapan Kumar Nayak, VECC



Date : 22/7/2015

Member : Prof. Debasish Das, SINP

Final approval and acceptance of this thesis is contingent upon the candidate's submission of the final copies of the thesis to HBNI.

I hereby certify that I have read this thesis prepared under my direction and recommend that it may be accepted as fulfilling the thesis requirement.

Date : 22/07/15

Place : KOLKATA


Guide

STATEMENT BY AUTHOR

This dissertation has been submitted in partial fulfillment of requirements for an advanced degree at Homi Bhabha National Institute (HBNI) and is deposited in the Library to be made available to borrowers under rules of the HBNI.

Brief quotations from this dissertation are allowable without special permission, provided that accurate acknowledgement of source is made. Requests for permission for extended quotation from or reproduction of this manuscript in whole or in part may be granted by the Competent Authority of HBNI when in his or her judgment the proposed use of the material is in the interests of scholarship. In all other instances, however, permission must be obtained from the author.

PALASH KHAN

DECLARATION

I, hereby declare that the investigation presented in the thesis has been carried out by me. The work is original and has not been submitted earlier as a whole or in part for a degree / diploma at this or any other Institution / University.

PALASH KHAN

*“To follow knowledge like a sinking star,
Beyond the utmost bounds of human thought.”*

Alfred Lord Tennyson

Dedicated to My Parents

ACKNOWLEDGEMENTS

The golden five years of my research career is almost at the end. It feels nostalgic when I look back to have a glimpse of these years. I still remember the long friendly discussion at the very first day when I met my supervisor Prof. Sukalyan Chattopadhyay. Sukalyan Da is not only a super guide, but also a beautiful human being. I feel elated to have worked with him and my reverence towards him will remain forever. He gave complete freedom to think, work and develop. I look forward to carry those values in my life. Without his constant courage and support this thesis work would not have been possible to accomplish.

Life was beautiful both at SINP and at CERN. I found it very enjoyable to work at SINP. During the infant stages of my thesis work Indranil Da helped me a lot, both at SINP and at CERN, irrespective of whether it was academic or non-academic. I am very much thankful to him. I am also thankful to Kushal Da, Debasish Da, Tinku Di and Biswarup for their continuous support throughout my thesis work. I would like to convey my sincere thanks to Prof. Pradip Kumar Roy, Prof. Abhee Kanti Dutt-Mazumder, Prof. Sunanda Banerjee and Prof. Tapan Kumar Nayak for extending their hand of support whenever needed. It was my pleasure to work with Cynthia Hadjidakis for my first analysis work on QA. I am thankful to her for the important suggestions and feed backs at every stage of my QA analysis. I would like to express my sincere gratitude to Diego Stocco for his valuable suggestions at various stages of my thesis work. I stayed at Gif-

sur-Yvette, in the south-western suburbs of Paris, for around a month working on alignment and Upsilon analysis. During those days I learned a lot working with Javier Castillo. I am thankful to him for the things I learned from him and for accommodating me a very comfortable stay at Gif-sur-Yvette. I feel privileged to be able to work in a project like LHC. The complex experiment work there really took off many wraps of knowledge to me. I cordially loved the work culture and work environment of CERN.

The support from my family members was beyond words. I am specially to my Mom, Dad, Bilas and Payel for their continuous support and encouragement. Without their support and encouragement the thesis work would not have been possible to accomplish. Last but not the least, I express my sincere gratitude to all my friends and colleagues whom I have missed to mention in this page. It is for all of them that I must have “to strive, to seek, to find, and not to yield”.

Palash Khan

18 February, 2015

SYNOPSIS

In the Standard Model of particle physics the interaction between quarks and gluons are described by a theory called quantum chromodynamics (QCD). QCD predicts that at very high temperature and energy density the hadronic matter can undergo a phase transition and can turn into a state of deconfined quarks and gluons known as Quark-Gluon Plasma (QGP). This state of matter can be created by colliding two large nuclei at ultra-relativistic energies. In such collisions, heavy flavors, specially charm and bottom, are produced at the very early stage by the hard scattering and hence can be used to characterize the hot and dense medium. It is predicted that the production of quarkonia (charmonia and bottomonia) in nucleus-nucleus collisions will be suppressed relative to that in proton-proton due to the Color-Debye Screening mechanism. In particular, a sequential suppression of quarkonia, depending on their binding energy has been proposed as a thermometer of the deconfined medium.

The suppression of quarkonia can be quantified by measuring the nuclear modification factor R_{AA} , which is the ratio of yield in nucleus-nucleus collisions to that in proton-proton collisions scaled by the number of binary collisions. The suppression of quarkonium states depends on several factors, as the feed-down contributions from higher-mass resonances into the observed quarkonium yield, the b-hadrons decay into charmonium and the quarkonium regeneration due to the $q\bar{q}$ recombination (expected to be important for $c\bar{c}$ pairs at LHC energies). Other important competing mechanisms are the Cold Nuclear Matter (CNM) effects, such

as nuclear shadowing or gluon saturation, which can break the binary scaling even in absence of the QGP. Hence, for the interpretation of results in heavy-ion collisions, data from pA are crucial since they allow to disentangle the CNM effects from those related to the formation of a hot medium. With this goal in mind, the ALICE collaboration has measured the $\Upsilon(1S)$ production in Pb-Pb collisions at $\sqrt{s_{NN}} = 2.76$ TeV and p-Pb collisions at $\sqrt{s_{NN}} = 5.02$ TeV. For p-Pb, data were taken with two beam configurations corresponding to the proton going towards or opposite to the direction of the muon spectrometer.

There are four main physics experiments ALICE, ATLAS, CMS and LHCb currently going on the LHC accelerator. The result presented in the thesis is from the analysis of the data obtained from the forward Muon Spectrometer of ALICE. The forward Muon Spectrometer is in the rapidity range $2.5 < y < 4$ and can measure a wide range of transverse momentum down to $p_T = 0$. Its main goal is to study the charmonium (J/ψ and $\psi(2S)$) and bottomonium (Υ resonances), low mass vector mesons (ρ and ϕ), open heavy-flavours (D and B families) and weak bosons (Z , W^\pm), via their muonic decay channels in pp, pA and AA collisions at the LHC energies.

The Muon Spectrometer has a total length of 17 m and covers the polar angular range $172^\circ < \theta < 178^\circ$ ($4.0 < \eta < 2.5$) with respect to the ALICE reference frame. It is composed of absorbers, five stations of tracking detectors that, together with a warm dipole magnet, are used to track muons and to measure their momenta and two stations of trigger chambers shielded by a muon filter.

The following important results which will be reported in the thesis:

(A) Results from 2011 Pb–Pb run at $\sqrt{s_{\text{NN}}} = 2.76$ TeV:

- $\Upsilon(1S)$ R_{AA} versus centrality
- $\Upsilon(1S)$ R_{AA} versus rapidity
- Comparison to model predictions

(B) Results from 2013 p–Pb and Pb–p run at $\sqrt{s_{\text{NN}}} = 5.02$ TeV:

- $\Upsilon(1S)$ R_{pPb} at forward and backward rapidity
- Forward Backward Ratio (R_{FB}) for $\Upsilon(1S)$
- Comparison to model predictions

In Pb–Pb collisions, the inclusive $\Upsilon(1S)$ nuclear modification factor at $\sqrt{s_{\text{NN}}} = 2.76$ TeV has been measured down to $p_{\text{T}} = 0$ in the $2.5 < y < 4$ rapidity and 0%–90% centrality ranges for a data sample corresponding to an integrated luminosity of $L_{\text{int}} = 69.2 \mu\text{b}^{-1}$. We obtained $R_{\text{AA}}^{0\%-90\%} = 0.30 \pm 0.05(\text{stat.}) \pm 0.02(\text{uncorr.}) \pm 0.04(\text{corr.})$ corresponding to a strong suppression of inclusive $\Upsilon(1S)$. Two centrality ranges were studied and the suppression is more pronounced in most central collisions. The R_{AA} was also measured in two rapidity bins and, within uncertainties, no significant rapidity dependence was observed in the range probes by the ALICE muon spectrometer.

The data were compared with the ALICE J/ψ results obtained in the same kinematic range. The $\Upsilon(1S)$ is more suppressed than the J/ψ and the difference of R_{AA} is particularly pronounced in the 0%–20% ($2.5 < y < 3.2$) centrality (rapidity) bin.

The interpretation of these results is not straightforward due to the different sizes of the expected feed-down and (re-)generation effects for the two quarkonium states.

The $\Upsilon(1S)$ R_{AA} was also compared with CMS data measured in the $|y| < 2.4$ rapidity region and down to $p_T = 0$ as shown in Figure- 1. The inclusive $\Upsilon(1S)$ yield measured at forward rapidity by ALICE is more suppressed than that measured at mid-rapidity by CMS.

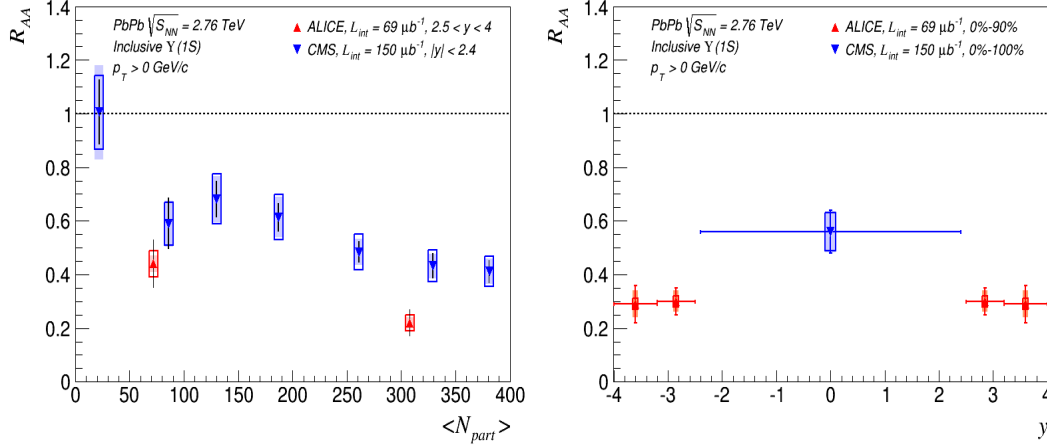


Figure 1: Left (Right): ALICE and CMS nuclear modification factor of inclusive $\Upsilon(1S)$ production as a function of the average number of participant nucleons (rapidity). Bars stand for statistical uncertainties and filled (open) boxes uncorrelated (correlated) for uncertainties. On the right plot, open points are reflected with respect to the measured ones.

A better understanding of Υ production in AA collisions requires a precise measurement of feed-down from higher mass bottomonia and CNM effects at forward rapidity. For this reason in 2013 data has been taken in p-Pb and Pb-p collisions.

In case of p-Pb and Pb-p the inclusive $\Upsilon(1S)$ R_{pPb} was measured at forward ($2.04 < y_{cms} < 3.54$) and backward rapidity ($-4.46 < y_{cms} < -2.96$) for a data sample corresponding to an integrated luminosity of $L_{int} = 5.3 \text{ nb}^{-1}$ (for p-Pb) and 6.1 nb^{-1} (for Pb-p) respectively.

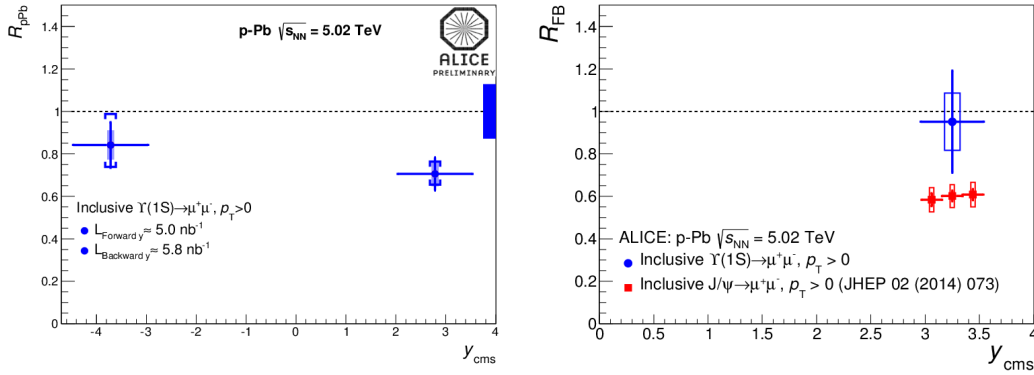


Figure 2: (Left) Inclusive $\Upsilon(1S)$ nuclear modification factor evolution as a function of y_{cms} . (Right) Forward to backward ratio R_{FB} of inclusive $\Upsilon(1S)$ yields compared to the J/ψ R_{FB} . The vertical error bars represent the statistical uncertainties and the open boxes the uncorrelated systematic uncertainties.

At forward rapidity, R_{pPb} shows a suppression of $\Upsilon(1S)$ production in p-Pb compared to pp collisions. At backward rapidity, the $\Upsilon(1S)$ R_{pPb} is consistent with unity, suggesting a small gluon anti-shadowing. The forward to backward ratio R_{FB} of the inclusive $\Upsilon(1S)$ yields in $2.96 < |y_{cms}| < 3.53$ is compatible with unity within large uncertainties as shown in Figure- 5.9. Within our uncertainties, the measured $[\Upsilon(2S)/\Upsilon(1S)]$ ratio shows no evidence of different CNM effects on the two states. Additional measurements with higher statistics are needed to further constrain the CNM effects to Pb-Pb collisions.

The thesis is composed of seven chapters and these are as follows,

Chapter 1. The Quark-Gluon Plasma (QGP) :

In this chapter the general understanding of the Quark-Gluon Plasma (QGP) from the view point of Quantum Chromodynamics (QCD) will be explained. The possible observables QGP in context of ALICE experiment will also be discussed.

Chapter 2. ALICE Experiment at the LHC :

This will describe different detectors of ALICE with specific emphasis on

Muon Spectrometer. The detector layout, data taking and analysis framework will be discussed in some details.

Chapter 3. Data Quality Assurance (QA) :

Only the QA checked data are used for the physics analysis in ALICE. Some general trends are checked to understand and validate the data during QA test. In this chapter the methods of the QA will be discussed.

Chapter 4. Upsilon (Υ) Production in Pb–Pb Collisions :

In this chapter the analysis of Υ production in Pb-Pb collisions in ALICE will be discussed. The data analyzed is at forward rapidity ($2.5 < \eta < 4$) region at $\sqrt{s_{NN}} = 2.76$ TeV. The inclusive nuclear modification factor R_{AA} of $\Upsilon(1S)$ in Pb–Pb collisions as a function of centrality and rapidity will be shown. The results will also be compared to the measurement at midrapidity by CMS and to theoretical predictions.

Chapter 5. Upsilon (Υ) Production in p–Pb Collisions :

To understand the Cold Nuclear Matter effect (CNM), the ALICE experiment has measured the $\Upsilon(1S)$ production in the p-Pb collisions at $\sqrt{s_{NN}} = 5.02$ TeV . The measurement is performed at forward rapidity ($2.04 < y_{CM} < 3.54$) and backward rapidity ($-4.46 < y_{CM} < -2.96$) as a function of the rapidity. The ratio of the nuclear modification factors R_{pPb} at forward rapidity and backward rapidity and forward to backward yield ratio (R_{FB}) has also been studied. In this chapter, the results are discussed and compared with the ALICE J/ψ data at forward and backward rapidity and with the available theoretical predictions.

Chapter 6. Summary and Outlook :

Summary of the thesis, prospects and future direction.

List of Publications Arising from the Thesis

Journal:

1. Suppression of $\Upsilon(1S)$ at forward rapidity in Pb–Pb collisions at $\sqrt{s_{NN}} = 2.76$ TeV, B. Abelev et al. [ALICE Collaboration], Phys. Lett. B **738** (2014) 361-372 [arXiv:1405.4493 [nucl-ex]].
2. Production of $\Upsilon(1S)$ and $\Upsilon(2S)$ in p–Pb collisions at $\sqrt{s_{NN}} = 5.02$ TeV, B. Abelev et al. [ALICE Collaboration], Phys. Lett. B **740** (2015) 105-117 [arXiv:1410.2234 [nucl-ex]].

Conferences:

1. Υ Production in Pb–Pb and p–Pb Collisions at Forward Rapidity with ALICE at the LHC, Palash Khan for the ALICE Collaboration, 14th International Conference on Strangeness in Quark Matter (SQM2013), Journal of Physics: Conference Series **509** (2014) 012112 [arXiv:1310.2565 [nucl-ex]].
2. Υ Production in Pb–Pb Collisions at Forward Rapidity with ALICE at the LHC, Palash Khan and Sukalyan Chattopadhyay for the ALICE Collaboration, DAE Symposium on Nuclear Physics, Vol 58 (2013), p. 790.
3. Υ Production in p–Pb Collisions at Forward Rapidity with ALICE at the LHC, Palash Khan and Sukalyan Chattopadhyay for the ALICE Collaboration, DAE Symposium on Nuclear Physics, Vol 58 (2013), p. 792.

Others:

1. Measurement of the $\Upsilon(1S)$ R_{AA} in Pb–Pb collisions at $\sqrt{s_{NN}} = 2.76$ TeV with the ALICE muon spectrometer, Francesco Bossu, Palash Khan, Loic Manceau, Massimiliano Marchisone, ANA-640, CERN-PH-EP-2014-103, [<https://aliceinfo.cern.ch/Notes/node/155>].
2. Production of $\Upsilon(1S)$ at forward rapidity in Pb–Pb collisions at $\sqrt{s_{NN}} = 2.76$ TeV, B. Abelev et al. [ALICE Collaboration], PUB-753, CERN-PH-EP-2014-103, [<https://aliceinfo.cern.ch/Notes/node/172>].
3. Production of $\Upsilon(1S)$ and $\Upsilon(2S)$ in p–Pb collisions at $\sqrt{s_{NN}} = 5.02$ TeV, Francesco Bossu, Martino Gagliardi, Palash Khan, Loic Manceau, ANA-909, CERN-PH-EP-2014-196, [<https://aliceinfo.cern.ch/Notes/node/192>].

List of Tables

1.1	Quarkonium binding energies (ΔE), quark distance (r_0) and dissociation temperatures in units of T_c [18].	16
4.1	Average number of binary collisions, average number of participant nucleons and nuclear overlap function for the various centrality classes considered in this analysis [5].	94
4.2	The fit results for different centrality and rapidity bins.	98
4.3	The results of signal extraction. Central values and statistical uncertainties are the average of the results obtained for each study. Systematic uncertainties from each source were summed in quadrature. Overall statistical (systematic) uncertainties range between 15% – 23% (5% – 11%).	100
4.4	The yields of $\Upsilon(1S)$ per unit of rapidity obtained in Pb-Pb collisions at $\sqrt{s_{NN}} = 2.76$ TeV for each centrality and rapidity range. Uncorrelated (correlated) systematic uncertainties are quoted as uncorr. (corr.).	102
4.5	$A \times \epsilon$ values for the centrality and rapidity bins considered in the present analysis.	105

4.6	Extended Crystal Ball tail parameters for the centrality and rapidity bins considered in this analysis.	106
4.7	Experimental results used for the interpolation of the $\Upsilon(1S)$ cross-section at mid-rapidity.	109
4.8	Combined results for $\frac{d\sigma_Y}{dy}$ (nb) in pp collisions at $\sqrt{s} = 2.76$ TeV at forward rapidity. The uncertainty on the normalization (Norm.) is quoted separately from the one related to the spread between the extrapolated values at forward rapidity (Extr.).	115
4.9	Inclusive $\Upsilon(1S)$ cross-section in pp collisions at $\sqrt{s} = 2.76$ TeV from LHCb [21] in various rapidity bins at forward rapidity.	116
4.10	Inclusive $\Upsilon(1S)$ cross-section per unit of rapidity in pp collisions at $\sqrt{s} = 2.76$ TeV obtained from the rapidity interpolation of LHCb data [21]. This result is 30% to 35% higher than data-driven method (Table 4.8). Results do not include the branching ratio of $\Upsilon(1S)$ decay to dimuon.	117
4.11	Summary of statistical uncertainties.	117
4.12	Summary of systematic uncertainties.	118
4.13	Summary of systematic uncertainties for various bins.	118
4.14	Values of the R_{AA} measured in Pb-Pb collisions at $\sqrt{s_{NN}} = 2.76$ TeV.	119
5.1	The Signal count, mass position, width, signal-to-background ratio, significance for the $\Upsilon(1S)$ state obtained applying the fit procedure. Values are shown for the different rapidity ranges considered in the analysis.	142
5.2	The signal-to-background ratio, significance for the $\Upsilon(2S)$ state obtained applying the fit procedure. Values are shown for the two rapidity ranges considered in the analysis.	142

List of Tables

5.3	Summary of signal extraction of $\Upsilon(1S)$	144
5.4	Summary of signal extraction of $\Upsilon(2S)$. Values are given for the integrated rapidity bins, one for forward rapidity and other for the backward rapidity, that are possible to study.	144
5.5	The $A \times \epsilon$ of $\Upsilon(1S)$ for p-Pb and Pb-p period with statistical uncertainties.	148
5.6	Systematic uncertainties on $A \times \epsilon$ of $\Upsilon(1S)$ for p-Pb and Pb-p period. This one is related to the choice of the parametrisation used as input distribution for MC simulations.	148
5.7	Rapidity ranges used for the interpolation and for the measurement of the $\Upsilon(1S)$ nuclear modification factor. The central value of each range is also reported.	150
5.8	Interpolation uncertainties and results for the $\Upsilon(1S)$ cross section at $\sqrt{s} = 5.02$ TeV. The numbering of rapidity ranges is as defined in Tab. 5.7.	153
5.9	Summary of the relative systematic uncertainties on each quantity entering in the calculations of the results. Type U uncertainties are given as a range including the smallest and the largest values observed in the bins considered in this analysis.	153
5.10	$\Upsilon(1S)$ yields per unit of rapidity obtained in p-Pb collisions at $\sqrt{s_{NN}} = 5.02$ TeV for each bin considered in the analysis.	155
5.11	$\Upsilon(2S)$ yields per unit of rapidity obtained in p-Pb collisions at $\sqrt{s_{NN}} = 5.02$ TeV for each bin considered in the analysis.	155

5.12 Numerical values bin-by-bin measured in p-Pb collisions at $\sqrt{s_{\text{NN}}} =$
5.02 TeV. Statistical uncertainties are quoted as stat., uncorrelated
systematic uncertainties are quoted as uncorr. and fully correlated
uncertainties are quoted as glob. 158

List of Figures

1	Left (Right): ALICE and CMS nuclear modification factor of inclusive $\Upsilon(1S)$ production as a function of the average number of participant nucleons (rapidity). Bars stand for statistical uncertainties and filled (open) boxes uncorrelated (correlated) for uncertainties. On the right plot, open points are reflected with respect to the measured ones.	xx
2	(Left) Inclusive $\Upsilon(1S)$ nuclear modification factor evolution as a function of y_{cms} . (Right) Forward to backward ratio R_{FB} of inclusive $\Upsilon(1S)$ yields compared to the J/ψ R_{FB} . The vertical error bars represent the statistical uncertainties and the open boxes the uncorrelated systematic uncertainties.	xxi
1.1	The elementary particles in the Standard Model.	2
1.2	The summary of α_s as a function of momentum transfer Q	4
1.3	A schematic QCD phase diagram.	6
1.4	Time evolution of space-time diagram in heavy-ion collisions.	8

1.5	Top Left: R_{AA} of heavy-flavour decay electrons at central rapidity and heavy-flavour decay muons at forward rapidity in central (0–10%) Pb–Pb collisions, as a function of p_T . Top Right: Average R_{pPb} of prompt D^0 , D^+ and D^{*+} mesons as a function of p_T compared to the prompt D meson R_{AA} in the 20% most central Pb–Pb collisions and in the 40–80% centrality class. Bottom Left: centrality dependence of the R_{AA} of prompt D mesons and of J/ψ from B meson decay (measured by CMS) compared with a pQCD model including mass dependent radiative and collisional energy loss. Bottom Right: comparison of D^0 and charged pion R_{AA} as a function of centrality for $3 < p_T < 5$ GeV/c.	17
1.6	Schematic diagram of nuclear matter effects.	20
2.1	The schematic view of the four main experiments (ALICE, ATLAS, CMS and LHCb) in the LHC.	33
2.2	Schematic view of the ALICE experiment.	34
2.3	Layout of the Inner Tracking System (ITS).	35
2.4	Layout of the Time Projection Chamber (TPC).	36
2.5	Energy loss in the TPC as a function of momentum with superimposed Bethe-Bloch lines for various particle species.	37
2.6	Illustration of TRD surrounded by TPC and TOF.	38
2.7	The PHOS crystal and assembled module.	39
2.8	The layout of ALICE EMCal.	40
2.9	The schematic diagram of HMPID modules setup in ALICE.	41
2.10	The schematic diagram of FMD.	42
2.11	The schematic diagram of the V0 detector.	43
2.12	The view of T0 module of ALICE.	44

List of Figures

2.13	The setup of PMD detector in ALICE.	45
2.14	The setup of ZDC detector in ALICE.	46
2.15	The basic layout of the Forward Muon Spectrometer of ALICE. . . .	47
2.16	The Front Absorber of ALICE.	48
2.17	The picture of Muon Filter (left) and Dipole Magnet (right) of ALICE.	49
2.18	The picture of Tracking Station of ALICE.	50
2.19	The basic working principle of cathode pad chamber.	51
2.20	Layout of the ALICE Muon Trigger system. Different colours refer to the three strip widths.	53
2.21	A schematic diagram for the detector readout of ALICE.	55
2.22	General scheme of the AliRoot architecture.	60
3.1	The criteria used for filtering the runs for LHC11d period from the ALICE logbook.	74
3.2	Run-by-run analysis of trigger only tracks, tracker only tracks and matched tracks per Minimum Bias (CINT7B) events.	75
3.3	Run-by-run analysis of trigger tracks and tracker tracks per Mini- mum Bias (CINT7B) events.	76
3.4	Run-by-run analysis of trigger only tracks, tracker only tracks and matched tracks per Unlike Sign dimuon (CMUU7B) events.	76
3.5	Run-by-run analysis of trigger tracks and tracker tracks per Unlike Sign dimuon (CMUU7B) events.	77
3.6	Number of matched tracks per CMUU7B after applying the $p_T = 1$ and 2 GeV cut.	77
3.7	Charge asymmetry of the matched tracks for the CMUU7B trigger. .	78
3.8	Identified beam-gas tracks for CMUU7B events by using pDCA cut.	79

List of Figures

3.9	The average number of clusters per chamber per track for the Muon tracking system.	80
3.10	Efficiency of bending and non-bending planes of the Trigger chambers.	80
3.11	Multinomial probability for the Muon trigger system.	81
3.12	Run-by-run analysis of trigger only tracks, tracker only tracks and matched tracks per Minimum Bias (CPBI2_B1) events.	82
3.13	Centrality percentile of the central and peripheral Minimum Bias events.	83
3.14	Number of matched tracks per CPBI1MSH after applying the $p_T = 1$ and 2 GeV cut.	84
3.15	Charge asymmetry of the matched tracks for the CPBI1MSH trigger.	85
3.16	The average number of clusters per chamber per track in Pb–Pb for the Muon tracking system.	86
3.17	Efficiency of bending and non-bending planes in Pb–Pb of the Trigger chambers.	86
3.18	Multinomial probability for the Muon trigger system in Pb–Pb.	87
4.1	The F_{norm} as a function of run number. The dotted line represents the average value, while RMS gives the systematics.	95
4.2	Default fit procedure applied to the invariant mass distributions of opposite-sign dimuons in different centrality and rapidity bins. There are five plots top(integrated), middle left(0%–20%), middle right(20%–90%), bottom left($2.5 < y < 3.2$) and bottom right($3.2 < y < 4.0$).	101
4.3	Distribution of MB events as a function of centrality in Pb–Pb collisions.	103

4.4	The distribution of generated and the reconstructed $\Upsilon(1S)$ in MC simulation.	104
4.5	Energy dependence of the Υ cross-section at mid-rapidity, with overlaid power-law (left) and logarithmic (right) fit.	110
4.6	Energy dependence of the $\Upsilon(1S)$ cross-section at mid-rapidity, with overlaid FONLL predictions re-scaled by the α parameter. The points corresponding to different predictions at the same energy are slightly shifted horizontally, for visibility.	111
4.7	Experimental data points from CMS ($ y < 2$) [14] and LHCb ($2.0 < y < 4.5$) [16] and $\frac{d\sigma^\Upsilon}{dy}$ distribution obtained from Pythia6.4. . . .	114
4.8	Combined Pythia6.4 $BR \times \frac{d\sigma^\Upsilon}{dy}$ for pp collisions at $\sqrt{s} = 2.76$ TeV, plotted together with CMS data points at mid-rapidity [13]. The error bars represent the uncorrelated uncertainty (Extr.) while the boxes represent the correlated one (Norm.).	115
4.9	Nuclear modification factor of the inclusive $\Upsilon(1S)$ as a function of the average number of participant nucleons (left) and as a function of rapidity (right). Bars stand for statistical uncertainties and filled (open) boxes uncorrelated (correlated) for uncertainties.	120
4.10	Comparison of the ALICE nuclear modification factor of inclusive $\Upsilon(1S)$ and J/ψ [23] in the same kinematic range. Left (Right): results are shown as a function of the average number of participant nucleons (rapidity). Bars stand for statistical uncertainties and filled (open) boxes for uncorrelated (correlated) uncertainties.	121

- 4.11 Left (Right): ALICE and CMS [27] nuclear modification factor of inclusive $\Upsilon(1S)$ production as a function of the average number of participant nucleons (rapidity). Bars stand for statistical uncertainties and filled (open) boxes uncorrelated (correlated) for uncertainties. On the right plot, open points are reflected with respect to the measured ones. 122
- 4.12 Left (Right): ALICE R_{AA} of inclusive $\Upsilon(1S)$ as a function of the average number of participant nucleons (rapidity) compared with theoretical predictions from [28]. The CMS data point at mid-rapidity is included in the rapidity plot. Bars stand for statistical uncertainties and filled (open) boxes for uncorrelated (correlated) uncertainties. On the right plot, open points are reflected with respect to the measured ones. 124
- 4.13 ALICE nuclear modification factor of inclusive $\Upsilon(1S)$ as a function of the average number of participant nucleons (left) and rapidity (right) compared with theoretical predictions from [43, 44, 45]. The CMS data point at mid-rapidity is included in the rapidity plot. Bars stand for statistical uncertainties and filled (open) boxes for uncorrelated (correlated) uncertainties. On the right plot, open points are reflected with respect to the measured ones. 125

- 4.14 ALICE nuclear modification factor of inclusive $\Upsilon(1S)$ as a function of the average number of participant nucleons (left) and as a function of rapidity (right) compared with theoretical predictions from [47, 48]. The CMS data point at mid-rapidity is included in the rapidity plot. Bars stand for statistical uncertainties and filled (open) boxes for uncorrelated (correlated) uncertainties. On the right plot, open points are reflected with respect to the measured ones. 127
- 5.1 Fit procedure applied on the invariant mass distributions of opposite-sign dimuons in the different rapidity bins consider in this analysis at forward rapidity. The total fit function is represented by the red line. The green lines represent the three Extended Crystal Ball used to describe the Υ state distributions and the blue line represents the Double Exponential used to describe the underlying continuum. The numbers of $\Upsilon(nS)$ counts, the position, the width of the $\Upsilon(1S)$ and the χ^2/ndf are shown. 139
- 5.2 Fit procedure applied on the invariant mass distributions of opposite-sign dimuons in the different rapidity bins consider in this analysis at backward rapidity. The total fit function is represented by the red line. The green lines represent the three Extended Crystal Ball used to describe the Υ state distributions and the blue line represents the Double Exponential used to describe the underlying continuum. The numbers of $\Upsilon(nS)$ counts, the position, the width of the $\Upsilon(1S)$ and the χ^2/ndf are shown. 140
- 5.3 Run-by-run integrated signal distribution from Monte Carlo production fitted with an Extend Crystal Ball function for p-Pb period (left) and for Pb-p period (right) for the $2.5 < y_{\text{lab}} < 4$ rapidity range. . . 146

- 5.4 Run-by-run $A \times \varepsilon$ for the LHC13d and LHC13e periods (top) along with that of LHC13f (bottom) in the $2.5 < y < 4$ rapidity range. . . 147
- 5.5 $\Upsilon(1S)$ cross section in $2 < y < 3.5$ as a function of energy [5, 6, 7]. Fits according to three different shapes are also shown, as well as the interpolated values at $\sqrt{s} = 5.02$ TeV. 152
- 5.6 $\Upsilon(1S)$ cross section in $3 < y < 4.5$ as a function of energy [5, 6, 7]. Fits according to three different shapes are also shown, as well as the interpolated values at $\sqrt{s} = 5.02$ TeV. 152
- 5.7 Inclusive $\Upsilon(1S)$ nuclear modification factor evolution as a function of y_{cms} 157
- 5.8 Nuclear modification factor of inclusive $\Upsilon(1S)$ in p–Pb collisions at $\sqrt{s_{\text{NN}}} = 5.02$ TeV as a function of rapidity. The vertical error bars represent the statistical uncertainties and the open boxes the uncorrelated systematic uncertainties. The full boxes around $R_{\text{pPb}} = 1$ show the size of the correlated uncertainties. Also shown are several model calculations: (left) parton energy loss [13] with and without EPS09 shadowing at NLO and CEM with EPS09 shadowing at NLO [12]; (right) CGC based [18] and CSM with EPS09 shadowing at LO [15]. 160
- 5.9 (Left) Forward to backward ratio R_{FB} of inclusive $\Upsilon(1S)$ yields compared to the J/ψ R_{FB} [11]. The vertical error bars represent the statistical uncertainties and the open boxes the uncorrelated systematic uncertainties. (Right) Inclusive $\Upsilon(1S)$ R_{FB} compared to theoretical model calculations. The statistical and systematic uncertainties for the experimental value are added in quadrature. For the model calculations, uncertainties are quoted when available. . 160

List of Figures

1	The Crystal Ball function with variation of parameters.	172
2	The Gaussian, CB and CB2 function.	174

Contents

Synopsis	xvii
Publications List	xxv
List of Tables	xxvii
List of Figures	xxxii
1 The Quark-Gluon Plasma (QGP)	1
1.1 The Standard Model of Particle Physics	1
1.2 Confinement and Asymptotic Freedom	3
1.3 QCD Phase Diagram	5
1.4 QCD Matter in Heavy-Ion Collisions	7
1.5 Kinematic Variables	8
1.6 Observables of QCD Matter	10
1.6.1 Light Vector Meson Production	11
1.6.2 Photon Production	11
1.6.3 Event-By-Event Fluctuations	11
1.6.4 Strangeness Production	12
1.6.5 Jet Quenching	12
1.6.6 Elliptic Flow	13
1.6.7 Nuclear Modification Factor	13
1.6.8 Suppression of Heavy-Flavour	14

1.6.9	Quarkonium Suppression	15
1.7	Present Status of Quarkonium Suppression	18
2	ALICE Experiment at the LHC	31
2.1	The Large Hadron Collider (LHC)	31
2.2	A Large Ion Collider Experiment (ALICE)	33
2.3	Central Barrel Detectors	34
2.3.1	Inner Tracking System (ITS)	35
2.3.2	Time Projection Chamber (TPC)	36
2.3.3	Transition Radiation Detector (TRD)	37
2.3.4	Time of Flight (TOF)	38
2.3.5	Photon Spectrometer (PHOS)	39
2.3.6	Electromagnetic Calorimeter (EMCal)	40
2.3.7	High Momentum Particle Identification Detector (HMPID)	40
2.4	Forward Detectors	41
2.4.1	Forward Multiplicity Detector (FMD)	42
2.4.2	VZERO Detector (V0)	42
2.4.3	TZERO Detector (T0)	43
2.4.4	Photon Multiplicity Detector (PMD)	44
2.4.5	Zero Degree Calorimeter (ZDC)	44
2.5	The Forward Muon Spectrometer	46
2.5.1	Front Absorber	47
2.5.2	Muon Filter	48
2.5.3	Dipole Magnet	49
2.5.4	Beam Shield	50
2.5.5	Tracking Stations	50
2.5.6	Trigger Stations	52

Contents

2.6	Detector Readout	54
2.7	Online Control Systems	55
2.7.1	Detector Control System (DCS)	56
2.7.2	Central Trigger Processor (CTP)	56
2.7.3	Data Acquisition System (DAQ)	57
2.7.4	High Level Trigger (HLT)	57
2.7.5	Data Quality Monitoring (DQM)	58
2.7.6	Detector Algorithms (DA)	58
2.8	Offline Framework	59
2.8.1	AliRoot	59
2.8.2	The GRID	61
3	Data Quality Assurance (QA)	67
3.1	Muon Run Selection	68
3.2	Definition of Quality	71
3.3	Physics Event Selection	72
3.4	Muon QA for pp Collisions	73
3.4.1	Minimum Bias Events	74
3.4.2	Unlike Sign Dimuon Events	75
3.4.3	Charge Asymmetry and Beam-Gas Tracks	78
3.4.4	Tracking and Trigger Chambers Efficiencies	79
3.5	Muon QA for Pb–Pb Collisions	81
3.5.1	Minimum Bias Events	82
3.5.2	High p_T Events	83
3.5.3	Tracking and Trigger Chambers Efficiencies	85
3.6	Summary	87

4	Upsilon(Υ) Production in Pb-Pb Collisions	91
4.1	Data Selection	91
4.1.1	Trigger Selection	91
4.1.2	Track Selection	92
4.1.3	Centrality Selection	93
4.2	Minimum Bias Normalization	94
4.3	Signal Extraction	96
4.3.1	Fit Procedure	96
4.3.2	Fit Results	98
4.3.3	Systematic Uncertainties	98
4.3.4	Background Description	99
4.3.5	Mass Position and Signal Width	99
4.3.6	Signal Tail Parameters	99
4.4	$\Upsilon(1S)$ Yield in Pb-Pb Collisions	102
4.5	Monte Carlo Simulation	103
4.5.1	Acceptance and Efficiency Correction Factor	103
4.5.2	Embedding Production	105
4.5.3	Signal Line Shape	106
4.5.4	Systematic Uncertainties	106
4.5.5	Monte Carlo Parametrization	106
4.5.6	Muon Tracking Efficiency	107
4.5.7	Muon Trigger Efficiency	107
4.5.8	Matching Efficiency	108
4.6	Nuclear Modification Factor	108
4.7	Baseline: pp Reference Cross Section	108
4.7.1	Interpolation of $\Upsilon(1S)$ Cross Section at Mid-rapidity	109

4.7.2	Extrapolation of $\Upsilon(1S)$ Cross Section at Forward-rapidity . .	112
4.7.3	Interpolation of $\Upsilon(1S)$ Cross Section Using LHCb Measurement	116
4.8	Summary on Uncertainties	117
4.9	Results	119
4.10	Discussion	120
4.10.1	Comparison with J/ψ data from ALICE at forward rapidity .	120
4.10.2	Comparison with $\Upsilon(1S)$ data from the CMS Collaboration .	121
4.11	Comparison with theoretical predictions	122
4.11.1	Dynamical model	122
4.11.2	Transport models	124
4.12	Summary	127
5	Upsilon(Υ) Production in p-Pb Collisions	135
5.1	Data Selection	135
5.1.1	Event Selection	136
5.1.2	Track Selection	137
5.2	Signal Extraction	138
5.2.1	Fit Procedure	138
5.2.2	Fit Results	141
5.2.3	Systematic Uncertainties	142
5.3	Monte Carlo Simulation	145
5.3.1	Signal Line Shape	145
5.3.2	Acceptance Efficiency Correction Factor	146
5.3.3	Systematic Uncertainties	148
5.4	Baseline: Proton-Proton Reference Cross Section	149
5.5	Summary of Systematic Uncertainties	153
5.6	Results	154

Contents

5.6.1	Υ Yield in p-Pb Collisions	154
5.6.2	Cross Section Ratio of $\Upsilon(1S)$ and $\Upsilon(2S)$	155
5.6.3	Nuclear Modification Factor of $\Upsilon(1S)$	156
5.6.4	Forward-Backward Ratio $R_{FB}^{\Upsilon(1S)}$	158
5.7	Discussions	159
5.8	Summary	161
6	Summary and Outlook	165
6.1	Quality Assurance	165
6.2	Υ production in Pb-Pb	166
6.3	Υ production in p-Pb	167
6.4	Future ALICE Upgrade Program	168
6.5	Outlook	168
	Appendix	171
1.	Crystal Ball Function	171
2.	Extended Crystal Ball Function	173
3.	Double Exponential Function	174
4.	Double Power Law Function	175

Chapter 1

The Quark-Gluon Plasma (QGP)

In the Standard Model of particle physics the interaction between quarks and gluons are described by a theory called quantum chromodynamics (QCD). This model predicts that at very high temperature and/or energy density the hadronic matter can undergo a phase transition and can turn into a state of deconfined quarks and gluons known as Quark-Gluon Plasma (QGP) [1]. In this chapter the concept of QGP and its most important signatures will be discussed.

1.1 The Standard Model of Particle Physics

There are four fundamental interactions (Strong, Electromagnetic, Weak and Gravitation) that govern the world of elementary particles at everyday low energies. The Standard Model of Particle Physics deals with weak, electromagnetic and strong interactions and is very much successful in explaining a wide variety of experimental results as well as providing predictions of Higgs Boson. At present, there are six quarks (up, down, charm, strange, top, bottom), six leptons (electron, electron neutrino, muon, muon neutrino, tau, tau neutrino), the gauge

bosons (eight gluons, photons, W^+ , W^- and Z) and a massive scalar elementary particle Higgs boson in the Standard Model [Fig. 1.1].

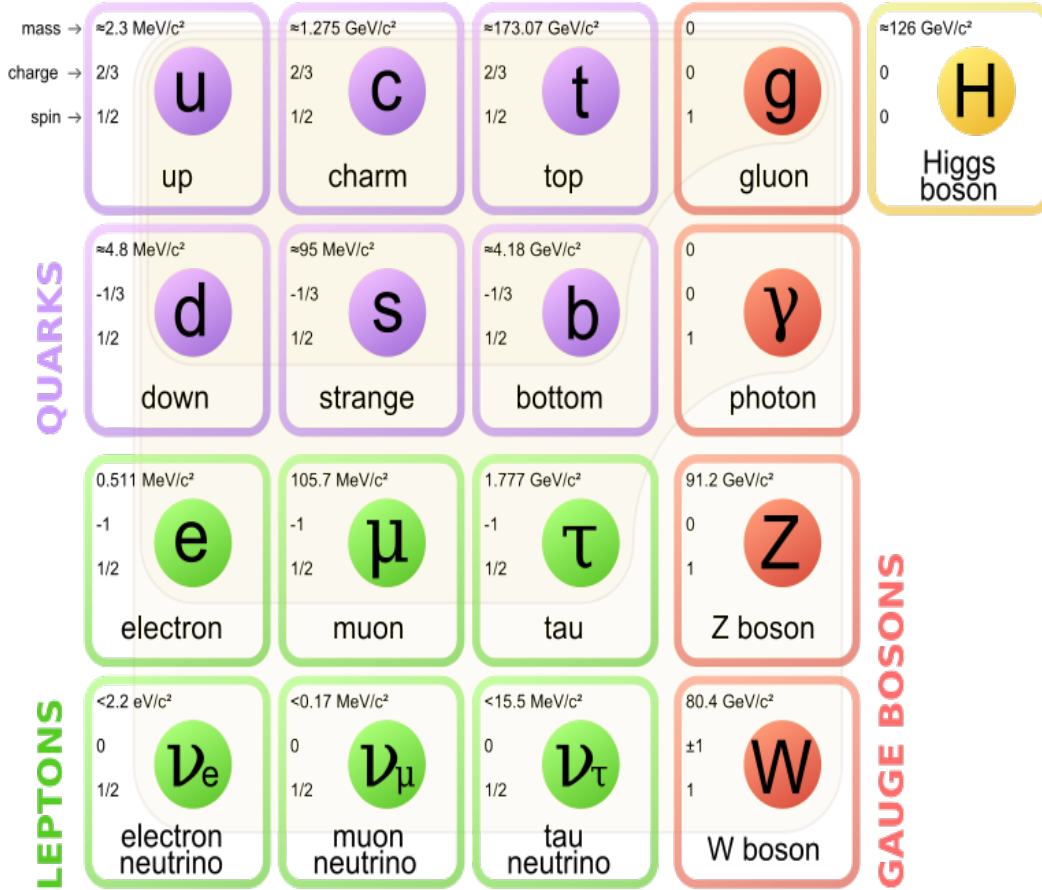


Figure 1.1: The elementary particles in the Standard Model.

Among these three interactions, strong interaction is the interaction between the elementary particles quarks and gluons by the exchange of color charge and is described by a theory called quantum chromodynamics (QCD). The quarks are spin-1/2 Fermions and comes in six flavours: up, down, strange, charm, bottom and top. According to QCD, each quark carries a color, called color charge. The color charge can be of three types – red, green and blue. Each quark has its own anti-quark and they (anti-quarks) carry anti-color (anti-red, anti-green, anti-blue).

On the other hand, gluons are spin-1 Bosons and can carry both the color and the anti-color. These quarks and gluons are the building blocks of all the hadrons (like protons, neutrons, pions etc.). A particular flavour of quark can have any one of the colors red, green or blue and can change its color via the exchange of the force carrying particle gluons. This exchange of color between two different colored quarks gives rise to attraction and repulsion, which is referred as strong interaction.

1.2 Confinement and Asymptotic Freedom

The phenomenon that quarks can not be isolated separately, is called confinement. Quarks always form a group and gives rise to hadrons. All hadrons are color neutral and can be of two types – mesons and baryons. Meson is composed of one quark and one anti-quark, so that overall it is color neutral. On the other hand baryons are generally composed of three quarks, each with different color charges, so that overall color charge is "white" or neutral (analogous to optics where the red, green and blue color form white). There is no analytical proof why confinement exists in QCD, i.e., quarks always forms a group. The present understanding is that as a quark-antiquark separate, a narrow tube (or string) of color field is formed between them. The string goes on increasing with the supplied energy and at a certain point it becomes more energetically favorable for a new quark-antiquark pair to spontaneously appear, than to allow the string to extend further.

The strength of the interaction between two quarks depends on the coupling constant α_s . For large momentum transfer Q (or sufficiently short distances), the interaction between the quarks becomes very weak. This phenomenon was dis-

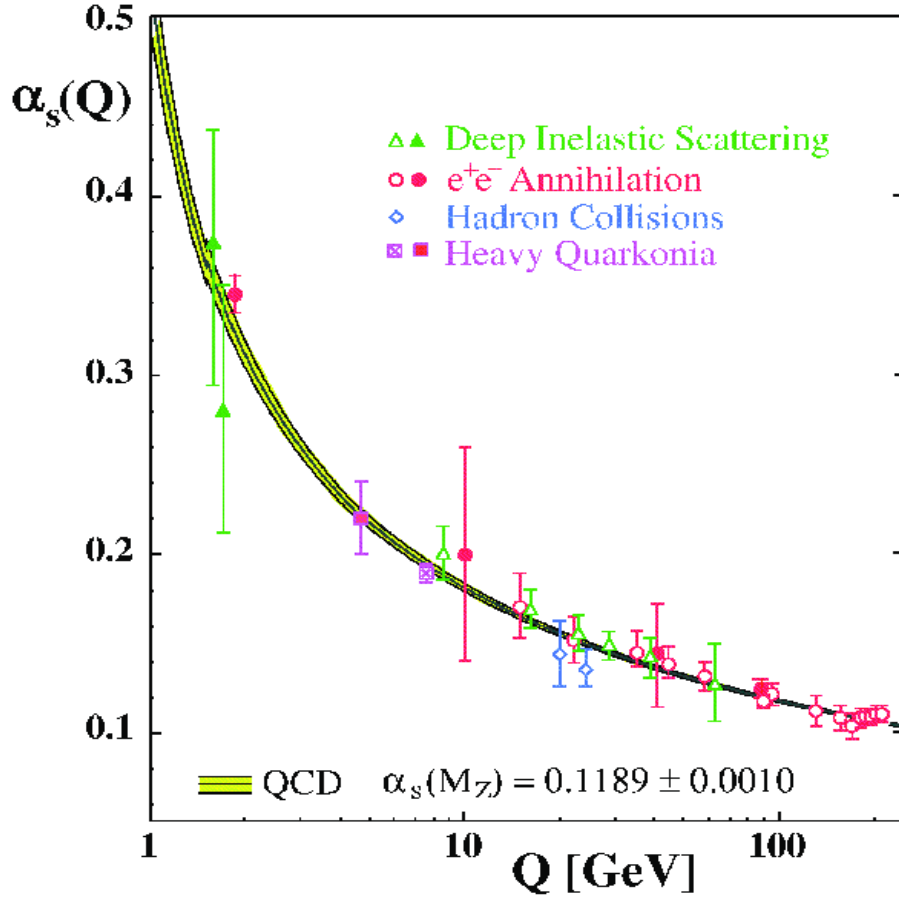


Figure 1.2: The summary of α_s as a function of momentum transfer Q .

covered by Frank Wilczek, David Gross, and independently by David Politzer in 1973 and is called asymptotic freedom. In the one loop approximation [2] the coupling constant α_s can be written as:

$$\alpha_s(Q) = \frac{12\pi}{(11n_c - 2n_f) \ln \left(\frac{Q^2}{\Lambda_{QCD}^2} \right)} \quad (1.1)$$

where n_c and n_f are the number of colors and number of quark flavours respectively. The energy scale Λ_{QCD} is called QCD scale and its value is ~ 200 MeV [3]. At high energy interactions the momentum transfer Q is high and the coupling

constant α_s is small [Fig. 1.2]. This is the asymptotic freedom regime, where the quarks and gluons interact weakly. In this regime $\alpha_s \ll 1$, the perturbative QCD (pQCD) approach can be applied to make predictions for observables expressed in terms of powers of α_s . When Q is less, α_s becomes larger and pQCD can not be used anymore. In this regime some effective phenomenological models or Lattice QCD (lQCD) [4] calculations are used.

1.3 QCD Phase Diagram

The thermodynamic properties of a system can be readily expressed in terms of phase diagram in the space of thermodynamic parameters. In the QCD Phase diagram [Fig. 1.3] the thermodynamic variables are baryonic chemical potential (μ) and temperature (T). At $\mu = T = 0$, the phase diagram represents the vacuum. If the temperature of a system is increased with small net baryon density, first a gas of hadrons (mostly pions) will be produced. If the temperature is increased further, then there will be a crossover at ~ 170 MeV [5, 6, 7] and the thermal fluctuations will break up the hadron gas into a soup of quark and gluons. This state is similar to that of the early universe after the big bang, where the net baryon density was close to zero. At low temperature with increasing chemical potential there will be ordinary atomic matter at ~ 300 MeV and nuclear matter at ~ 900 MeV. With further increase in chemical potential more dense nuclear matter will be formed, which is supposed to be the condition in the neutron stars. At even higher chemical potential and low temperature a state will emerge, where two quarks of same color will form pair, called Color Superconductor (analogous to Cooper pair). At the phase boundary there is a point, called critical point, where striking physical phenomena, analogous to critical opalescence, are expected (in critical

opalescence a normally transparent liquid appears cloudy at critical point, as the density fluctuations of the gas and liquid of a fluid mixture become comparable to the wavelength of light). However, the critical point is not discovered yet.

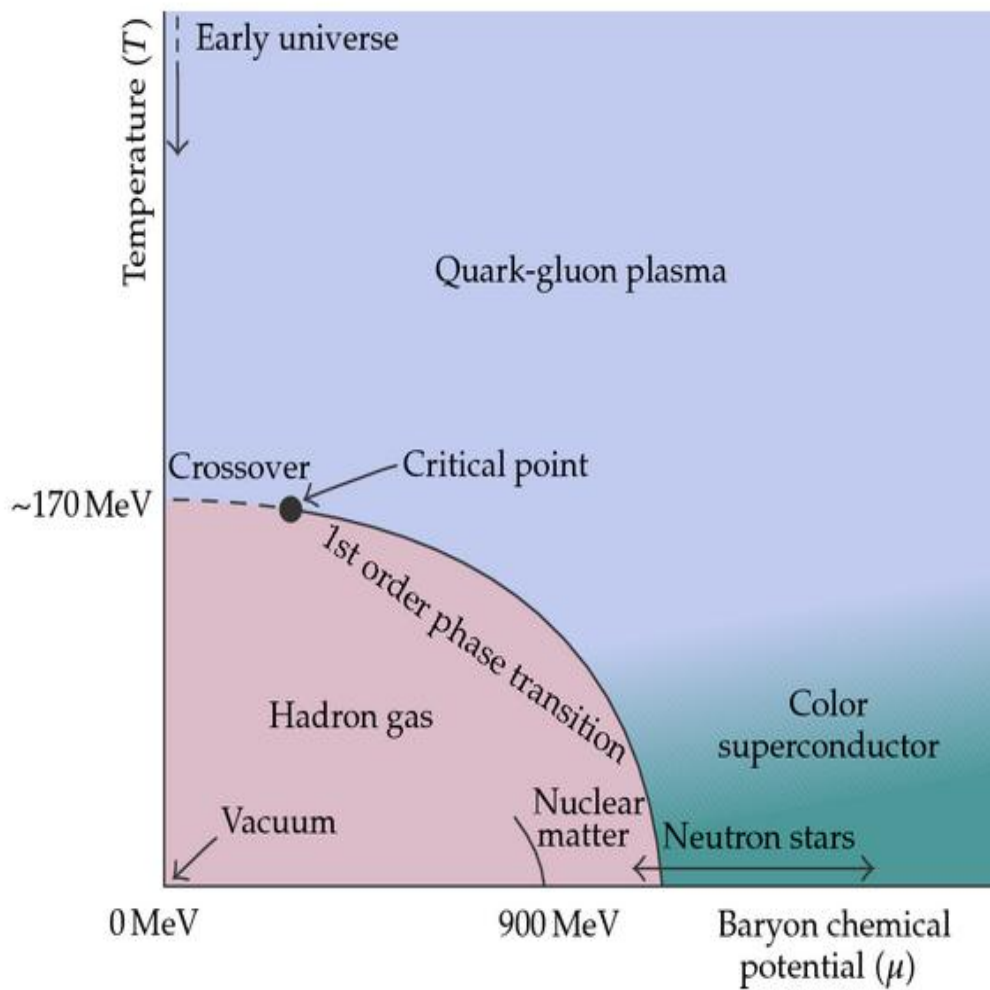


Figure 1.3: A schematic QCD phase diagram.

1.4 QCD Matter in Heavy-Ion Collisions

In the QCD phase diagram the region with low chemical potential (μ) and high temperature can be investigated in the particle accelerators by means of the heavy-ion collisions. According to the Bag Model [8], the energy density needed to create the QGP is $\sim 1 \text{ GeV}/fm^3$. With this goal in mind, relativistic heavy-ion collisions are conducted at Brookhaven National Laboratory (BNL) in USA and at CERN in Switzerland.

In the heavy-ion collisions two beams of heavy ions (like Au, Pb) are accelerated quite close to that of speed of light and then allowed to collide. In the center of mass frame of the colliding nuclei, these two nuclei can be seen as two thin disks due to Lorentz contraction. During collisions a nucleon in one nucleus may collide with many nucleons in the other nucleus and deposits large amount of energy in the collision region.

The energy density generated can be measured by measuring the charge particle produced per unit rapidity range:

$$\varepsilon = \frac{\langle m_T \rangle}{\tau_f A} \frac{dN}{dy} \quad (1.2)$$

where $\langle m_T \rangle = \sqrt{(E^2 - p_z^2)}$, is the average transverse mass of the charged particle, τ_f is the formation time of the charged particle, A is the overlapping area of the colliding nuclei and $\frac{dN}{dy}$ is the charge particle multiplicity in the rapidity range covered.

The collision takes place at $\tau = 0$ [Fig. 1.4]. At $\tau \sim 1 \text{ fm}/c$ ($\sim 10^{-24} \text{ sec}$), a hot dense fireball of quark-gluon matter of energy density $\varepsilon \sim \text{few } 10 \text{ GeV}/fm^3$ (approximately 30 times more than normal matter) [9] with a dimension of $\sim 300 \text{ fm}^3$ [10] is produced and the temperature reaches to $T \sim 550 \text{ MeV}$ (approximately

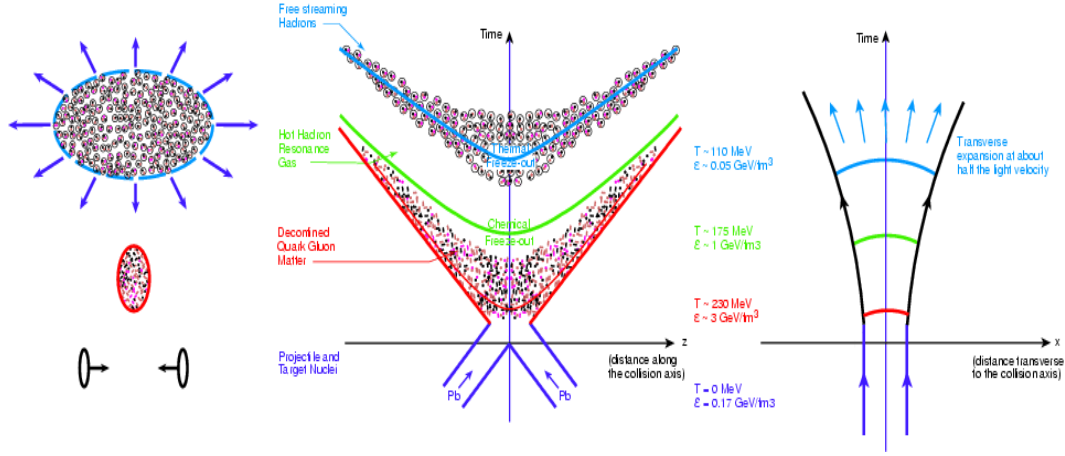


Figure 1.4: Time evolution of space-time diagram in heavy-ion collisions.

5.5×10^{12} K) at LHC. The fireball expands due to pressure gradient and after few fm/c (about 10^{-23} sec) "hadronization" starts. The life time of the plasma depends on the energy density reached in the collision, which is few fm/c in case of LHC. At "chemical freeze-out" the kinetic energy of the produced particles becomes too low for inelastic collisions and at this point all abundances and particle ratios becomes fixed. Finally, after the "thermal freeze-out" elastic collisions also stops and the kinematic distribution of the produced particles get fixed. On the right hand side diagram, the time evolution of the created "fireball" is shown in the plane transverse to the direction of collisions.

1.5 Kinematic Variables

In high energy collision experiments, it is convenient to use some kinematic variables which follow simple transformation rules. The transverse momentum (p_T), transverse mass (m_T), rapidity (y) and pseudo-rapidity (η) are some of those kinematic variables, which are used frequently in the literature and in this thesis. They follow simple Lorentz transformation properties. The simplification of trans-

formation rule of these kinematic variables are possible due to the presence of ultra-relativistic particles and a preferred axis in these high energy experiments.

For a particle of 4-momentum $p^\mu = p^\mu(E, p_x, p_y, p_z)$ the kinematic variables p_T , m_T , y and η are defined as:

$$p_T = \sqrt{(p_x^2 + p_y^2)} \quad (1.3)$$

$$m_T = \sqrt{(p_T^2 + m^2)} \quad (1.4)$$

$$y = \frac{1}{2} \ln \left(\frac{E + p_z}{E - p_z} \right) \quad (1.5)$$

$$\eta = -\ln \left[\tan \left(\frac{\theta}{2} \right) \right] = \frac{1}{2} \ln \left(\frac{|\vec{p}| + p_z}{|\vec{p}| - p_z} \right) \quad (1.6)$$

The rapidity y is not a Lorentz invariant quantity, but under Lorentz transformation it changes by a constant amount. For example, if A and B are two reference frames moving with velocity v with respect to each other, then the rapidities of a particle in these two reference frames can be related as:

$$y_B = y_A + y_\beta \quad (1.7)$$

where $\beta = v/c$ and y_β is given by:

$$y_\beta = \frac{1}{2} \ln \left(\frac{1 + \beta}{1 - \beta} \right) \quad (1.8)$$

In order to measure the rapidity y of a particle, one needs to measure both the energy and the longitudinal momentum of the particle. But in many experiment it

is only possible to measure the angle θ of the detected particle with respect to the beam axis. In that case it is convenient to calculate the pseudo-rapidity η of the particle rather than the rapidity y . However, the rapidity y and pseudo-rapidity η are connected by the formula:

$$y = \frac{1}{2} \ln \left[\frac{\sqrt{p_T^2 \cosh^2 \eta + m^2} + p_T \sinh \eta}{\sqrt{p_T^2 \cosh^2 \eta + m^2} - p_T \sinh \eta} \right]. \quad (1.9)$$

and vice-verse as,

$$\eta = \frac{1}{2} \ln \left[\frac{\sqrt{p_T^2 \cosh^2 y + m^2} + p_T \sinh y}{\sqrt{p_T^2 \cosh^2 y + m^2} - p_T \sinh y} \right]. \quad (1.10)$$

If the particle have a distribution $dN/dydp_T$ in terms of the rapidity variable y , then the distribution in terms of the pseudo-rapidity variable η can be written as:

$$\frac{dN}{d\eta dp_T} = \sqrt{1 - \frac{m^2}{m_T^2 \cosh^2 y}} \frac{dN}{dy dp_T}. \quad (1.11)$$

For a particle, if the momentum $|\vec{p}|$ is very large compared to its rest mass, then $|\vec{p}| \approx E$. In that case from Eqn. 1.5 and 1.6 it is evident that $y \approx \eta$.

1.6 Observables of QCD Matter

Since the fireball produced in the heavy-ion collisions is very short lived (\sim few 10^{-23} sec), it is not possible to directly measure the properties of the fireball. Rather some model dependent methods are used to characterize the nature of the collision. So, in order to understand the formation of QGP it is important to look into various observables predicted by the models. Here in this section a very short description of some of the main observables are discussed along with the

experimental constraints:

1.6.1 Light Vector Meson Production

The light vector mesons ρ , ω and ϕ have been suggested as a probes for the QGP, since their masses, widths and decay branching ratios may change in hot and dense matter. One of the ϕ meson decay channel is $\phi \rightarrow K^+ K^-$, and since the ϕ mass is only about 30 MeV above the mass of two Kaons, the branching ratios are expected to change dramatically in a QGP, due to chiral symmetry restoration [11]. But a comparison between the decays of $\phi \rightarrow K^+ K^-$ and $\phi \rightarrow e^+ e^-$ requires very high statistics, since the branching to the latter is only about 0.03 % and the signal is hard to distinguish from the combinatorial background.

1.6.2 Photon Production

The directly produced photons interacts electromagnetically and they have a mean free path much larger than the size of the matter produced in heavy ion collisions. The direct photons are generally divided into prompt photons and thermal photons. The prompt photons are produced in initial hard parton scatterings, while thermal photons are produced in the possible QGP phase and the hadron gas phase. An increase in the emission of thermal photons is expected from a QGP. But the low production rate and huge background from decays, e.g. $\pi^0 \rightarrow \gamma\gamma$ and $\eta \rightarrow \gamma\gamma$, make the isolation of the prompt and thermal components difficult.

1.6.3 Event-By-Event Fluctuations

The phase transitions are normally associated with large fluctuations. The QGP phase transition may yield non-statistical fluctuations in e.g. particle multiplicities,

ratios and transverse momenta. These fluctuations might be detectable in final state observables, some of which can be studied on an event-by-event basis. The requirement of high statistics per event for such analyses is met at RHIC and LHC energies, where a high multiplicity of particles is produced. The idea of event-by-event, net charge fluctuations as a QGP signature is not directly related to the phase transition. The main issue is the distribution of electric charge in a QGP (where the quarks carry $\pm\frac{1}{3}$ or $\pm\frac{2}{3}$ unit charges), compared to the distribution in ordinary hadronic matter. It has been argued that the distribution of more evenly spread charge in a QGP would survive the phase transition back to hadronic matter.

1.6.4 Strangeness Production

In the high energy density produced in heavy-ion collisions, the low mass quark pairs $u\bar{u}$, $d\bar{d}$ are produced copiously. Since the quarks are Fermions, the production of low mass quarks may be blocked due to Pauli exclusion principle. At that stage production of higher mass quarks $s\bar{s}$ are favoured. The abundance of strange quarks can however be explained by hadronic re-scattering processes. However, this complication can be solved by studying particles not likely to be produced by hadronic re-scattering, such as $\bar{\Lambda}$ (consisting of $\bar{u}\bar{d}\bar{s}$) and multistrange baryons.

1.6.5 Jet Quenching

In hard nucleus-nucleus collisions, two quarks or two gluons can be produced at the very early stage of the collisions back-to-back with high p_T . If it happens near the surface of the fireball, then one of them can hadronize and form a jet, while the other one passes through the large medium in the opposite direction,

loosing most of its energy by gluon radiation [12, 13]. The visible effect is the away-side jet quenching and a signature of the formation of dense matter. This signature can be found by studying the number of correlated jets at different angular separations.

1.6.6 Elliptic Flow

In non-central heavy-ion collisions the two participating nuclei have a almond shaped overlap region. The partonic pressure gradient leads to spatial and momentum anisotropy, which creates hydrodynamic collective motion of all the particles at the beginning of thermal equilibrium, called flow [14, 15]. Since the spatial anisotropy is largest at the beginning of the evolution, elliptic flow is especially sensitive to the early stages of system evolution. A measurement of elliptic flow thus provides access to the fundamental thermalization time scale of a relativistic heavy-ion collision.

1.6.7 Nuclear Modification Factor

The Nuclear Modification Factor (R_{AA}) is a measure for the difference in particle production in pp and nucleus-nucleus collisions, taking into account the different collision geometries and is defined as:

$$R_{AA} = \frac{Y(Pb-Pb)}{\langle N_{coll} \rangle \times Y(pp)} \quad (1.12)$$

where $Y(PbPb)$ and $Y(pp)$ are the yield (or number of particles per event) in Pb-Pb and pp collisions, respectively, and N_{coll} is the average number of binary nucleon-nucleon collisions, which have taken place in the collision of two lead ions. Since each lead nucleus consists of 208 nucleons, i.e. protons and neutrons,

it is clear that a typical Pb–Pb collisions can be seen as a superposition of many pp collisions. The N_{coll} , which can be determined in the experiment, measures how many pp collisions should be equivalent on average to one Pb–Pb collision.

If the nuclear modification factor is equal to one, the production of particles in one Pb–Pb collision on average is the same as in N_{coll} independent pp collisions. Naively, this could be interpreted such that the physics of pp and Pb–Pb collisions is the same.

1.6.8 Suppression of Heavy-Flavour

Charm and beauty quarks are effective probes of the properties of the hot and dense stronglyinteracting medium formed in high-energy nuclear collision, the Quark-Gluon Plasma (QGP). They are sensitive to the transport properties of the medium, since they are predominantly produced on a short time scale in primary partonic scattering processes. Thus the measurement of nuclear modification factor in heavy-ion collisions provides insights into the mechanisms of parton energy loss in the hot and dense medium.

By measuring the heavy-flavour nuclear modification factor we get some insight of the hot dense medium produced at the LHC [Fig. 1.5]. The results obtained with ALICE indicate a strong suppression of heavy flavour production in central Pb–Pb collisions for $p_T > 3$ GeV/c, observed for heavy-flavour decay electrons and muons, for electrons from beauty decays and for D mesons. From the comparison with p–Pb measurements, it is possible to conclude that the suppression observed in Pb–Pb collisions is mainly due to final state effects, i.e. the interaction of heavy quarks with the hot medium. The comparison of prompt D meson and non-prompt J/ψ R_{AA} shows an indication of larger suppression for D mesons with respect to B mesons, that can confirm the mass dependent nature of

the energy loss mechanisms.

1.6.9 Quarkonium Suppression

In heavy-ion collisions, heavy flavors, specially charm and bottom, are produced at the very early stage by the hard scattering and hence can be used to characterize the hot and dense medium. It is predicted that the production of quarkonia (charmonia and bottomonia) in nucleus-nucleus collisions will be suppressed relative to that in proton-proton due to the Color-Debye Screening mechanism [16]. When the screening radius becomes less than the binding radius of the quark system, the confining force can no longer holds the quark together and the deconfinement occurs. This effect reduces the number of quarkonia states and leads to suppression.

The suppression of quarkonia can be quantified by measuring the Nuclear Modification Factor R_{AA} (R_{pPb}), which is obtained by dividing the yield in Pb–Pb (p-Pb) collisions per unit of rapidity by $\langle T_{AA(pPb)} \rangle$, the average nuclear overlap function and by $\frac{d\sigma^{pp}}{dy}$, the pp reference y-differential cross-section.

$$R_{AA(pPb)} = \frac{\frac{dY_{Y(1S)}}{dy}}{\langle T_{AA(pPb)} \rangle \times \frac{d\sigma^{pp}}{dy}} \quad (1.13)$$

In particular, a sequential suppression of quarkonia, depending on their binding energy has been proposed as a thermometer of the deconfined medium [17]. Since different resonances have different dimensions and binding energies, it is expected that the less tightly bound states melt at lower temperatures: this effect is known as sequential suppression. While the excited states are dissociated just above the critical temperature T_c needed to form the QGP, the fundamental states melt far above that value, as shown in Table 1.1. It is important to note that the un-

certainties are large and old calculations predict lower values than those reported here. The dissociation of specific resonances can thus be used as a thermometer of the QGP.

State	$J/\psi(1S)$	$\chi_c(1P)$	$\psi(2S)$	$\Upsilon(1S)$	$\chi_b(1P)$	$\Upsilon(2S)$	$\chi_b(2P)$	$\Upsilon(3S)$
Mass (GeV)	3.10	3.53	3.68	9.46	9.99	10.02	10.26	10.36
ΔE (GeV)	0.64	0.20	0.05	1.10	0.67	0.54	0.31	0.20
r_0 (fm)	0.50	0.72	0.90	0.28	0.44	0.56	0.68	0.78
T_d/T_c	2.10	1.16	1.12	> 4	1.76	1.60	1.19	1.17

Table 1.1: Quarkonium binding energies (ΔE), quark distance (r_0) and dissociation temperatures in units of T_c [18].

As the collision energy increases, more and more heavy quarks are produced, leading to quarkonium generation. However, this contribution is expected to be important for the charmonium yield and negligible or very small for the Υ yield, even at the LHC energies.

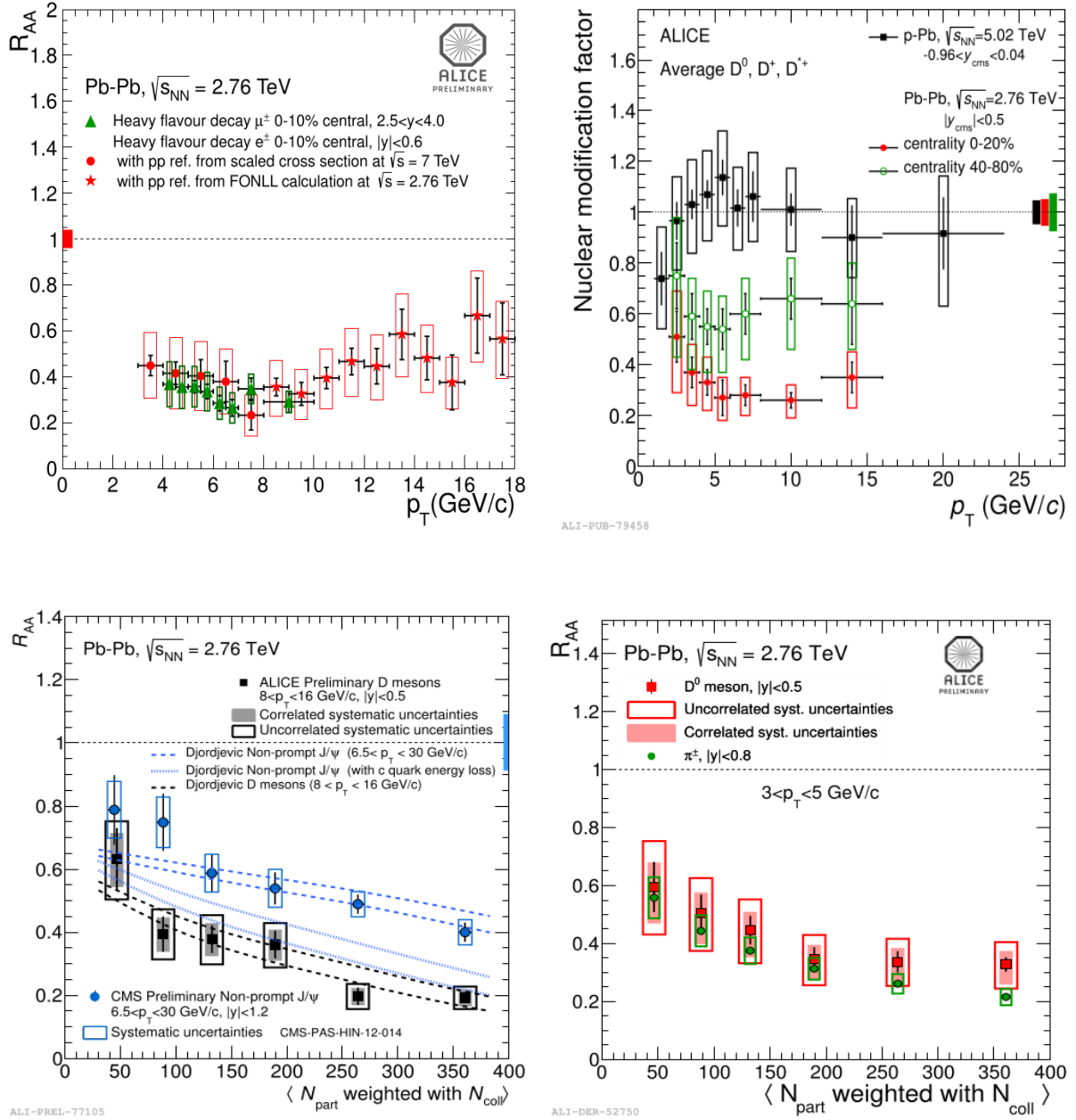


Figure 1.5: Top Left: R_{AA} of heavy-flavour decay electrons at central rapidity and heavy-flavour decay muons at forward rapidity in central (0–10%) Pb–Pb collisions, as a function of p_T . Top Right: Average R_{pPb} of prompt D^0 , D^+ and D^{*+} mesons as a function of p_T compared to the prompt D meson R_{AA} in the 20% most central Pb–Pb collisions and in the 40–80% centrality class. Bottom Left: centrality dependence of the R_{AA} of prompt D mesons and of J/ψ from B meson decay (measured by CMS) compared with a pQCD model including mass dependent radiative and collisional energy loss. Bottom Right: comparison of D^0 and charged pion R_{AA} as a function of centrality for $3 < p_T < 5$ GeV/c.

1.7 Present Status of Quarkonium Suppression

The quarkonium states are suppressed in the QGP with different dissociation probabilities for the various mass states, depending on their binding energy. In the charmonium sector (bound state of c and \bar{c} quarks), a significant suppression has been observed for the J/ψ state at SPS [19, 20, 21] ($\sqrt{s_{NN}} = 17.3$ GeV), RHIC [22, 23] ($\sqrt{s_{NN}} = 39, 62.4, 200$ GeV) and LHC [24, 25, 26] ($\sqrt{s_{NN}} = 2.76$ TeV) energies. The $\psi(2S)$ charmonium state has lower binding energy than the J/ψ one and cannot be produced by the decays of higher mass states. It is observed at SPS energies [27], the suppression of $\psi(2S)$ yield is about 2.5 times larger than for the J/ψ state. A qualitative description of these results can be understood by assuming a regeneration process in addition to the dissociation by colour screening for high-energy collisions, known as hot nuclear matter effects. The color screening depends on the color density in the QGP medium, whereas the recombination effect is proportional to the square of the number of $c\bar{c}$ pair in the medium ($N_{c\bar{c}}^2$). The regeneration mechanism is particularly important at LHC energies, where the multiplicity of charm quarks is large [28, 29, 30, 31, 32]. With the high collision energies and luminosities recently available at RHIC and LHC, it is also possible to study bottomonium production in heavy-ion collisions [33, 34, 35, 36, 37]. Compared with the J/ψ case, the probability for the Υ states to be regenerated in the medium is much smaller due to the lower production cross section of $b\bar{b}$ pairs [38].

At RHIC, the inclusive $\Upsilon(1S + 2S + 3S)$ production has been measured in Au–Au collisions at mid-rapidity by STAR [33] and PHENIX [34] Collaborations. The observed suppression is consistent with the melting of the $\Upsilon(2S)$ and $\Upsilon(3S)$ states. At LHC, the CMS Collaboration has measured the mid-rapidity production of bottomonium states in Pb–Pb collisions. The $\Upsilon(1S)$ yield is suppressed by approxi-

mately a factor of two. Moreover, the $\Upsilon(2S)$ and the $\Upsilon(3S)$ are almost completely suppressed [35, 36].

However, the feed-down from higher mass bottomonia (between 40% and 50% for $\Upsilon(1S)$ [39]) complicates the data interpretation. Furthermore, the suppression due to the QGP must be disentangled from that due to Cold Nuclear Matter (CNM) effects, which, as of now, are not accurately known neither at RHIC energies [33] nor in the forward rapidity regions probed at LHC. Cold nuclear matter effects can be studied in proton–nucleus (p–A) collisions, where the QGP is not expected to be formed. It can be separated into initial and final-state effects.

The initial-state effects occur prior to the formation of the heavy-quark pair. This includes shadowing, anti-shadowing, EMC, gluon saturation [40, 41, 42, 43] and parton energy loss effects [44, 45, 46]. The nuclear Parton Distribution Functions (nPDF) differ from those in free nucleons (PDF). Since the gluon fusion mechanism dominates the production of heavy-quark pairs in high energy collisions, quarkonium production is particularly sensitive to the gluon nPDF, which is presently not well known. Bjorken- x (x_{Bj}) is defined as the fraction of the hadron momentum carried by the parton. The gluon nPDF includes a shadowing region at low x_{Bj} ($x_{Bj} \lesssim 0.01$) corresponding to a suppression of gluons, an anti-shadowing region at intermediate x_{Bj} ($0.01 \lesssim x_{Bj} \lesssim 0.3$) corresponding to an enhancement of gluons, and an additional suppression of gluons known as EMC effect at higher x_{Bj} ($0.35 \lesssim x_{Bj} \lesssim 0.7$). When the energy density is high enough (like LHC energies), at low x_{Bj} gluons start to recombine with each other leading to gluon saturation. Then the Colour Glass Condensate (CGC) model can be used to describe the nucleus [47]. Finally, partons can lose energy before creating the heavy-quark pair, therefore modifying the kinematic distributions of quarkonia.

The final-state effects are those, in which case the heavy-quark pair interacts

with the nuclear matter and eventually break up after the hadronization [48]. After a quarkonium state is formed it can break-up as it passes through the colliding nucleus. This effect is also called nuclear absorption. The break-up cross section depends on the nature of the pre-resonant state and is expected to be small for $\Upsilon(1S)$ at high energy [48, 49, 50]. The final-state resonance can also interact with surrounding dense gas system of hadronic comovers and lose energy or even break up. This process is known as comovers absorption [51, 52, 53].

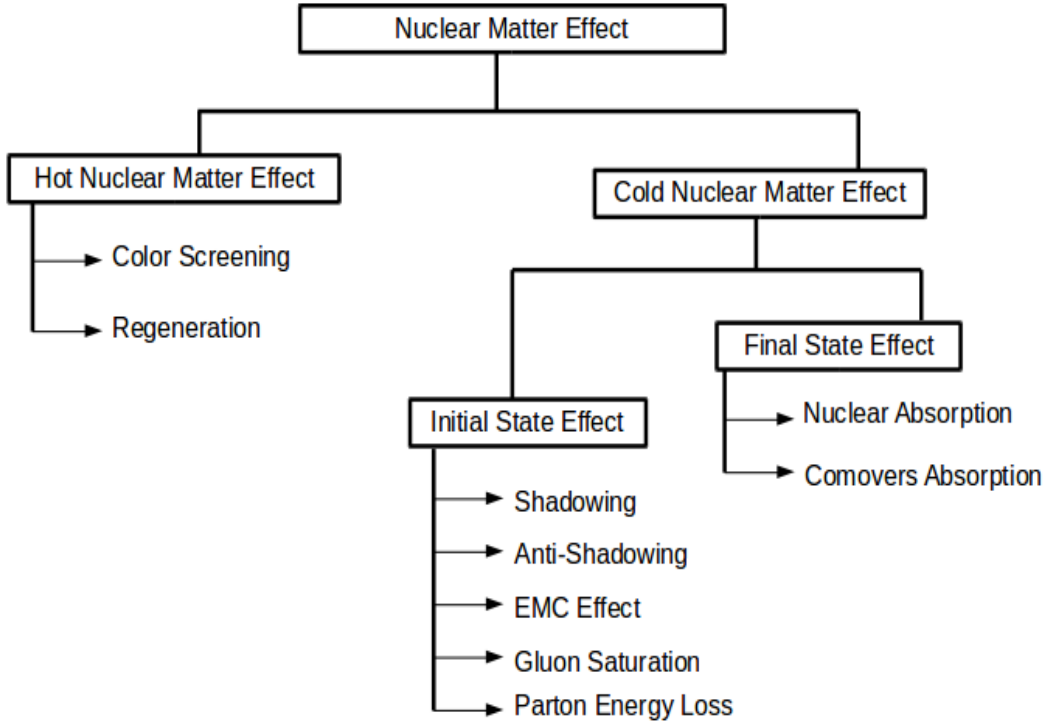


Figure 1.6: Schematic diagram of nuclear matter effects.

In this thesis, both the effect of hot and cold nuclear matter effect on the Υ production will be discussed. In chapter 2 the detector used for the data analysis will be described. The data taken for the analysis needs quality assurance, which will be discussed in chapter 3. The effect of hot nuclear matter will be discussed in the light of the experimental results of Υ production in Pb–Pb collision in chap-

ter 4. In chapter 5, the measurements on Υ production in p-Pb collision will be discussed, which is the first investigation of CNM effects on Υ at forward rapidity. Finally in chapter 6, the summary of the experimental results and future outlook will be presented.

Bibliography

- [1] E.V. Shuryak, Theory of Hadronic Plasma, Sov. Phys. JETP **47** 212 (1978).
- [2] M. E. Peskin et al. An Introduction to Quantum Field Theory. Addison-Wesley Publishing Company, 1995.
- [3] J. Beringer et al. Review of Particle Physics. Phys. Rev. D, **86**, Jul 2012.
- [4] T. Hatsuda et al. QCD phenomenology based on a chiral effective Lagrangian. Phys. Rep., 247(5-6):221-367, Oct 1994.
- [5] Z. Fodor et al. Critical point of QCD at finite T and μ , lattice results for physical quark masses. JHEP, 2004(04), 2004.
- [6] P. Petreczky. QCD at non-zero temperature: Bulk properties and heavy quarks. Mod. Phys. Lett. A, 25(37):3081-3092, 2010.
- [7] Y. Aoki et al. The QCD transition temperature: Results with physical masses in the continuum limit II. JHEP, 0906(088), 2009.
- [8] A. Chodos et al. New extended model of hadrons. Phys. Rev. D, (9):3471-3495, June 1974.

Bibliography

- [9] H. Satz. Colour deconfinement and quarkonium binding. J. Phys. G, 32(R25), 2006.
- [10] K. Aamodt et al. Two-pion Bose-Einstein correlations in central Pb-Pb collisions at $\sqrt{s_{NN}} = 2.76$ TeV. Phys. Lett. B, 696(4):328-337, 2011.
- [11] R. Arnaldi et al. First Measurement of the ρ Spectral Function in High-Energy Nuclear Collisions. Phys. Rev. Lett., **96**, Apr 2006.
- [12] M. Gyulassy et al. Jet quenching and monojet rates in ultrarelativistic nucleus-nucleus collisions. Nucl. Phys. A, 590(1-2):511-514, Jul 1995.
- [13] The PHENIX Collaboration. Dense-Medium Modifications to Jet-Induced Hadron Pair Distributions in Au+Au Collisions at $\sqrt{s_{NN}} = 200$ GeV. Phys. Rev. Lett., **97**, Aug 2006.
- [14] S. Voloshin et al. Flow Study in Relativistic Nuclear Collisions by Fourier Expansion of Azimuthal Particle Distributions. arXiv:hep-ph/9407282, Jul 1994.
- [15] The STAR Collaboration. System size and energy dependence of nearside dihadron correlations. Phys. Rev. C, **85**, Jan 2012.
- [16] T. Matsui and H. Satz, Phys. Lett. B **178**, 416 (1986).
- [17] S. Digal, P. Petreczky, and H. Satz, Phys. Rev. D **64** (2001) 094015 [arXiv:hep-ph/0106017].

- [18] H. Satz, Colour deconfinement and quarkonium binding, J. Phys. G **32** (2006) R25 [arXiv:hep-ph/0512217].
- [19] M. Abreu, et al., J/ψ , ψ' and Drell–Yan production in S–U interactions at 200 GeV per nucleon, Phys. Lett. B **449** (1999) 128–136.
- [20] B. Alessandro, et al., A new measurement of J/ψ suppression in Pb–Pb collisions at 158 GeV per nucleon, Eur. Phys. J. C **39** (2005) 335–345, arXiv:hep-ex/0412036.
- [21] R. Arnaldi, et al., J/ψ production in indium–indium collisions at 158 GeV/nucleon, Phys. Rev. Lett. **99** (2007) 132302.
- [22] A. Adare, et al., J/ψ production vs centrality, transverse momentum, and rapidity in Au + Au collisions at $\sqrt{s_{\text{NN}}} = 200$ GeV, Phys. Rev. Lett. **98** (2007) 232301, arXiv:nucl-ex/0611020.
- [23] B. Abelev, et al., J/ψ production at high transverse momentum in p + p and Cu + Cu collisions at $\sqrt{s_{\text{NN}}} = 200$ GeV, Phys. Rev. C **80** (2009) 041902, arXiv:0904.0439.
- [24] B. Abelev, et al., J/ψ suppression at forward rapidity in Pb–Pb collisions at $\sqrt{s_{\text{NN}}} = 2.76$ TeV, Phys. Rev. Lett. **109** (2012) 072301, arXiv:1202.1383.
- [25] G. Aad, et al., Measurement of the centrality dependence of J/ψ yields and observation of Z production in lead–lead collisions with the ATLAS detector at the LHC, Phys. Lett. B **697** (2011) 294–312, arXiv:1012.5419.

- [26] S. Chatrchyan, et al., Suppression of non-prompt J/ψ , prompt J/ψ , and $\Upsilon(1S)$ in PbPb collisions at $\sqrt{s_{NN}} = 2.76$ TeV, J. High Energy Phys. 1205 (2012) 063, arXiv:1201.5069.
- [27] B. Alessandro, et al., ψ' production in Pb–Pb collisions at 158 GeV/nucleon, Eur. Phys. J. C 49 (2007) 559–567, arXiv:nucl-ex/0612013.
- [28] L. Grandchamp, R. Rapp, G.E. Brown, In medium effects on charmonium production in heavy ion collisions, Phys. Rev. Lett. 92 (2004) 212301, arXiv:hep-ph/0306077.
- [29] E. Bratkovskaya, A. Kostyuk, W. Cassing, H. Stoecker, Charmonium chemistry in $A + A$ collisions at relativistic energies, Phys. Rev. C 69 (2004) 054903, arXiv:nucl-th/0402042.
- [30] R.L. Thews, M. Schroedter, J. Rafelski, Enhanced J/ψ production in deconfined quark matter, Phys. Rev. C 63 (2001) 054905, arXiv:hep-ph/0007323.
- [31] P. Braun-Munzinger, J. Stachel, (Non)thermal aspects of charmonium production and a new look at J/ψ suppression, Phys. Lett. B 490 (2000) 196–202, arXiv:nucl-th/0007059.
- [32] A. Andronic, P. Braun-Munzinger, K. Redlich, J. Stachel, Statistical hadronization of charm in heavy ion collisions at SPS, RHIC and LHC, Phys. Lett. B 571 (2003) 36–44, arXiv:nucl-th/0303036.
- [33] L. Adamczyk, et al., Suppression of Υ production in d + Au and Au + Au collisions at $\sqrt{s_{NN}} = 200$ GeV, Phys. Lett. B 735 (2014) 127, arXiv:1312.3675.

- [34] A. Adare, et al., Measurement of $\Upsilon(1S + 2S + 3S)$ production in p + p and Au + Au collisions at $\sqrt{s_{NN}} = 200$ GeV, arXiv:1404.2246.
- [35] S. Chatrchyan, et al., Indications of suppression of excited Υ states in PbPb collisions at $\sqrt{s_{NN}} = 2.76$ TeV, Phys. Rev. Lett. 107 (2011) 052302, arXiv:1105.4894.
- [36] S. Chatrchyan, et al., Observation of sequential Υ suppression in PbPb collisions, Phys. Rev. Lett. 109 (2012) 222301, arXiv:1208.2826.
- [37] B. Abelev, et al., Production of $\Upsilon(1S)$ in PbPb collisions at $\sqrt{s_{NN}} = 2.76$ TeV, ALICE-PUBLIC-2014-001.
- [38] L. Grandchamp, S. Lumpkins, D. Sun, H. van Hees, R. Rapp, Bottomonium production at RHIC and CERN LHC, Phys. Rev. C 73 (2006) 064906, arXiv:hep-ph/0507314
- [39] B. Abelev, et al., Measurement of quarkonium production at forward rapidity in pp collisions at $\sqrt{s} = 7$ TeV, Eur. Phys. J. C 74 (2014) 2974, arXiv:1403.3648
- [40] K. Eskola, H. Paukkunen, C. Salgado, EPS09: a new generation of NLO and LO nuclear parton distribution functions, J. High Energy Phys. 0904 (2009) 065, arXiv:0902.4154.
- [41] D. de Florian, R. Sassot, Nuclear parton distributions at next-to-leading order, Phys. Rev. D 69 (2004) 074028, arXiv:hep-ph/0311227.

- [42] D. de Florian, R. Sassot, P. Zurita, M. Stratmann, Global analysis of nuclear parton distributions, Phys. Rev. D 85 (2012) 074028, arXiv:1112.6324.
- [43] M. Hirai, S. Kumano, T.-H. Nagai, Determination of nuclear parton distribution functions and their uncertainties in next-to-leading order, Phys. Rev. C 76 (2007) 065207, arXiv:0709.3038.
- [44] S. Gavin, J. Milana, Energy loss at large $x(F)$ in nuclear collisions, Phys. Rev. Lett. 68 (1992) 1834–1837.
- [45] S.J. Brodsky, P. Hoyer, A bound on the energy loss of partons in nuclei, Phys. Lett. B 298 (1993) 165–170, arXiv:hep-ph/9210262.
- [46] F. Arleo, S. Peigne, Heavy-quarkonium suppression in p–A collisions from parton energy loss in cold QCD matter, J. High Energy Phys. 1303 (2013) 122, arXiv:1212.0434.
- [47] H. Fujii, K. Watanabe, Heavy quark pair production in high energy pA collisions: quarkonium, Nucl. Phys. A 915 (2013) 1–23, arXiv:1304.2221.
- [48] R. Vogt, Cold nuclear matter effects on J/ψ and Υ production at the LHC, Phys. Rev. C 81 (2010) 044903, arXiv:1003.3497.
- [49] E. Ferreira, F. Fleuret, J. Lansberg, N. Matagne, A. Rakotozafindrabe, Υ production in p(d)A collisions at RHIC and the LHC, Eur. Phys. J. C 73 (2011) 2427, arXiv:1110.5047.
- [50] C. Lourenco, R. Vogt, H.K. Woehri, Energy dependence of J/ψ absorption in proton–nucleus collisions, J. High Energy Phys. 0902 (2009) 014,

arXiv:0901.3054.

- [51] S. Gavin, R. Vogt, Charmonium suppression by comover scattering in Pb + Pb collisions, Phys. Rev. Lett. 78 (1997) 1006–1009, arXiv:hep-ph/9606460.
- [52] A. Capella, A. Kaidalov, A. Kouider Akil, C. Gerschel, J/ψ and ψ' suppression in heavy ion collisions, Phys. Lett. B 393 (1997) 431–436, arXiv:hep-ph/9607265.
- [53] E. Ferreira, $\psi(2S)$ versus J/ψ suppression in the comover interaction approach, arXiv:1411.0549.

Chapter 2

ALICE Experiment at the LHC

There are four main physics experiments ALICE, ATLAS, CMS and LHCb, which are collecting data from the LHC. The results presented in this thesis are from the analysis of the data obtained from the Muon Spectrometer of ALICE. In this chapter, the LHC accelerator, ALICE experiments and its data taking framework will be discussed, with more emphasis on the detectors related to the analysis presented in this thesis.

2.1 The Large Hadron Collider (LHC)

The Large Hadron Collider (LHC) is an experimental facility build by the European Organization of Nuclear Research (CERN) from 1998 to 2008 and become successfully operational on 23rd November, 2009. It is the most powerful particle accelerator till date, which lies in a tunnel of circumference 27 Km and at a depth between 50 to 175 m beneath the ground in Franco-Swiss border near Geneva, Switzerland.

There are two parallel beam pipes inside the collider tunnel, where two beams

are circulated in opposite directions at very high energy and then allowed to collide in the four interaction points located in ALICE, ATLAS, CMS and LHCb sites. To keep the beam focused in the beam pipes for collisions around 1,232 dipole magnets, 392 quadrupole magnets and 1,600 superconducting magnets are used. The super-fluid helium are used to maintain the operating temperature of the magnets at 1.9 K. Since the magnets are operational at a certain current threshold, a minimal particle energy is needed for the LHC collider in the injection level. For this purpose Super Proton Synchrotron (SPS) is used. The SPS provides proton beam of energy 450 GeV, which is then injected in the main LHC ring. In LHC the proton beam is then accelerated to reach the desired energy. When the desired beam energy is reached, the two opposite directional beams are collided in four interaction points, where the main experimental sites (ALICE, ATLAS, CMS and LHCb) are located as shown in the Fig. 2.1. The beam intensity goes down after several interactions and the interaction rates starts to decrease. This period is about 3 – 4 hours. At that point a new fill is prepared and injected into the collider.

The LHC has delivered pp collisions at energies $\sqrt{s} = 0.9, 2.76, 7$ and 8 TeV. However it also delivered two Pb-Pb collisions (around four weeks in 2010 and 2011) at energy $\sqrt{s} = 2.76$ TeV for the Heavy-Ion collision experiments to investigate the hot nuclear matter effect. However there is also some cold nuclear matter effects present in the Heavy-Ion collisions. In order to study these cold nuclear matter effects p-Pb collisions at $\sqrt{s} = 5.02$ TeV are provided by the LHC at the beginning of 2013.

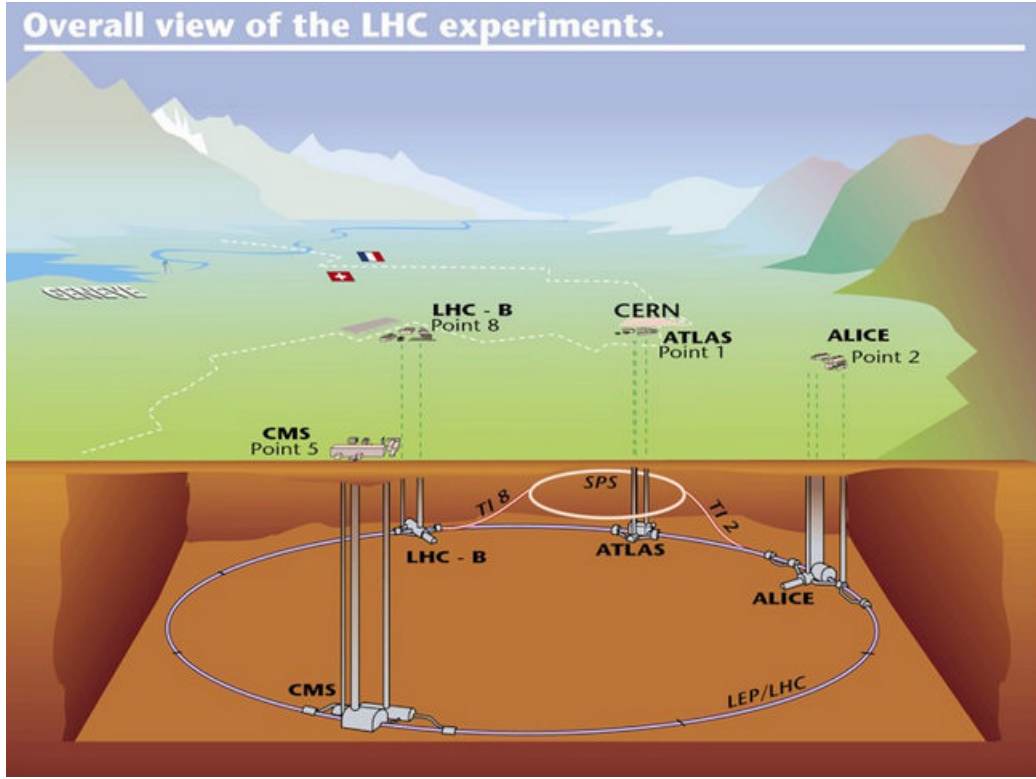


Figure 2.1: The schematic view of the four main experiments (ALICE, ATLAS, CMS and LHCb) in the LHC.

2.2 A Large Ion Collider Experiment (ALICE)

A Large Ion Collider Experiment (ALICE) [Fig. 2.2] is the only major LHC experiment dedicated for heavy-ion collisions to study the properties of matter at extreme high energy densities. It can identify particles in a wide momentum range (100 MeV to 100 GeV) and high multiplicity environment (8000 charge particles per unit rapidity) [1]. The experiment have many detectors which can be broadly grouped in two classes, central and forward detectors.

In ALICE the beam interaction point is taken as the origin and a right-handed orthogonal Cartesian system [2] is used to define its global coordinate system. Beam direction is the z-axis (Muon Spectrometer direction is taken to be negative

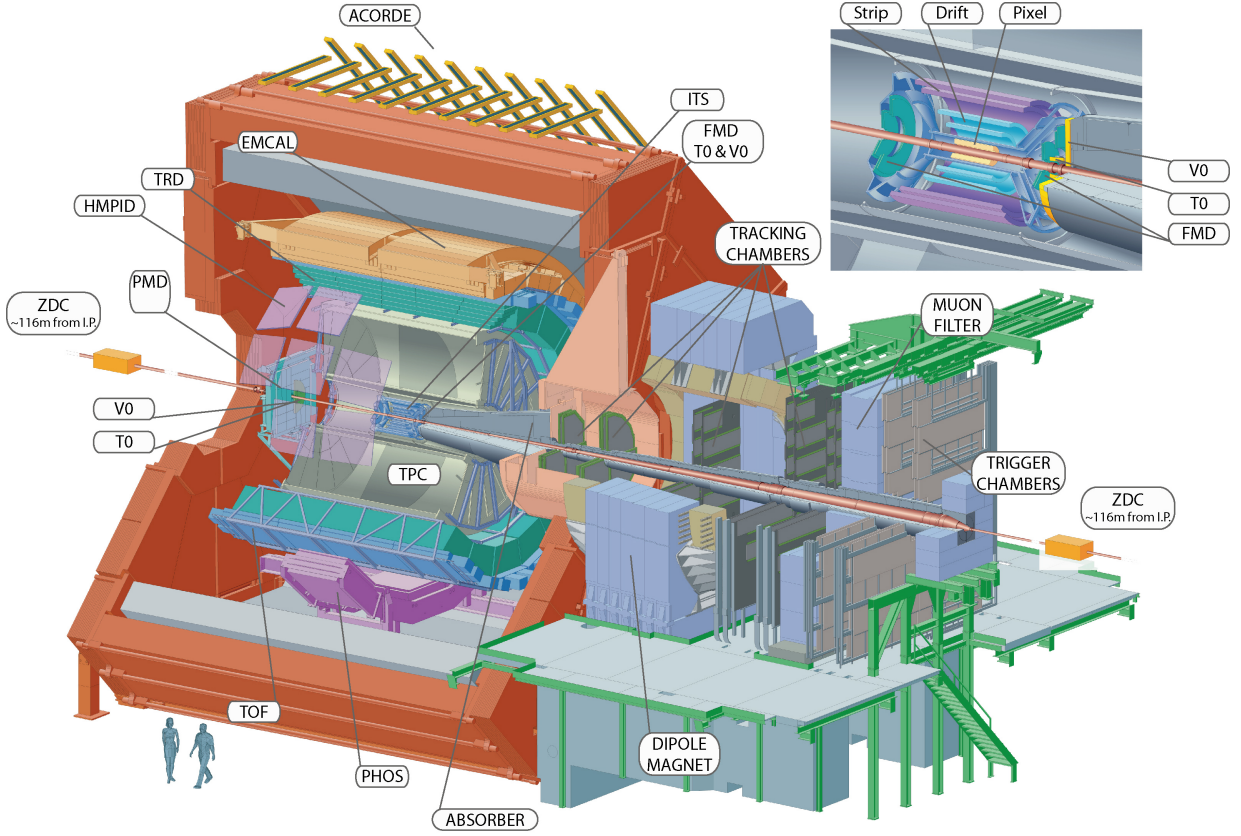


Figure 2.2: Schematic view of the ALICE experiment.

z-axis). The x-axis is perpendicular to the z-axis and points towards LHC ring center, while y-axis is perpendicular to the x-axis and z-axis pointing upwards.

The ALICE detector has been discussed in some details in the following sections.

2.3 Central Barrel Detectors

The central barrel detectors are in the rapidity coverage $-0.9 \leq \eta \leq 0.9$ and are placed inside the L3 magnet. These detectors are used in wide variety of measurements such as vertex reconstruction and particle identification. The brief description of the different central barrel detectors are as follows:

2.3.1 Inner Tracking System (ITS)

The Inner Tracking System (ITS) [3] is composed of six cylindrical layers with inner and outer most radii 4 cm and 43 cm respectively covering an acceptance of $1.98 \leq |\eta|$ [Fig. 2.3]. It is the inner most detector closest to the interaction point and provides primary vertex resolution better than $100 \mu\text{m}$ and reconstruction of secondary vertices (e.g. B, D decays). The six layers of the ITS are grouped in three pairs of, Silicon Pixel Detector (SPD), Silicon Drift Detector (SDD) and Silicon Strip Detector (SSD). The SPD is the inner most layer, which can run at a rate of 1 kHz and handle up to $80 \text{ particles}/\text{cm}^2$. On the other hand both SDD and SSD can provide particle identification by measuring energy loss of the charge particles traversing the detector material and can handle up to $7 \text{ particle}/\text{cm}^2$ and $1 \text{ particle}/\text{cm}^2$, respectively.

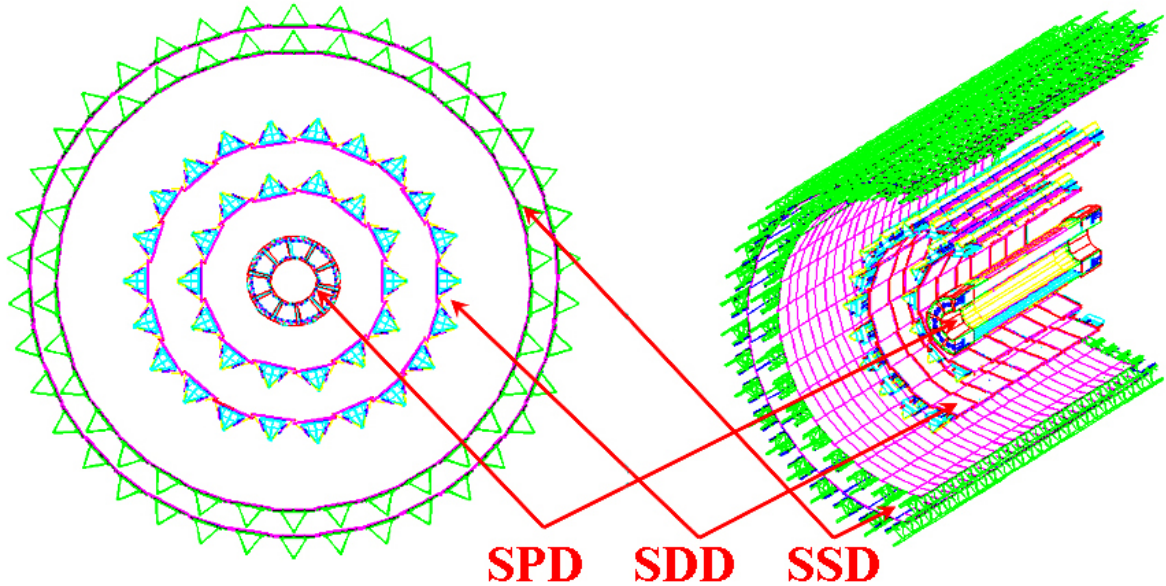


Figure 2.3: Layout of the Inner Tracking System (ITS).

2.3.2 Time Projection Chamber (TPC)

The Time Projection Chamber (TPC) [4] is a 500 cm long hollow cylinder along the beam direction around ITS with an inner radius of 85 cm and outer radius 250 cm [Fig. 2.4]. It is the central tracking device for the charge particles in ALICE. The hollow cylinder is filled with a gas mixture of Ne, CO₂, N₂ in a ratio of 85:10:5 at atmospheric pressure. Charge particle crossing the gas of the TPC ionize the gas atoms along their path, liberating electrons that drift towards the end plates of the detector. The momentum dependence of the energy loss caused by the fast charged particles passing through the gas medium can be used for particle identification [Fig. 2.5]. Low momentum particles (up to few GeV) can also be identified by TPC along with TOP, TRD, ITS by measuring the dE/dx .

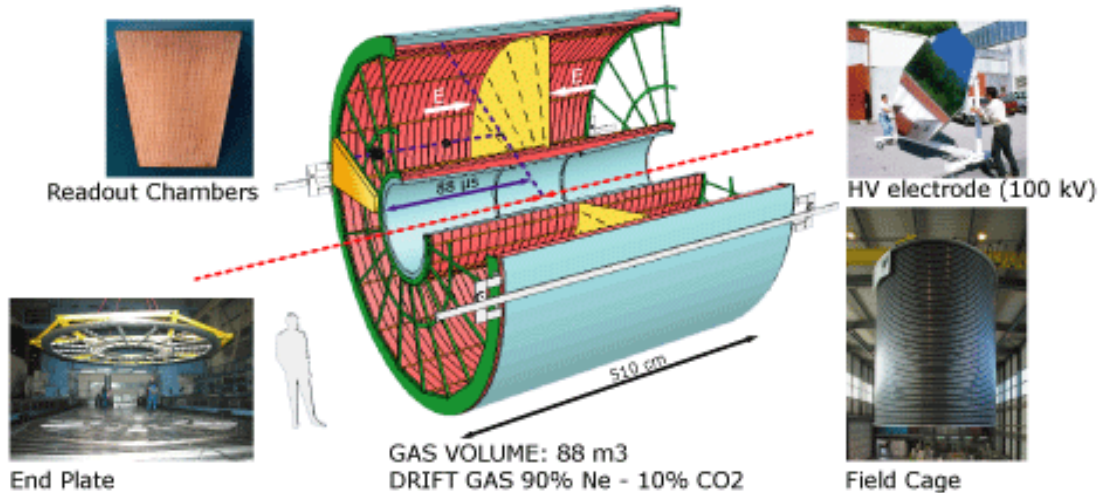


Figure 2.4: Layout of the Time Projection Chamber (TPC).

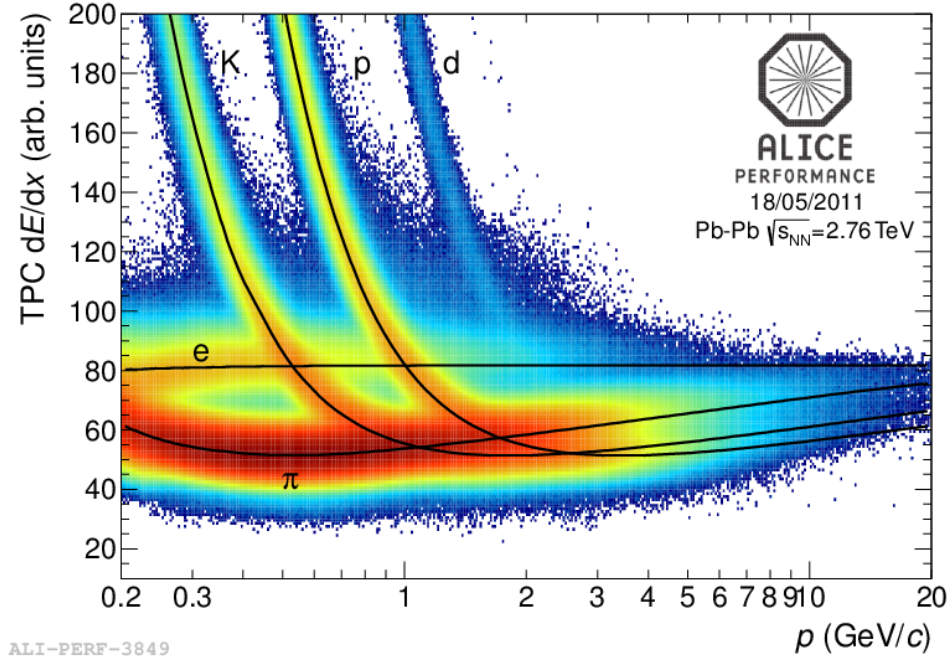


Figure 2.5: Energy loss in the TPC as a function of momentum with superimposed Bethe-Bloch lines for various particle species.

2.3.3 Transition Radiation Detector (TRD)

The Transition Radiation Detector (TRD) [5] consists of 6 layers between 260 cm to 370 cm and is located between the radial space between the TPC and TOF [Fig. 2.6]. It can identify electrons with momenta higher than 1 GeV/c from pions, where the energy loss mechanism of TPC is no longer effective. When a relativistic charge particle passes through the boundary of two media with different dielectric constant, it emits transition radiation (TR). Since the pion is heavier, their ionization loss is smaller than electron causing no transition radiation below ~ 100 GeV/c. The TRD uses this principle to separate electron from pions.

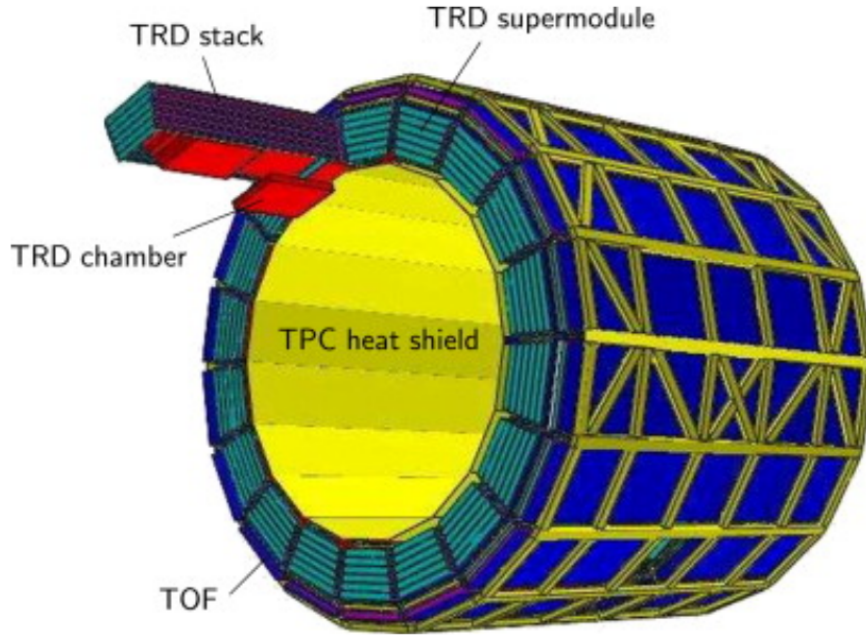


Figure 2.6: Illustration of TRD surrounded by TPC and TOF.

2.3.4 Time of Flight (TOF)

The Time Of Flight (TOF) [6] is segmented in 18 super modules in ϕ and 5 in z direction, the TOF measures the particle time of flight with an overall resolution better than 80 ps. It is the outermost detector having a full azimuthal coverage and a longitudinal acceptance of $|\eta| < 0.9$. By the combination of this information with the particle momenta it is possible to determine their masses. The TOF provides particle identification in the intermediate momentum region: a separation of better than 3σ can be achieved below 2.5 GeV/c for pions and kaons and below 4 GeV/c for kaons and protons. The detector is made of Multi-gap Resistive Plate Chambers (MRPC). They are gaseous detectors with high and uniform electric field where the ionization immediately starts the avalanches without any drift. They can operate at atmospheric pressure and with high gain due to the internal quenching capabilities of the resistive plates. The TOF detector delivers trigger

signals as well. It provides Level-0 (L0) triggers to select ultra-peripheral collisions, minimum bias events in pp collisions and cosmic muons for the calibration of central detectors and cosmic ray physics.

2.3.5 Photon Spectrometer (PHOS)

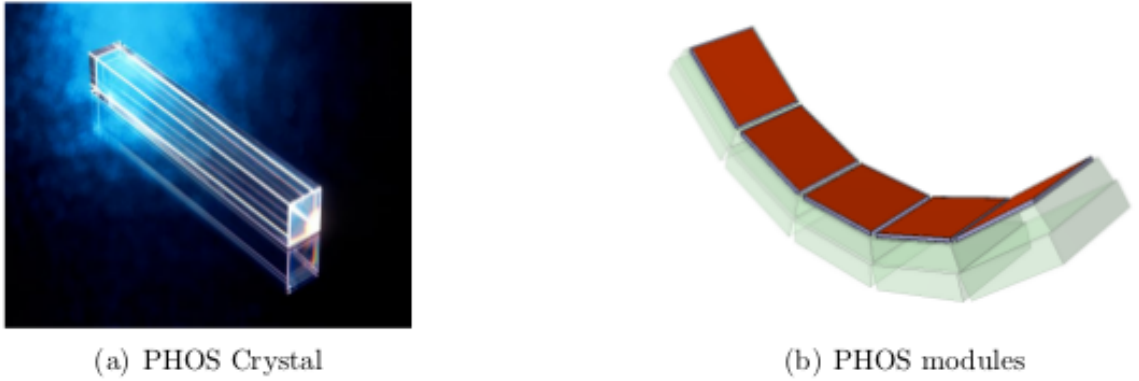


Figure 2.7: The PHOS crystal and assembled module.

The PHOton Spectrometer (PHOS) [7] is divided into five independent modules of a segmented electromagnetic calorimeter and a Charged-Particle Veto (CPV) detector. It is a high-resolution electromagnetic spectrometer covering 100 degree in azimuth and $|\eta| < 0.12$, placed at the bottom of the ALICE setup at a distance of 460 cm from the interaction point. Each calorimeter consists of 56 rows of 64 cells of PbWO_4 crystals. Fig. 2.6 shows a 3D schematic view. The CPV is a Multi-Wire Proportional Chamber with a charged-particle detection efficiency better than 99%. The PHOS is designed to provide photon identification, as well as neutral meson identification, through the two-photons decay channel.

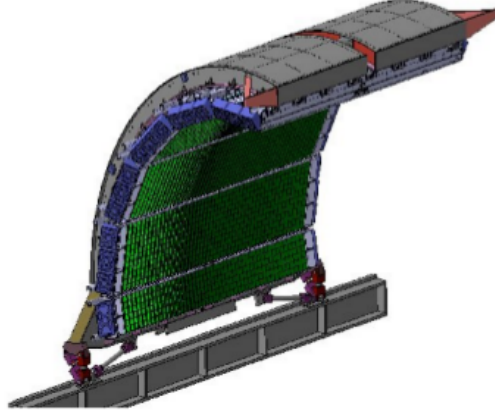


Figure 2.8: The layout of ALICE EMCal.

2.3.6 Electromagnetic Calorimeter (EMCal)

The Electromagnetic Calorimeter (EMCal) [8] is located 4.5 m away from the beam line with an azimuthal acceptance coverage of 110 degree and $|\eta| < 0.7$, limited by the PHOS and the HMPID (Fig. 2.6). It enhances the ALICE capabilities for high-energy jet measurements by improving jet energy resolution. It also increases the capabilities to measure high momentum photons and electrons. The chosen technology is a layered Pb-scintillator sampling calorimeter with alternating layers of 1.44 mm of lead and 1.76 mm of scintillator.

2.3.7 High Momentum Particle Identification Detector (HMPID)

The High Momentum Particle Identification Detector (HMPID) [9] is optimized to extend the range for π/K and K/p discrimination, on a track-by-track basis, up to 3 GeV/c and 5 GeV/c respectively. It enhances the PID capability of ALICE by enabling the identification of particles beyond the momentum interval attainable through energy loss (in ITS and TPC) and time of flight measurements (in TOF).

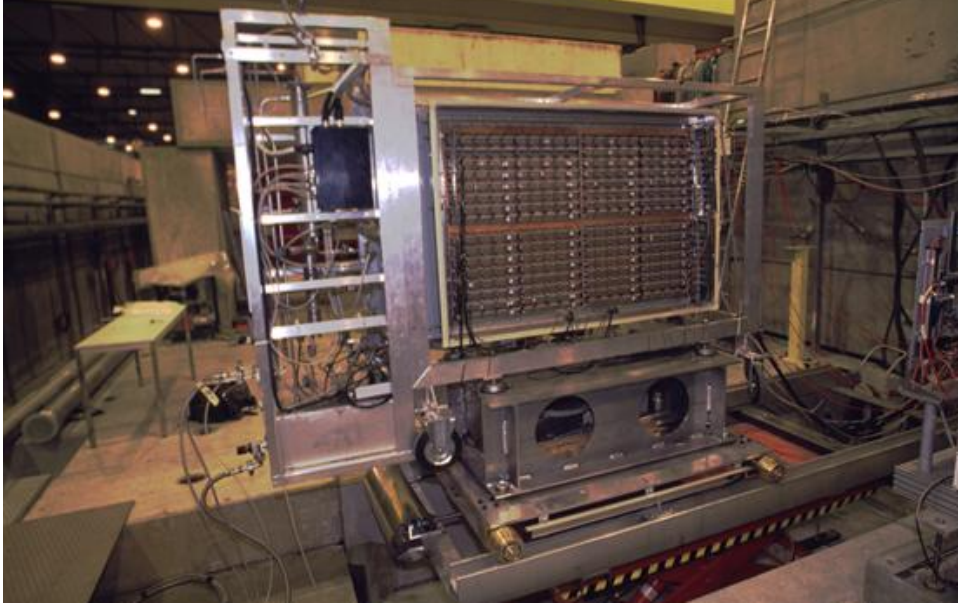


Figure 2.9: The schematic diagram of HMPID modules setup in ALICE.

The detector is designed as a single-arm array with a pseudo-rapidity acceptance of $|\eta| < 0.6$ and an azimuthal coverage of about 58 degree which corresponds to 5% of the central barrel phase space. It is based on Ring Imaging Cherenkov counters and consists of seven modules of about $1.5 \times 1.5 \text{ m}^2$ each (see Fig. 2.6).

2.4 Forward Detectors

The ALICE forward detectors are generally used for the centrality determination of a AA collision and the multiplicity evaluation in pp, pA and AA collisions. These measurement of the centrality and multiplicity is useful to understand the global characteristic of the event. A brief description of these detectors are given below:

2.4.1 Forward Multiplicity Detector (FMD)

The Forward Multiplicity Detector (FMD) [10] consists of silicon strip detectors divided in seven disks perpendicular to the beam pipe and placed at distances between 42 cm and 225 cm from the interaction point. It provides charged particle multiplicity information in the pseudorapidity range $1.7 < \eta < 5.1$ (A-side) and $3.4 < \eta < 1.7$ (C-side). In Fig. 2.10 a schematic view is presented.

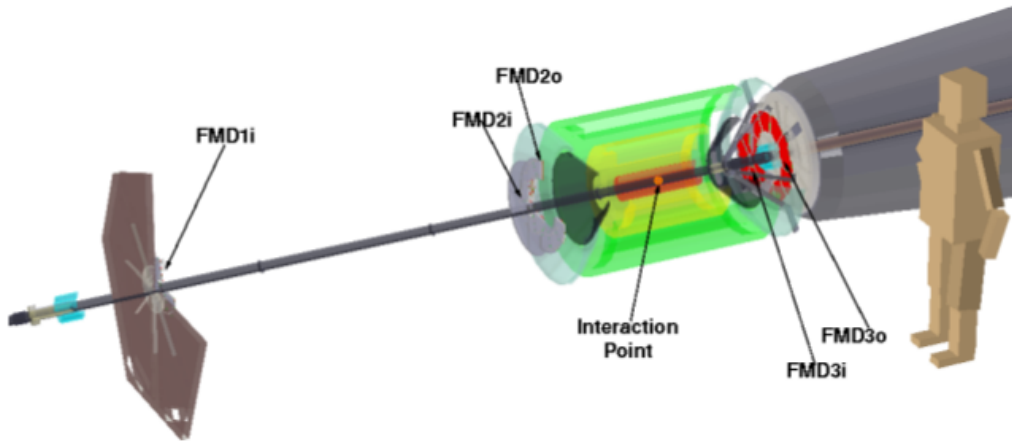


Figure 2.10: The schematic diagram of FMD.

2.4.2 VZERO Detector (V0)

The VZERO detector (V0) [10] is segmented into 64 elementary counters distributed in 8 rings, covering two pseudorapidity ranges: $2.8 < \eta < 5.1$ and $3.8 < \eta < 1.7$. It is made of two arrays of scintillator material, located at 340 cm (A-side) and 90 cm (C-side) from the interaction point (Fig. 2.11). The measurement of the time difference between the two subsystems allows to identify and reject the beam-gas events, thus providing a minimum bias trigger for the central barrel detectors and a validation signal for the Muon Trigger. The V0 can also measure the charged particle multiplicity, acting as a centrality indicator for AA

collision analysis.

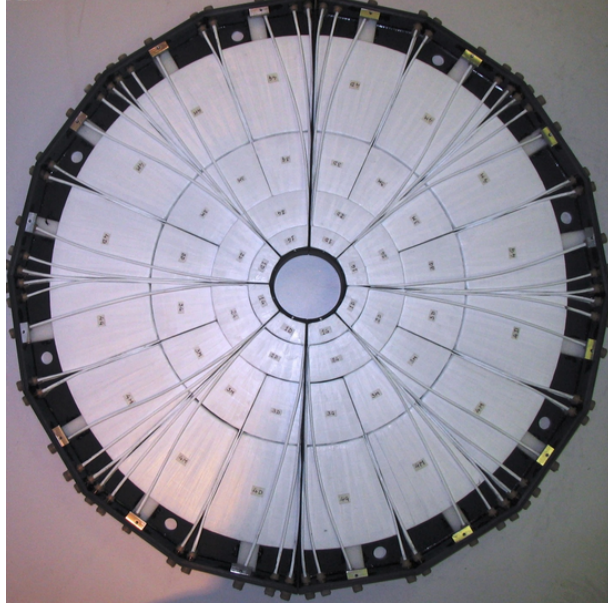


Figure 2.11: The schematic diagram of the V0 detector.

2.4.3 TZERO Detector (T0)

The TZERO detector (T0) [10] is designed to provide a start signal for the TOF detector, to measure the vertex position along the beam axis with a precision of ± 1.5 cm and to measure the particle multiplicity, generating a centrality trigger. It consists of two arrays of Cherenkov counters, with a time resolution better than 50 ps, asymmetrically placed at 375 cm (A-side) and 72.7 cm (C-side) from the interaction vertex, with a pseudorapidity coverage of $4.61 < \eta < 4.92$ and $3.28 < \eta < 2.97$ respectively (Fig. 2.12).

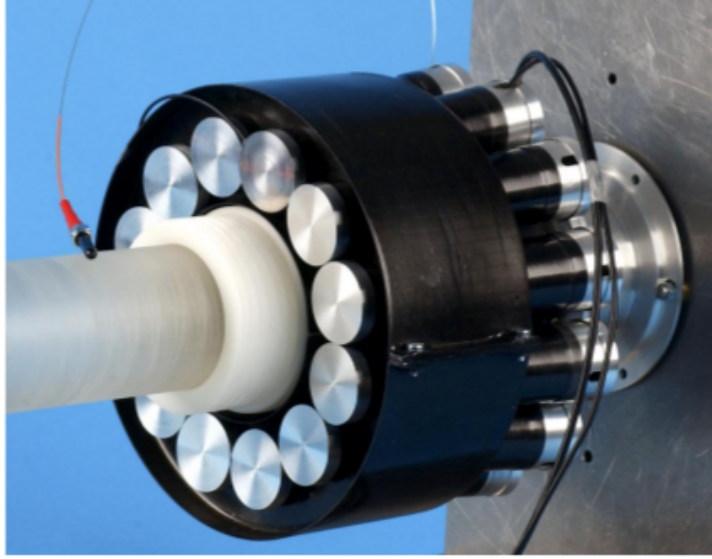


Figure 2.12: The view of T0 module of ALICE.

2.4.4 Photon Multiplicity Detector (PMD)

The Photon Multiplicity Detector (PMD) [11] is about 360 cm from the interaction point, in A-side, its main goal is the estimate of the transverse electromagnetic energy and the reaction plane on an event-by-event basis for AA collisions analysis. It is a pre-shower detector measuring the multiplicity and spatial distribution of photons in the forward region ($2.3 < \eta < 3.7$). It consists of two identical planes of detectors, made of gas proportional counters with honeycomb structure and wire readout (Fig. 2.13).

2.4.5 Zero Degree Calorimeter (ZDC)

The Zero Degree Calorimeters (ZDC) [12] consists of two pairs of quartz-fiber hadronic calorimeters (for neutrons and protons), placed on both sides of the interaction point, at 116 m from it. It provide a centrality estimate and trigger in

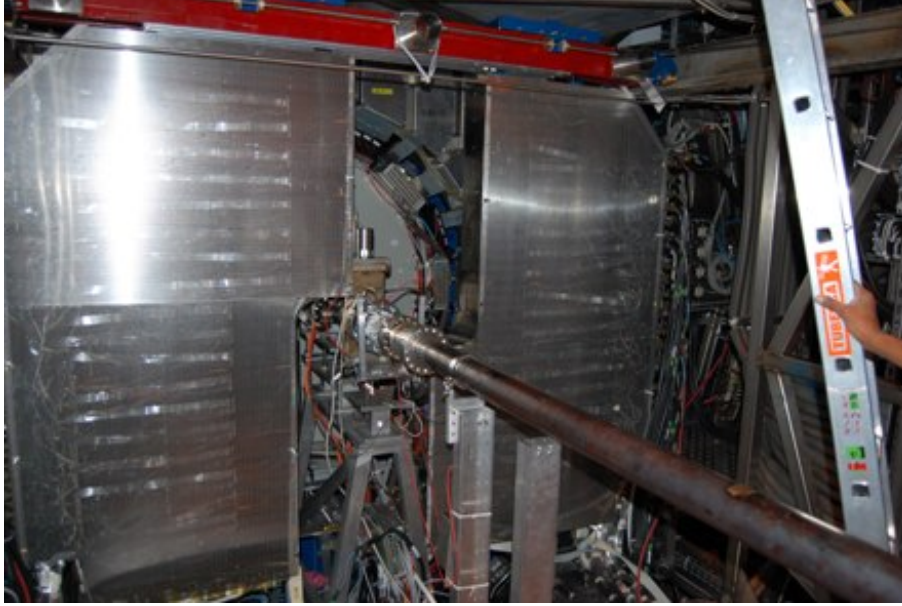


Figure 2.13: The setup of PMD detector in ALICE.

Pb–Pb collisions by measuring the energy carried in the forward direction (at zero degrees with respect to the beam direction) by noninteracting nucleons (spectators)(Fig. 2.14). The ZDC system presents also two electromagnetic calorimeters (ZEM), both placed at about 7 m from the IP (PMD side), which allow to resolve ambiguities in the determination of the centrality. The ZEM, made of lead and quartz fibers, are designed to measure the energy of particles, mostly photons generated from π^0 decays, at forward rapidities ($4.8 < \eta < 5.7$).



Figure 2.14: The setup of ZDC detector in ALICE.

2.5 The Forward Muon Spectrometer

The forward Muon Spectrometer [13] is in the rapidity range $2.5 < y < 4$ and can measure a wide range of transverse momentum down to $p_T = 0$. Its main goal is to study the charmonium (J/ψ and $\psi(2S)$) and bottomonium (Υ resonances), low mass vector mesons (ρ and ϕ), open heavy-flavours (D and B families) and weak bosons (Z, W^\pm), via their muonic decay channels in pp, pA and AA collisions at the LHC energies.

The Muon Spectrometer has a total length of 17 m and covers the polar angular range $172^\circ < \theta < 178^\circ$ ($4.0 < \eta < 2.5$) with respect to the ALICE reference frame [14]. It is composed of absorbers, five stations of tracking detectors that, together with a warm dipole magnet, are used to track muons and to measure their momenta and two stations of trigger chambers shielded by a muon filter as shown in Fig. 2.15.

This thesis uses the data from this sub-detector. Thus, a more detail description

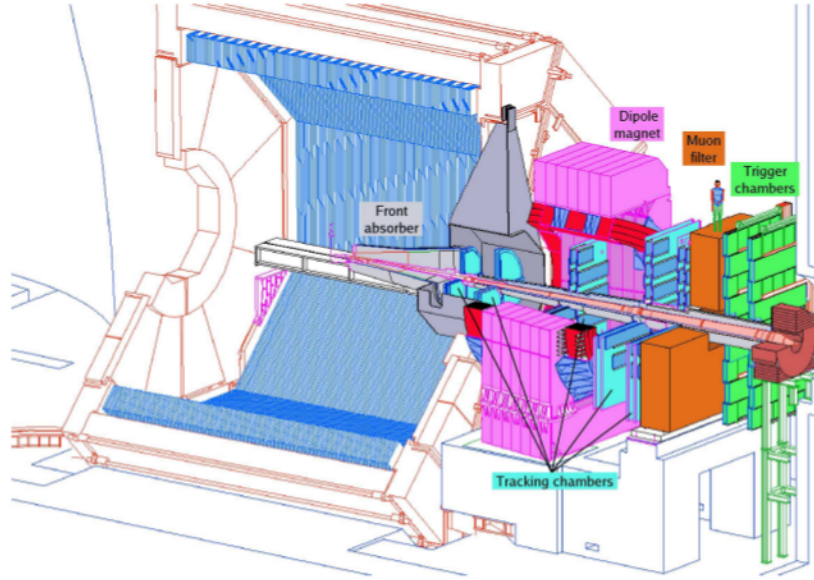


Figure 2.15: The basic layout of the Forward Muon Spectrometer of ALICE.

has been presented below.

2.5.1 Front Absorber

The front absorber is located at 90 cm from the IP, inside the L3 magnet, it is designed to limit multiple scattering and energy loss by traversing muons, but also to protect other ALICE detectors from secondary particles produced within the absorbing material [15]. It is made out of carbon, concrete and steel with a conical geometry, for a total length of 4.13 m (corresponding to ~ 10 radiation lengths), as shown in Fig. 2.16. It is covered by a 10 mm layer of tungsten at the front end of the cone (close to ITS) and in the sector between 10.5° and 12.5° where it faces TPC. A tungsten cover of 100 mm thickness at the back end absorbs most of the low energetic electrons created inside the absorber. An additional ring of 100 mm of tungsten is added to the 2° cone to improve the shielding against particles from the beam pipe. Finally, three layers of polyethylene are placed at

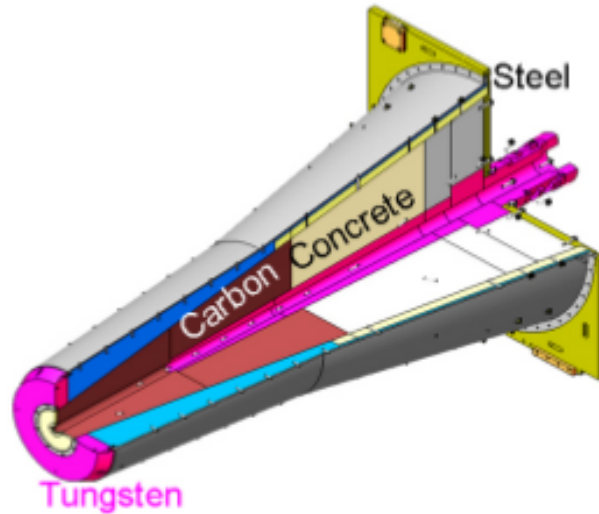


Figure 2.16: The Front Absorber of ALICE.

the end of the absorber for stopping slow neutrons.

2.5.2 Muon Filter

There is another absorber called Muon Filter, located between the Muon Tracking and the Muon Trigger, 14.5 m from the IP. It is a 120 cm thick wall made of cast iron, whose aim is to reduce the background on the Muon Trigger stations. It absorbs hadrons and low-momentum muons: the combined effect of the front absorber and the muon filter prevents muons with $p < 4$ GeV/c from reaching the Muon Trigger chambers. The muon filter is shown in Fig. 2.17 along with the warm dipole magnet.

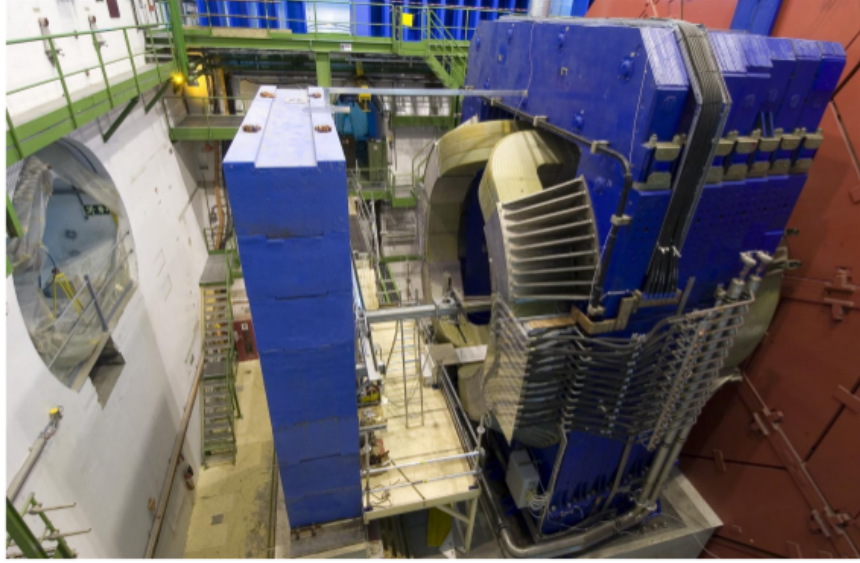


Figure 2.17: The picture of Muon Filter (left) and Dipole Magnet (right) of ALICE.

2.5.3 Dipole Magnet

The world's largest dipole magnet houses the third Muon Tracking station and provides the bending power necessary to measure the transverse momenta of muons. It is located at about 10 m away from the IP and has an integral field of 3 T.m. The general concept of the magnet is based on a window-frame return yoke, fabricated from low-carbon steel sheets. Its overall dimensions are 5 m in length, 7 m in width and 9 m in height, with a total weight of about 890 tons [16]. The magnet is also used as a support for the front absorber and beam shield. An additional radial space of 10 cm to 15 cm is provided to house the support frames of the Muon Tracking chambers inside the magnet. The dipole has an angular acceptance of $171^\circ < \theta < 178^\circ$ and is designed to provide a horizontal magnetic field perpendicular to the beam axis. The field polarity can be reverted within a short time. A view of this warm dipole magnet is shown in Fig. 2.17.

2.5.4 Beam Shield

The beam shield is an absorber made of high Z tungsten-lead mixture embedded in a 4 cm thick stainless steel envelope, which surrounds the beam pipe along the Muon Spectrometer. Its shape follows the 178° acceptance line up to a maximum radius of 30 cm and then it stays constant. It stops the small angle particles and secondary ones emerging from the beam pipe.

2.5.5 Tracking Stations

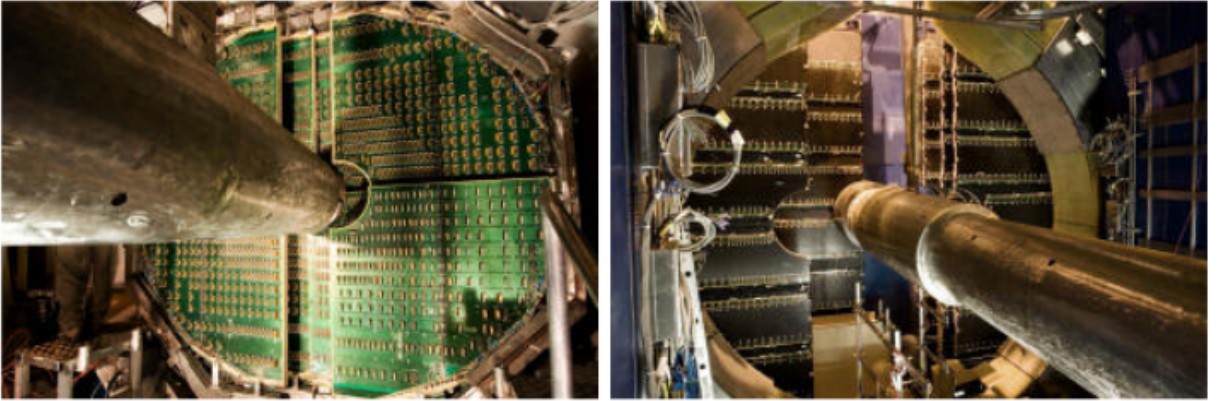


Figure 2.18: The picture of Tracking Station of ALICE.

The tracking detector system of Muon Spectrometer is composed of ten tracking chambers, and each pair of detection chamber is considered as one station. It is ~ 1000 cm long starting from ~ 500 cm of the interaction point (IP). On each side of the dipole magnet there are two stations with one remaining station situated at the middle of the magnet as shown in Fig. 2.18. In central Pb-Pb collisions, a few hundred particles are expected to hit the muon chambers, with a maximum hit density of about $5 \times 10^2 \text{ cm}^{-2}$. Moreover, the tracking system has to cover a total area of about 100 m^2 . The basic design criteria of dimuon tracking chamber

is to cope with such high particle flux in the forward direction and to achieve a spatial resolution of about $100\ \mu\text{m}$ to distinguish the members of the resonance family. Both of the conditions are found to be satisfied by Cathode Pad Chambers (CPC). Therefore, the tracking detectors are comprised of segmented Cathode with anode wires in between and are operated following the principle of Multiwire Proportional Counters (MWPC) with gas mixture of Ar/CO_2 (80%/20%). The basic geometry of CPC is shown Fig. 2.19, in which both the cathode planes are divided into sensitive pads, which are used to determine the position of particle traversing the detector. As a charged particle passes through the active gas volume of the detector, it produces ionization along its trajectory and avalanche takes place when the primary electrons drift towards the nearest anode wire. The motion of the secondary electrons induces charge on the cathode pads and charge clusters are formed. The relative values of the induced charges and the absolute positions of the pads in a charge cluster are used to determine the position of the charged particle passing through the detector.

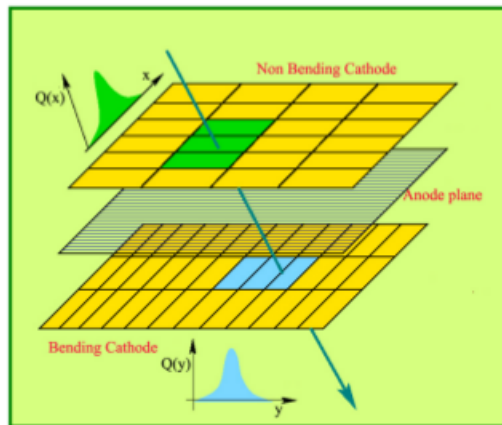


Figure 2.19: The basic working principle of cathode pad chamber.

Material budget is kept less than 3% of the radiation length to minimize the

multiple scattering of the muons in the chambers. Two different designs have been adopted for the different size of the stations (ranging from few square metres for station 1 to more than 30 m² for station 5). The first two stations have a quadrant structure, with the readout electronics distributed on their surface. For the other stations, a slat architecture has been chosen. The maximum size of a slat is 40×280 cm² and the electronics is implemented on the top and bottom sides of the slats. Thus, the slats have been overlapped to avoid dead zones on the detector. The position of the tracking chambers is continuously monitored by a sophisticated system of optical lines inspired by the RASNIK concept. The IR LED, a lens and a CCD camera constitutes the main components of each optical line. About 100 such optical lines are used to monitor the relative positions of the different chambers with better than 20 μ m accuracy, while 160 lines are used to monitor the planarity of the chambers.

2.5.6 Trigger Stations

The main purpose of the muon trigger system is to select unlike sign muon pairs from the decay of quarkonia resonances, single muons from heavy flavors and like sign muon pairs for the estimation of the combinatorial background studies. A loose p_T is applied at the trigger level on each individual muon to reduce the probability of triggering on events where low-pt muons are not accompanied by the high-pt ones (emitted in the decay of heavy quarkonia or in the semi-leptonic decay of open charm and beauty). For the study of quarkonia resonances, a dimuon trigger signal is issued when at least two tracks above a predefined p_T threshold are detected in an event. To perform the p_T selection, a position-sensitive trigger detector with space resolution better than 1 cm has been designed which can issue trigger within a very short time interval (~ 600 ns). This is achieved by

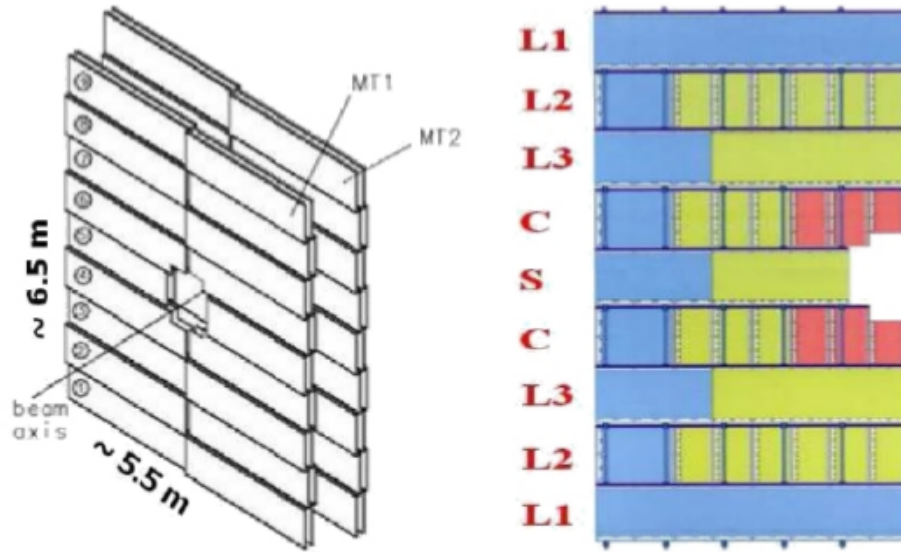


Figure 2.20: Layout of the ALICE Muon Trigger system. Different colours refer to the three strip widths.

Resistive Plate Chambers (RPCs) operated in streamer mode. The trigger system consists of four RPC planes arranged in two stations (MT1 and MT2), one metre apart from each other and placed behind the muon filter at about 1600 cm and 1700 cm, respectively, from the IP [Fig. 2.20]. Each trigger station is made of two parallel detection planes of 18 single-gap RPCs separated by 15 cm, so that the total number of RPCs is 72. The active area covered by the first station and the second are $6.12 \times 5.44 \text{ m}^2$ and $6.50 \times 5.78 \text{ m}^2$, respectively. A RPC is a planar geometry gaseous detector, where the active gas material is flushed through the resistive electrode plates. A High voltage is applied to the plate by means of a conducted layer coated on their outer surfaces. It is kept at a constant distance by plastic spacers placed inside the gas gap. The detector is filled with gas at atmospheric pressure, and kept in flow mode. The voltage required for operation is 4-5 kV/mm. When an ionising particle crosses the gas gap, the liberated elec-

trons give rise to a discharge on the anode, which are absorbed by organic gas and electronegative gases ($\text{Ar} + \text{C}_2\text{H}_2\text{F}_4 + \text{isobuthane} + \text{SF}_6$ at a ratio 49:40:7:1). Since duration of discharge (~ 10 ns) is much shorter than the relaxation time of the electrodes, they behave as an insulator through out the whole discharge. The signal can be picked up by induction method using insulated conductive strips placed on the electrodes.

2.6 Detector Readout

The tracking stations has front-end electronics which is based on a 16-channel indigenous Indian chip (MANAS), which includes the following functionalities: charge amplifier, filter, shaper and track & hold. The channels of four such chips are fed into a 12-bit ADCs, read out by the MARC chip which includes zero suppression. This chain is mounted on front-end boards (MANUs). A total of about 17,000 MANU cards are necessary to read the 1,076,224 channels of the tracking system. Up to 26 MANUs are connected (via PATCH bus) to the translator board which allows the data transfer to the Concentrator ReadOut Cluster Unit System (CROCUS). Each chamber is read out by two CROCUS, leading to a total number of 20 CROCUS. The main tasks of the CROCUS are to concentrate data from the chambers, to transport them to the DAQ and to perform control of the front-end electronics, including calibration and dispatching of the trigger signals. The data link that connects the top most readout element of the detector (i.e. CROCUS for dimuon tracking chambers) to the DAQ is called Detector Data Link (DDL). This scheme is shown in Fig. 2.21.

The dual-threshold front-end discriminators are used in the RPCs to adapted to the timing properties of the detector and reach the time resolution (1–2 ns)

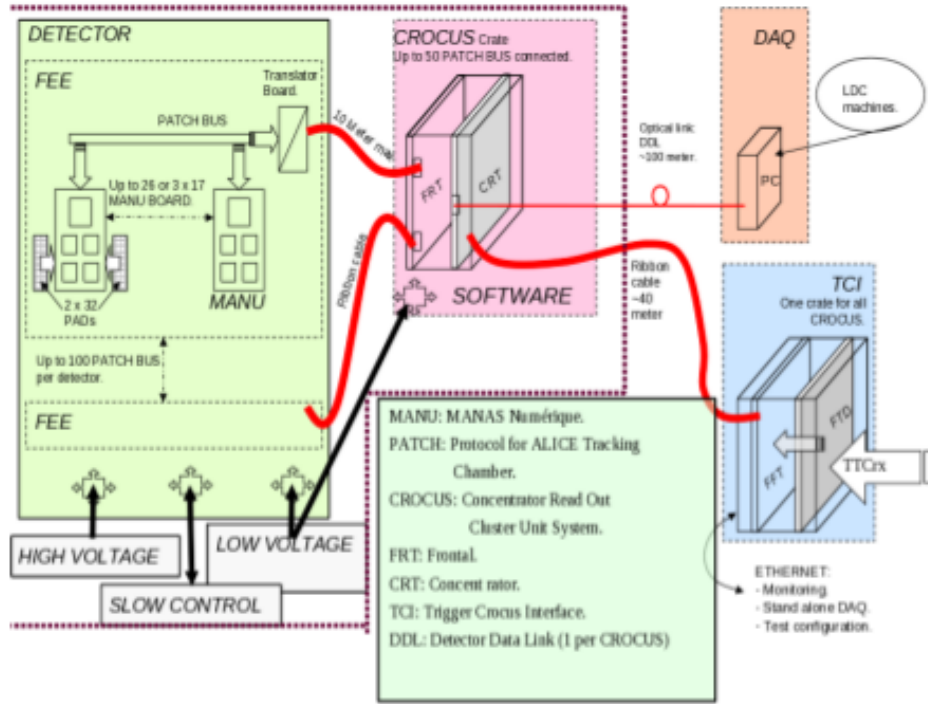


Figure 2.21: A schematic diagram for the detector readout of ALICE.

necessary for the identification of the bunch crossing. From the discriminators, the signals are sent to the trigger electronics (local trigger cards, based on programmable circuits working in pipeline mode) where the coordinates measured in the first and second stations are compared to determine the muon p_T . Due to the short decision time (600–700 ns) of the electronics, the dimuon trigger participates in the ALICE L0 trigger.

2.7 Online Control Systems

The experimental data collection is achieved by the Online Control System of ALICE. The various modules of the data collection system are discussed below:

2.7.1 Detector Control System (DCS)

The Detector Control System (DCS) [17] is developed by ALICE based on SCADA framework to control the detectors during data taking. It allows the shift crew to control the status of the detectors, issue alarms, check errors that could happen and have the possibility to recover possible failures in order to maximize the efficiency during the acquisition. Having to cope with a large variety of different subsystems and equipments, the DCS was designed to be flexible and modular, in order to give an easy environment to the sub-detector developers. The DCS is responsible of configuring, monitoring and controlling all the equipment of the experiment. It is also provided with a graphical user interface that shows the information from the detectors and allows the execution of commands.

2.7.2 Central Trigger Processor (CTP)

The Central Trigger Processor (CTP) [18] collects and processes the trigger signals from the detectors. Depending on the DAQ bandwidth and physics requirements it can select events having different features and downscale the data taking rates. The aim of the ALICE trigger is to manage the detectors which are busy for different periods following a valid trigger and to perform trigger selection optimized for several different running conditions. The fastest trigger signal, called Level 0 (L0), arrives within $1.2 \mu\text{s}$ after the collision. The L0 signals from the fastest detectors, such as the SPD, V0, T0 and the Muon Trigger, are treated with a three states logic (asserted, not relevant and negated) combined together with logic AND and OR in order to select a certain class of events. The information of slower detectors is used to create a Level 1 trigger signal (L1) that is dispatched after $6.5 \mu\text{s}$. The ALICE trigger system is provided with a past-future

protection circuit that looks for other events of requested types in a time windows before and after the collision under investigation. This is done for the rejection of pile-up events and the good read out of the detectors. The last level called Level 2 (L2), waits for the past-future protection and arrives after $88 \mu\text{s}$. The CTP data are stored in the raw data stream and in dedicated scalers. In particular, there are scalers for all the inputs and for each trigger class that store the scaled number of events passing each stage of the trigger (L0, L1, L2).

2.7.3 Data Acquisition System (DAQ)

The ALICE Data Acquisition system (DAQ) [17] was designed to handle large interaction rate and large amount of data (1.25 GB/s). Different clusters of detectors with different trigger rates can also be easily maintained by this DAQ. Once the CTP decides to acquire a particular event, the trigger signal is dispatched to the front-end read-out electronics (FERO) of the involved detectors. The data are then injected in the Detector Data Link (DDL4) and sent to a farm of computers, called Local Data Concentrators (LDC), that build the event fragments from the front-end electronics into sub-events. The sub-events are then shipped through an event building network to the Global Data Collectors (GDC) that take all the sub-events from the various LDCs to build the whole event and eventually send it to the storage facilities.

2.7.4 High Level Trigger (HLT)

The High Level Trigger (HLT) [19] can collect raw data from the LDC, to perform local pattern recognition, fast tracking and primary vertex localization, and to build up the global event. So, it can select interesting events as well as further

reduce the data size. The trigger decision and the compressed data are sent back to the DAQ via the HLT DDL output. In order to fulfil these requirements the HLT consists in a farm of more than 1000 multi-processor computers. The HLT also has an online event display that allows visualizing the events and monitoring the goodness of the data taking.

2.7.5 Data Quality Monitoring (DQM)

The Data Quality Monitoring (DQM) [20] provides online feedback of the data being recorded to ensure the acquisition of high quality data. It typically involves the online gathering of data samples, their analyses by userdefined algorithms and the visualization of the monitoring results. The final design of the DQM software framework of ALICE is AMORE (Automatic MONitoring Environment). This system is used to monitor the event data coming from the ALICE detectors allowing operators and experts to access a view of monitoring elements and to detect potential problems. Important features include the integration with the offline analysis and reconstruction framework, the interface with the electronic logbook that makes the monitoring results available everywhere through a web browser.

2.7.6 Detector Algorithms (DA)

The Detector Algorithms (DA) [21] provided by the detector teams allows to regularly calibrate the detectors to achieve most accurate physics measurements. Each DA accesses detector data (physics or calibration events) and produces results online. These results can be directly used (for example to configure the detector electronics or to give quality feedback to the DQM system) or shipped offline (to be processed and used in event reconstruction). A DA consists of a spe-

cific detector code to analyse events and to produce results according to a given calibration task, using a support library to interact with the external components (read configuration, grab events, log messages, export results, deal with the control system commands). There are two types of DA: the monitoring DA, which subscribe to events on the fly and the LDC DA, which analyse at end of run a locally recorded data file.

2.8 Offline Framework

The offline framework used by the ALICE community is a software called AliRoot. It can be used for simulation, reconstruction, detector alignment, calibration, visualization and data analysis. A short description of the ALICE offline framework is given below:

2.8.1 AliRoot

In 1998 the development of the ALICE offline project started by a software called AliRoot [22]. The AliRoot architecture is based on the ROOT [23] framework and it is designed to be extremely modular as shown in Fig. 2.22. This framework is completely based on the Object Oriented paradigm and it is entirely written in C++ with some makefiles for Fortran 90 to interface with GEANT. The STEER module provides steering, run management, interface classes and base classes. The detectors code is divided into independent modules which provide the syntax for simulation and reconstruction. The analysis code is continuously developed and progressively added to the framework. AliRoot is designed to easily interface with external Monte Carlo modules for the event generation and particle transport through the detector geometry.

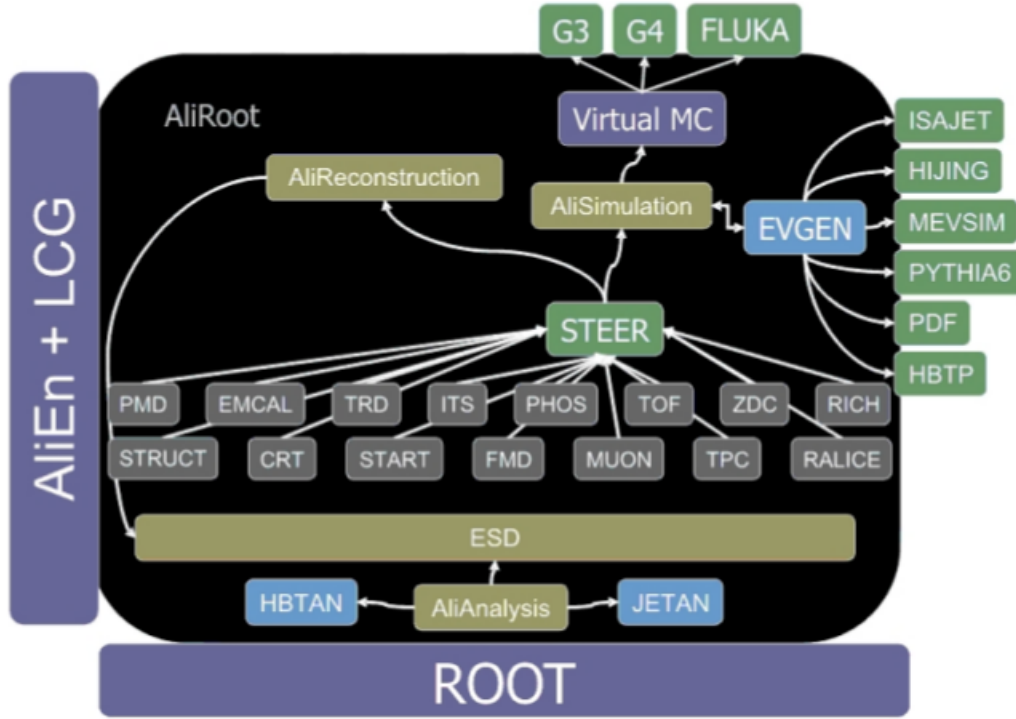


Figure 2.22: General scheme of the AliRoot architecture.

Simulation: In AliRoot the main simulation class is the AliSimulation. It provides the the interface to event generators (such as PYTHIA [24] or HIJING [25]) and to geometry builder (as detectors alignment and magnetic field). Users can also force the particles to be produced and to decay in a particular acceptance region in order to speed up the processes and tune their kinematic parametrizations (basically y and p_T needed to get the phase space of the particles) in the cases they are known.

Particle Transport: The AliRoot provides different Monte Carlo packages (like GEANT3 [26], GEANT4 [27] and FLUKA [28]) to obtain the detector response for the simulated events. The geometries of ALICE detectors are implemented by the detector groups in these packages, including support structures, absorbers, shielding and beam pipe. The magnetic field of the solenoid and the warm dipole

magnet can be described in the simulation as well. Ideal geometry is used as a default, but it is possible to work with a more reliable apparatus condition by retrieving the Offline Conditions Data Base objects (OCDB) which include pedestals, noisy or dead channels, HV values.

Reconstruction: The configuration of the reconstruction phase (for both the real data and Monte Carlo simulations) is provided by the class AliReconstruction. It gives the primary vertex reconstruction, track reconstruction and particle identification, secondary vertices reconstruction. The final output is an Event Summary Data (ESD), i.e. a .root file containing all the information relevant for physics analyses. During the production specific processes are possible such as the offline re-alignment of the tracking chambers. ESD could be further filtered for a more specific analysis and then stored in the Analysis Object Data (AOD) output files that are smaller in size and therefore give faster access for the users. The final stage of the filtering is the production of Muon AOD, which summarize all necessary information required for physics with the Muon Spectrometer.

2.8.2 The GRID

The computing facility called Grid [29] was started in CERN to distribute the enormous amount of data produced by the experiments around the world. The ALICE computing infrastructure, along with the other LHC experiments, belongs to the program coordinated by the Worldwide LHC Computing Grid (WLCG). This infrastructure, based on the MONARC [30] model, is hierarchical and the levels are called Tiers. The raw data from the experiment are stored in the very large computing center at CERN, the Tier-0, then data are replicated in regional large computing centers, called Tier-1 that also participate to the reconstruction and the storage of Monte Carlo data. The local computing centers, i.e. the resources of the

participating institutes, are the Tier-2. Although with smaller data storage capabilities, the Tier-2 contribute with computing power for the user data analysis tasks and the Monte Carlo simulations. The lowest levels of this infrastructure are the Tier-3 and Tier-4, local computing clusters of University departments and user's workstations respectively. For the present thesis, all the analysis jobs were carried out from Saha Institute of Nuclear Physics (SINP) with a dedicated ethernet link to CERN through the Tier-2 cluster of Variable Energy Cyclotron Centre (VECC). The interconnections between all these different facilities are possible through the Grid Middleware. ALICE developed a set of Middleware services called AliEn [31]. Through the AliEn User Interface (the MonALISA [32] repository for ALICE), the user interacts with the Grid: after authentication, he can access and store files as in a Unix like system, send own tasks (jobs) for analysis or simulation purposes and monitor their execution.

Bibliography

- [1] The ALICE Collaboration. The ALICE experiment at the CERN LHC. JINST, 3(08), 2008.
- [2] L. Betev et al. Definition of the ALICE coordinate system and basic rules for sub-detector components numbering. ALICE-INT, 2003-038, 2003.
- [3] The ALICE Collaboration. ITS Technical Design Report. CERN-LHCC, 99-12, 1999.
- [4] The ALICE Collaboration. TPC Technical Design Report. CERN-LHCC, 2000-001, 2000.
- [5] The ALICE Collaboration. TRD Technical Design Report. CERN-LHCC, 2001-021, 2001.
- [6] The ALICE Collaboration. TOF Technical Design Report. CERN-LHCC, 2000-012, 2000.
- [7] The ALICE Collaboration. PHOS Technical Design Report. CERN-LHCC, 99-4, 1999.

Bibliography

- [8] The ALICE Collaboration. EMCAL Technical Design Report. CERN-LHCC, 2006-014, 2006.
- [9] The ALICE Collaboration. HMPID Technical Design Report. CERN-LHCC, 98-19, 1998.
- [10] The ALICE Collaboration. Forward Detectors: FMD, T0 and V0 Technical Design Report. CERN-LHCC, 2004-25, 2004.
- [11] The ALICE Collaboration. PMD Technical Design Report. CERN-LHCC, 99-32, 1999.
- [12] The ALICE Collaboration. ZDC Technical Design Report. CERN-LHCC, 99-5, 1999.
- [13] The ALICE Collaboration. The forward muon spectrometer. Addendum to the ALICE Technical Proposal. CERN-LHCC, 96-32, 1996.
- [14] The ALICE Collaboration. ALICE dimuon forward spectrometer: addendum to the Technical Design Report. CERN-LHCC, 2000-46, 2000.
- [15] S. Grigoryan. Contribution of Secondary π/K Mesons, Produced in the Absorber, into the Dimuon Background in Pb-Pb Collisions. ALICE Internal Note, 2002-06, 2002.
- [16] D. Swoboda. ALICE Muon Arm Dipole Magnet. ALICE Internal Note, 1999-06, 1999.

- [17] The ALICE Collaboration. Trigger, Data Acquisition, High-Level Trigger and Control System Technical Design Report. CERN-LHCC, 2003-062, 2003.
- [18] D. Evans et al. The ALICE central trigger processor. CERN-LHCC, 2005-038, 2005.
- [19] T. Alt et al. The ALICE high level trigger. J. Phys. G, 30:S1097-S1100, 2004.
- [20] A. Telesca et al. The ALICE Data Quality Monitoring System. Real Time Conference (RT), 2010 17th IEEE-NPSS, May 2010.
- [21] F. Carena et al. Online processing in the ALICE DAQ, the Detector Algorithms. J. Phys., 219:022004, 2010.
- [22] <http://aliweb.cern.ch/Offline>.
- [23] <http://root.cern.ch>.
- [24] S. Mrenna et al. PYTHIA 6.4 Physics and Manual. JHEP, 0605:026, 2006.
- [25] M. Gyulassy et al. HIJING 1.0: A Monte Carlo program for parton and particle production in high energy hadronic and nuclear collisions. Comp. Phys. Comm., 83(2-3):307-331, 1994.
- [26] M. Goossens et al. GEANT: Detector Description and Simulation Tool. CERN program library long write-up, W5013, 1994.
- [27] S. Agostinelli et al. Geant4 - a simulation toolkit. Nucl. Instrum. Meth. A, 506(3):250-303, 2003.

Bibliography

- [28] G. Battistoni et al. Applications of FLUKA Monte Carlo code for nuclear and accelerator physics. Nucl. Instrum. Meth. B, 269(24):2850–2856, 2011.
- [29] I. Foster et al. Morgan Kaufmann Publishers, 1999.
- [30] <http://monarc.web.cern.ch/MONARC>.
- [31] <http://alien2.cern.ch>.
- [32] <http://monalisa.cern.ch/monalisa.html>.

Chapter 3

Data Quality Assurance (QA)

In order to study the Quark-Gluon Plasma, we want to measure the nuclear modification factor (R_{AA}) of the Υ resonances. To measure R_{AA} , we need the measurement of Υ production both in Pb–Pb and pp collisions at same energy. The Pb–Pb data was at 2.76 TeV, where as the pp data 7 TeV. The idea was to measure the Υ cross section at 7 TeV and use that result along with the LHCb data points at forward rapidity to interpolate the forward-rapidity cross section of Υ at 2.76 TeV. However, this method was not used due to low statistics and availability of LHCb results of forward-rapidity Υ cross section at 2.76 TeV. This is discussed quite in detail in chapter 4 and chapter 5.

During the data taking period ALICE collected substantial amount of data for the physics analysis. But quality of all the data were not good due to contamination from various sources and detector inefficiencies. So some general trends were checked for a given data called Quality Assurance (QA) to verify the suitability of the data for the physics analysis. Only the QA checked data were used for the physics analysis. In this chapter the methods of QA will be discussed, as I have actively participated in the QA monitoring of pp and Pb–Pb data.

3.1 Muon Run Selection

ALICE is capable of collecting data in various detector configurations for different physics analysis. Thus depending on the physics interest various data partitions with different trigger configurations have been used. The run list for a specific period is made using ALICE-logbook [1], DAQ-logbook [2] entries and Run Condition Table (RCT) [3]. First a run list is made from the ALICE logbook with the following basic criteria:

- (i) Period: LHC11d/e/f/...
- (ii) Partition: PHYSICS_1 (or another partition)
- (iii) Duration: > 10 min
- (iv) Run Type: PHYSICS
- (v) L3/Dipole Magnet Current (kA): [-30/-6] or [+30/+6]
- (vi) GDC mStream Recording: Yes
- (vii) Beam Energy (GeV): [900..]
- (viii) Beam: Stable
- (ix) Trigger Detectors: at least MUON_TRG
- (x) Readout Detectors: at least MUON_TRG, MUON_TRK, SPD
- (xi) Shuttle: Done
- (xii) Shuttle Done for Readout Detectors and GRP

(xiii) Data Quality not bad for Readout Detectors (depending on the Run Coordinator, the Global Data Quality can be bad if the TPC is not in).

Runs which are very short (< 10 min) are rejected, since a proper QA of these runs can not be done due to lack of statistics. For Muon Spectrometer data, the muon trigger (MUON_TRG) and V0 must be present as the trigger detector, while muon trigger (MUON_TRG), muon tracker (MUON_TRK), V0 and SPD must be

present as the readout detectors in the partition. During Pb–Pb data taking period ZDC was also requested as readout detector. The related detector information are also taken into account from the DAQ-logbook entries while selecting the runs. In some cases the global data quality may be bad, but those runs are only rejected if that happens due to some fault in the muon detector, otherwise they are taken in the basic run list. The Run Condition Table (RCT) is also checked for further information (to cross check any suspicious issue in other sub-detectors and their QA output) for the selected runs, as it gives run quality for all sub-detectors, the beam settings (number of bunches, fill number, luminosity scan, etc.), the magnetic field, the global run quality (for central barrel analysis) and Muon quality (for muon analysis). The runs used for luminosity scans are not considered for Muon analysis.

GDC : The Global Data Collectors (GDC) receives all sub-events from a given event and assembles them into a complete event. Subsequently, these events are stored on a system called Transient Data Storage (TDS).

GRP : Besides the 18 sub-detectors of the ALICE experiment, two further pre-processors exist: one to retrieve HLT specific parameters and another for data not specific to a particular sub-detector but to the whole experiment, called Global Run Parameters (GRP). The parameters are taken from different sources like, DAQ, DCS, Trigger etc. GRP does not correspond to a detector, but may be used by any in order to retrieve any global information to be used in reconstruction.

OCDB : The Offline Conditions Database (OCDB) is the place where the calibration and alignment data is stored. It is not a "database" in the literal sense of the word (like Oracle, MySQL, etc): it is a set of entries in the AliEn file catalog that point to the physical entities (ROOT files stored in the various storage elements of the grid) containing the calibration and alignment data.

Shuttle : During data-taking the sub-detectors interact with several online systems (CTP, DAQ, DCS, ECS and HLT). Data is read out by DAQ as raw data streams produced by the sub-detectors. At the same time they also produce conditions data which is information about the detector status and environmental variables. Most of the conditions data could in principle be calculated from the raw data and extracted offline after data-taking. However, such an approach would require an additional pass over the raw data before the reconstruction which is not possible due to the limited computing resources. Therefore, conditions data is already extracted during data-taking running dedicated sub-detector algorithms in the online systems. For this purpose Shuttle framework has been developed, which performs the following tasks:

- copying of data in any format produced by the online systems DAQ, DCS, and HLT for each sub-detector;
- preprocessing of the data, e.g. consolidation, fitting;
- reformatting to ROOT format;
- storing in the Grid Offline Conditions DataBase (OCDB);
- indicating that a given run has been processed, which is a precondition to starting the reconstruction.

Fill : Fill is the time period between beam injection and beam dump at LHC ring.

Period : Period is the time period between two consecutive technical stops by LHC.

BP : Bus Patch (BP) sends control signals to the front end electronics to read out MANAS chip and receive digitized data from the MANU cards.

DDL : Detector Data Link (DDL) connects the topmost readout element of the detector to the DAQ.

DE : Detection Element (DE) is the detector component that can operate independently, e.g. quadrants for the 1st and 2nd stations and slats for the 3rd, 4th and 5th stations of Muon Chambers.

3.2 Definition of Quality

In the RCT each sub-detector are tagged with certain numerical values to denote the status/quality of those sub-detectors. For the Muon Chambers (MCH), the following definitions are used [4]:

(1) detector configuration is nominal, no major problem. The average number of cluster per track per chamber is above 0.9, some BP are missing not more. Usable for Physics.

(2) detector configuration is lower than nominal, thus the tracking efficiency is slightly reduced. The average number of cluster per track per chamber is above 0.75 (and below 0.9). Usable for Physics.

(3) detector configuration is not nominal, for instance a DDL is missing or high occupancy DE have appeared. The average number of cluster per track per chamber is below 0.75, thus the tracking efficiency is modified. Usable for Physics if simulations are done accordingly.

(4) detector configuration is not nominal, tracking efficiency is not understood. Not Usable for Physics.

(5) Less than 50% of the run reconstructed

(6) Luminosity scan or too few events in the run or other issue (pedestal, ...)

(7) Bad in pass1 (reconstruction issue)

- (8) No QA results (QA has to be run)
- (9) Bad in pass2 (reconstruction issue)
- (10) Shuttle failed

While for the Muon Trigger (MTR) Subsystems, the quality definitions was:

(1) Nominal detector configuration, full detector(maybe some strips missing), Usable for Physics(Green).

(2) Nominal detector configuration, missing trigger electronics(Local, Regional, DARC) or RPCs or Masks, Usable for Physics(Yellow).

(3) Problem occurred during Data taking(Orange).

(4) Not nominal detector configuration, Not usable for physics(Red)

(5) VDM || LUMI || LHC Op. || Tests, Not for Physics(Red)

After doing the QA of the selected runs from the run list, the quality of a run for the muon analysis are tagged in the RCT. The analyzers of Muons follow this RCT to select the good runs for physics analysis or to understand the quality of a particular run just looking at the numerical tag of Muon Quality as given bellow :

(1) Good run (2) Bad run (3) Pending run (4) Bad for passX (5) Low statistics (6) Waiting for passX (7) No QA output (8) Investigating (9) MCH or MTR missing.

3.3 Physics Event Selection

The physics selection (by means of AliPhysicsSelection class) is used to select collision candidates in all the data samples collected by ALICE. This class works at present for all pp, p-Pb and Pb-Pb runs. The class AliPhysicsSelection selects events that:

- (1) Have the correct event type (physics);
- (2) Have the interaction trigger, i.e. trigger on bunch crossings;

(3) Fulfill the online trigger condition, replayed using offline signals from reconstructed clusters;

(4) Are not flagged as beam-gas by either V0A or V0C;

(5) Are not flagged as beam-gas, based on the SPD clusters vs tracklets correlation;

(6) Are not identified as "debunched" events by the ZDC timing cut.

This class produces control histograms. These histograms show the amount of events that pass the event selection in the control triggers (beam-empty, empty-beam, empty-empty) and are useful for the background assessment. The physics selection cut is used in all physics analysis.

3.4 Muon QA for pp Collisions

The Muon QA was done for the pp runs to select the good runs for the pp analysis, which were used as a baseline for the Pb-Pb runs. Here only the QA done for the LHC11d period is discussed, however, QA for the other pp run periods are almost the same [5]. At first the runs were selected from the ALICE logbook. A total of 141 runs qualified the selection criteria (see Fig. 3.1), which corresponds to ~ 2.47 M unlike sign trigger named as, CMUU7B.

Out of these 141 runs the 156656, 156657, 156858, 156859 and 157259 were not reconstructed due to various issues in GRP or CTP or Config OCDB, which accounts ~ 67.94 K CMUU7B. Another two runs 157476 and 157645 was rejected due to large physics selection effect. Physics selection removed ~ 21 % CINT7B (Minimum Bias) and ~ 10 % CMUU7B (Unlike Sign) events, which was ~ 2 % for the CINT7I trigger.




















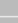








Runs filters	
Local filters 	
Period: LHC11d	 
Run Type: PHYSICS	 
Partition: PHYSICS_1	 
Duration: [10 m..]	 
L3 Magnet Current (kA): [-30..-30]	 
Dipole Magnet Current (kA): [-6..-6]	 
GDC mStream Recording: Yes	 
Other filters 	
Beam Mode: STABLE BEAMS	
Beam Energy (GeV): [3499..3501]	
Detectors: At least [MUON_TRG & V0] as Trigger At least [MUON_TRG & MUON_TRK & SPD & V0] as Readout	
MUON_TRG Quality Flag: (NOT) Bad run	
MUON_TRK Quality Flag: (NOT) Bad run	
SPD Quality Flag: (NOT) Bad run	
V0 Quality Flag: (NOT) Bad run	
Shuttle Done: Yes	
MUON_TRG Shuttle Done: DONE	
MUON_TRK Shuttle Done: DONE	
SPD Shuttle Done: DONE	
V0 Shuttle Done: DONE	

Figure 3.1: The criteria used for filtering the runs for LHC11d period from the ALICE logbook.

3.4.1 Minimum Bias Events

The CINT7B trigger represents the Minimum Bias events. The number of tracks per CINT7B trigger is shown in Fig. 3.2 on run-by-run basis for the LHC11d period. The trigger only tracks, tracker only tracks, matched tracks (trigger tracks able to find a tracker track in the tracker side) and all tracks (sum of the trigger only track, tracker only tracks and matched tracks) are denoted by blue, red, magenta and black colours respectively. It is apparent from the figure that there is a trend of decrease of matched tracks from beginning to the end of the period. However, the trigger tracks per CINT7B is ~ 0.015 – 0.020 (see Fig. 3.3), which is roughly constant throughout the period. At the start of each fill the tracker tracks are high and then it starts to decrease. This is due to beam-gas tracks or due to pile-up from other branches mainly since the MUON_TRK readout is longer than the time

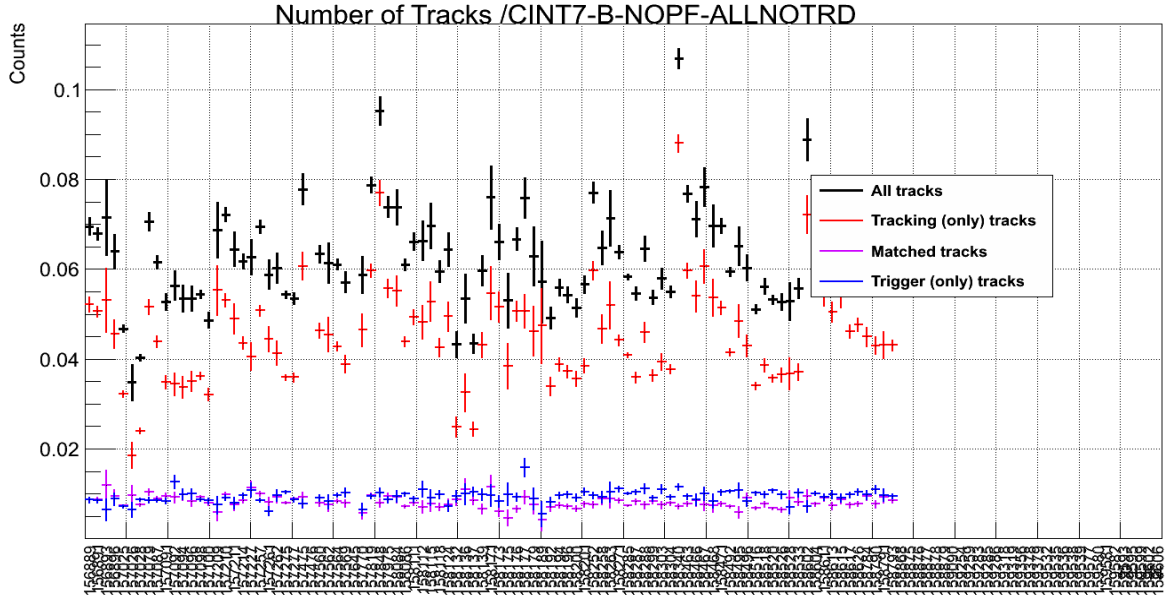


Figure 3.2: Run-by-run analysis of trigger only tracks, tracker only tracks and matched tracks per Minimum Bias (CINT7B) events.

between two branches. This effect is proportional to the beam luminosity and, hence, decreases within a fill.

3.4.2 Unlike Sign Dimuon Events

The CMUU7B denotes the Unlike Sign dimuon events, which means this events contains at least two muons of opposite charges. At the beginning of the period the number of matched tracks per CMUU7B was ~ 0.8 then decreases with time, ranging from ~ 0.5 – 0.8 throughout the period as shown in Fig. 3.4. However from Fig. 3.5 it is clear that while the number of trigger tracks remains constant throughout the period, the tracker tracks decreased with time. This implies the tracking chamber efficiency decreased with time. The matched tracks per CMUU7B was further analyzed for $p_T = 1$ and 2 GeV after applying the physics selection, vertex, R_{Abs} and pDCA cut (see Fig. 3.6). The trend of decrease in efficiency of tracking chambers remains for both the p_T cuts.

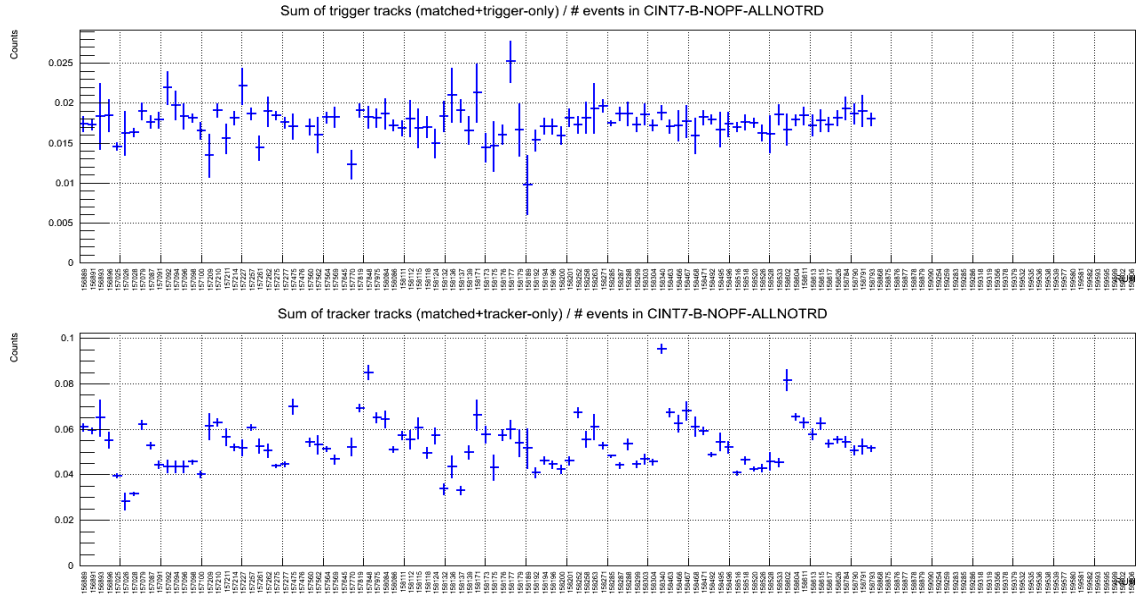


Figure 3.3: Run-by-run analysis of trigger tracks and tracker tracks per Minimum Bias (CINT7B) events.

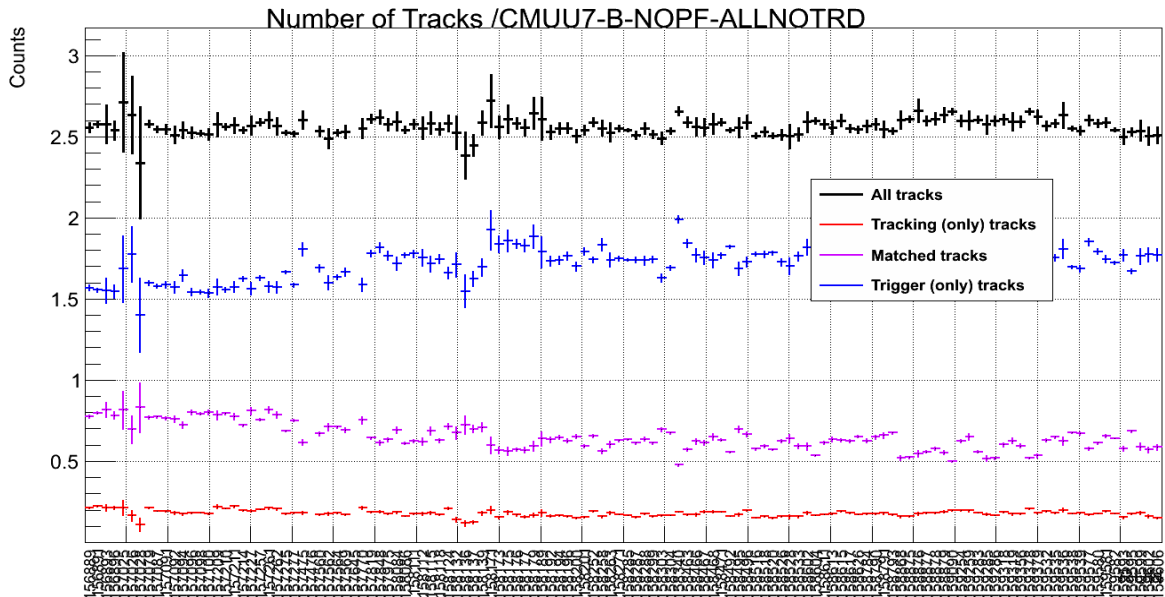


Figure 3.4: Run-by-run analysis of trigger only tracks, tracker only tracks and matched tracks per Unlike Sign dimuon (CMUU7B) events.

Chapter 3. Data Quality Assurance (QA)

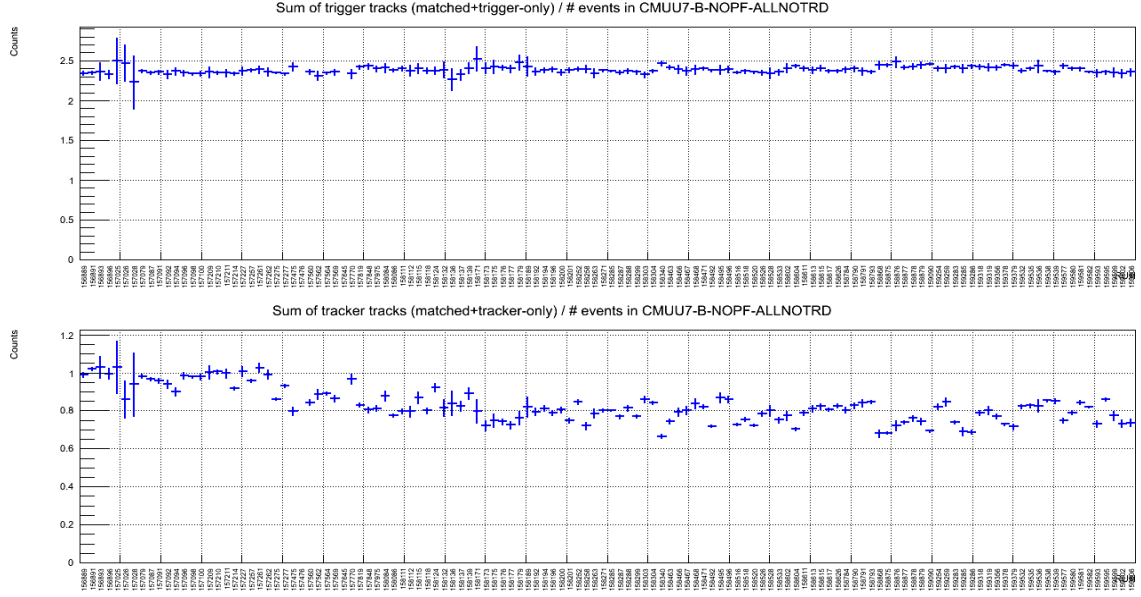


Figure 3.5: Run-by-run analysis of trigger tracks and tracker tracks per Unlike Sign dimuon (CMUU7B) events.

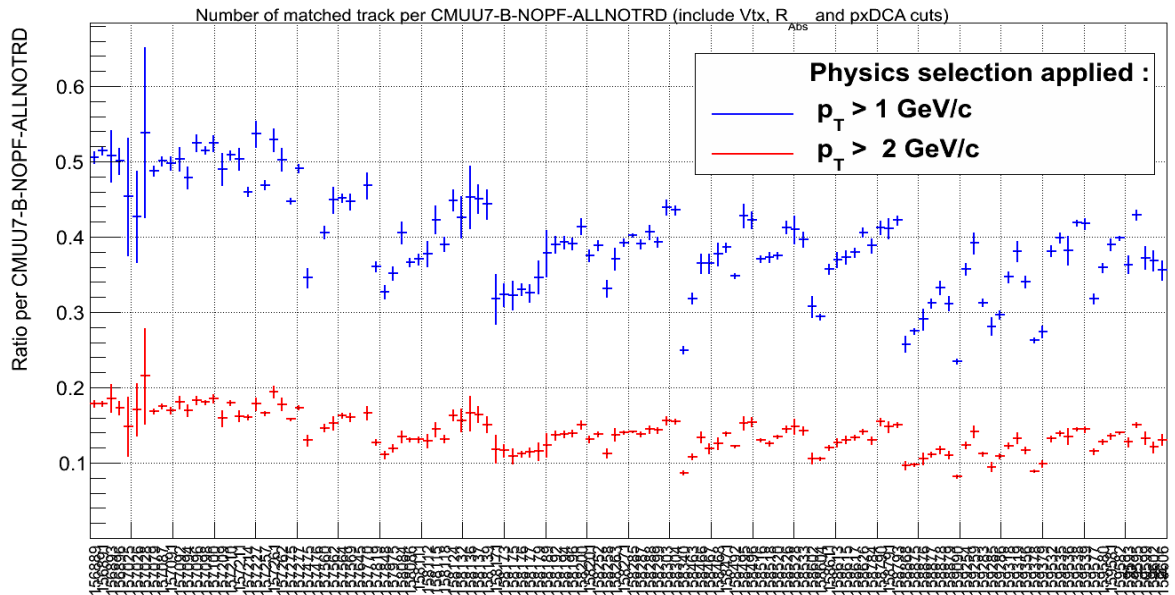


Figure 3.6: Number of matched tracks per CMUU7B after applying the $p_T = 1$ and 2 GeV cut.

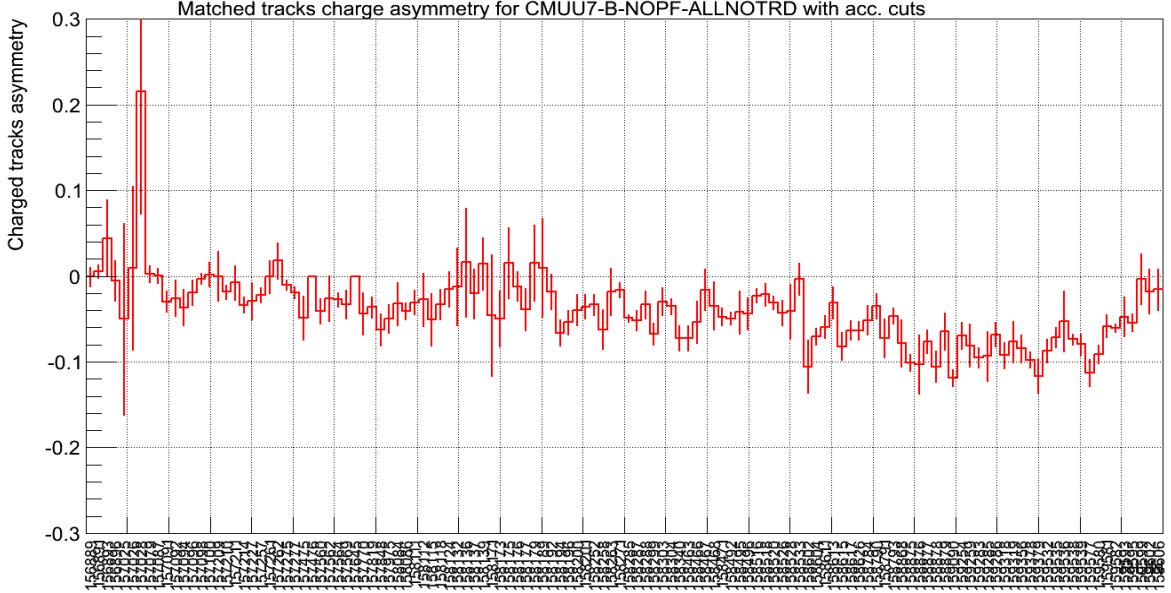


Figure 3.7: Charge asymmetry of the matched tracks for the CMUU7B trigger.

3.4.3 Charge Asymmetry and Beam-Gas Tracks

The charge asymmetry (Q_{asy}) of the match tracks was also analyzed. It is defined as:

$$Q_{\text{asy}} = \frac{M_p - M_n}{M_p + M_n} \quad (3.1)$$

where M_p and M_n are the number of positive and negative matched tracks, respectively. Since the cradles are placed symmetrically around the beam direction, it is expected that $Q_{\text{asy}} \sim 0$ if all portions of the detectors are equally efficient. However it can be observed from Fig. 3.7 that Q_{asy} becomes more negative with time, which indicates a decrease in efficiency (or loss of bus patches) on the top side of the Muon tracker compared to the bottom side.

The pDCA cut on the matched tracks are applied to identify the beam-gas tracks. It is found that there is a large amount of beam-gas effect through out the period, specially at the beginning of each fill (see Fig. 3.8), when the intensity

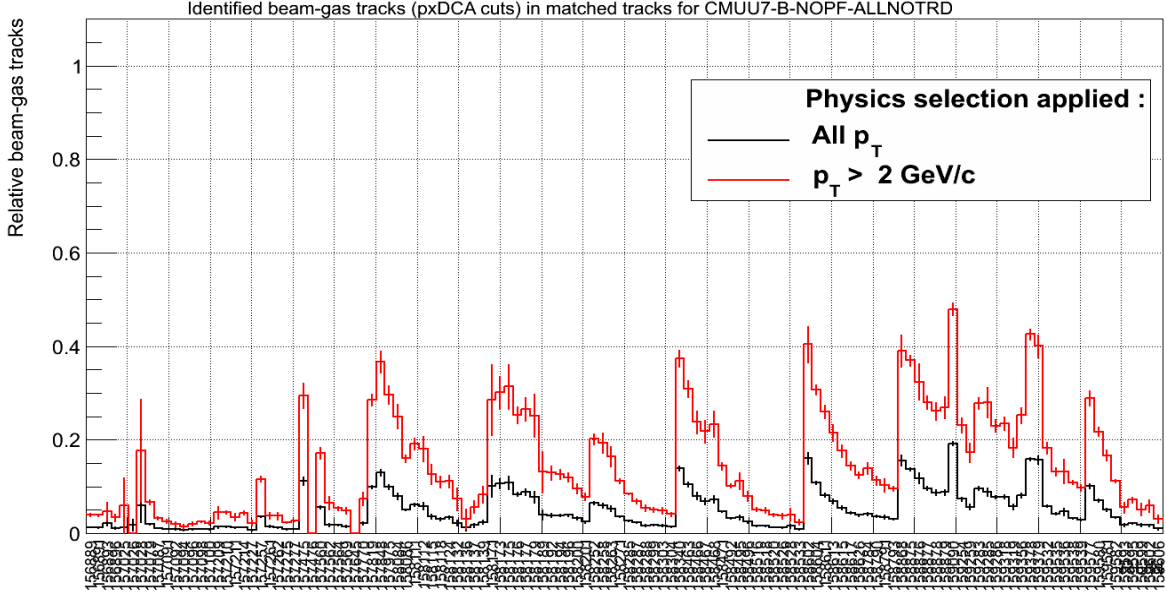


Figure 3.8: Identified beam-gas tracks for CMUU7B events by using pDCA cut.

of the beam is very high. For some runs (158602, 158868, 159090, 159378 and 159379) the beam-gas tracks are more than 40%, which are potentially bad runs. However these runs are not rejected as the source of these beam-gas tracks are understood and these runs can be used with the pDCA cut in the physics analysis.

3.4.4 Tracking and Trigger Chambers Efficiencies

The Muon Tracking system consists of five stations each with two chambers. For a track the average number of clusters in each chamber over a given run is shown in Fig. 3.9. The efficiency of chamber-1 and chamber-3 was quite low. However when a track is reconstructed, hit on both the chambers of a particular station was considered. This gave the overall efficiencies of each tracking stations to be above 80%.

There are two trigger stations in Muon spectrometer, each consisting of two cham-

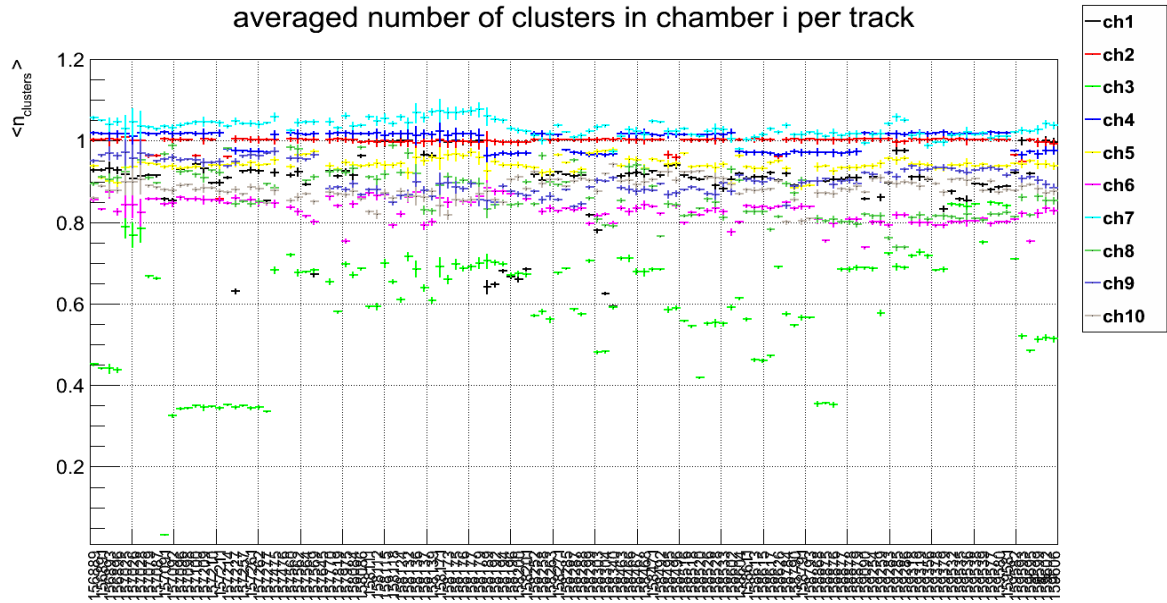


Figure 3.9: The average number of clusters per chamber per track for the Muon tracking system.

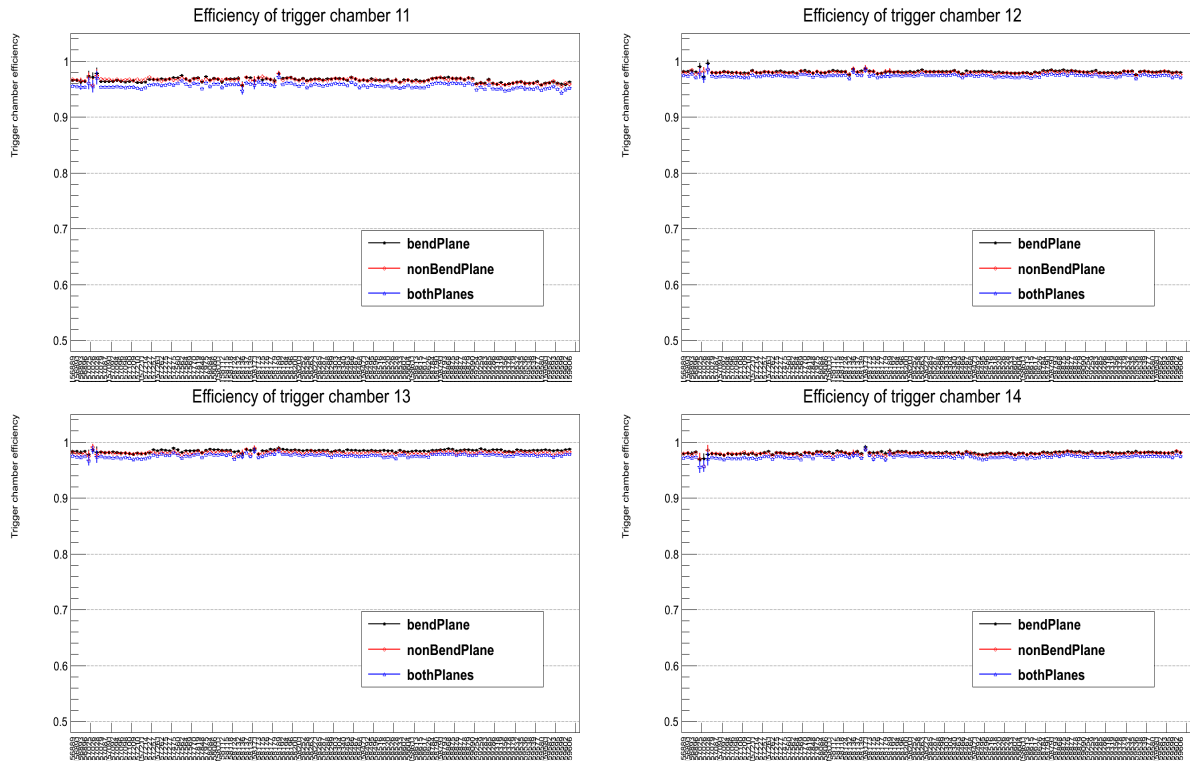


Figure 3.10: Efficiency of bending and non-bending planes of the Trigger chambers.

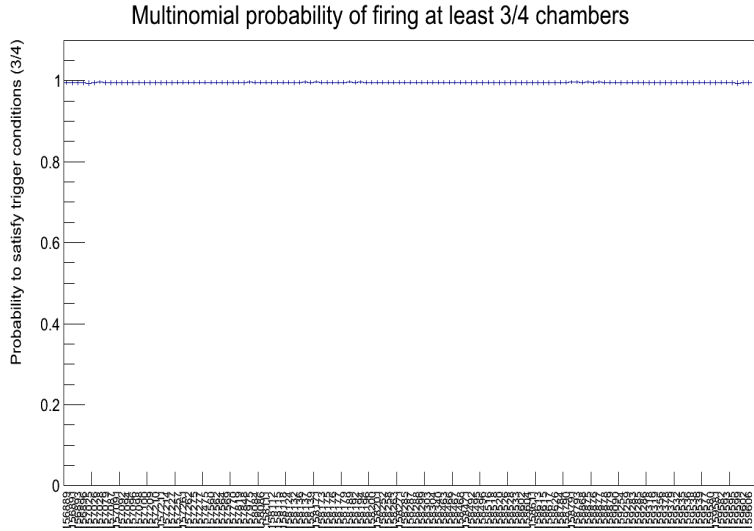


Figure 3.11: Multinomial probability for the Muon trigger system.

bers. Each individual chamber has a bending plane and a non-bending plane. The efficiencies of each chambers is shown in Fig. 3.10. For chamber-11 the efficiencies of both the bending and non-bending plane was above 94%, while for chamber-12, chamber-13 and chamber-14 the efficiency was greater than 96%. However, the trigger condition was taken valid if three out of the four chambers were found to register hits. This multinomial probability is above 98% (see Fig. 3.11) for the Muon trigger system.

3.5 Muon QA for Pb–Pb Collisions

The period LHC11h contains the 2011 Pb–Pb data. The basic procedure of QA for the Pb–Pb is the same as that of the pp data. The difference is in the trigger definitions and one additional parameter called centrality, which was not present in case of pp collisions. There was two set of reconstructions pass1 and pass2 (new OADB), with two more runs (168356 and 170315) in pass2 compared to pass1. A total of 139 runs (~ 21.07 M CMUL, which contains atleast an opposite-

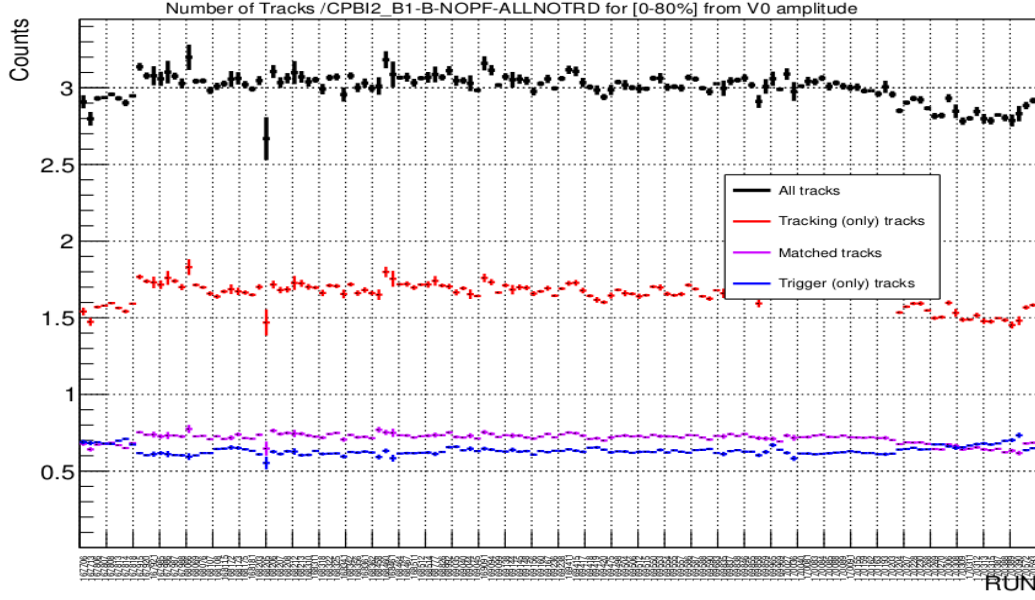


Figure 3.12: Run-by-run analysis of trigger only tracks, tracker only tracks and matched tracks per Minimum Bias (CPBI2_B1) events.

sign muon pair in the triggering system in coincidence with the minimum bias condition) was selected from the ALICE logbook after applying the basic selection criteria. The total runs reconstructed was 136, out of which 2 runs (169683 and 170162) neither contains the muon trigger nor the centrality, but contains the minimum bias trigger [6].

3.5.1 Minimum Bias Events

In Pb–Pb the trigger CPBI1_B1 and CPBI2_B1 represents the minimum bias events. The number of tracks per CPBI2_B1 trigger is shown in Fig. 3.12 on run-by-run basis for the LHC11h period. Except at the beginning and at the end the matched tracks per CPBI2_B1 is ~ 0.7 , which is around a order of magnitude higher than the pp values of ~ 0.008 in LHC11d period.

In Pb–Pb data reconstruction there was an additional parameter of centrality, which is calculated through the study of the V0 signal amplitude distribution. The

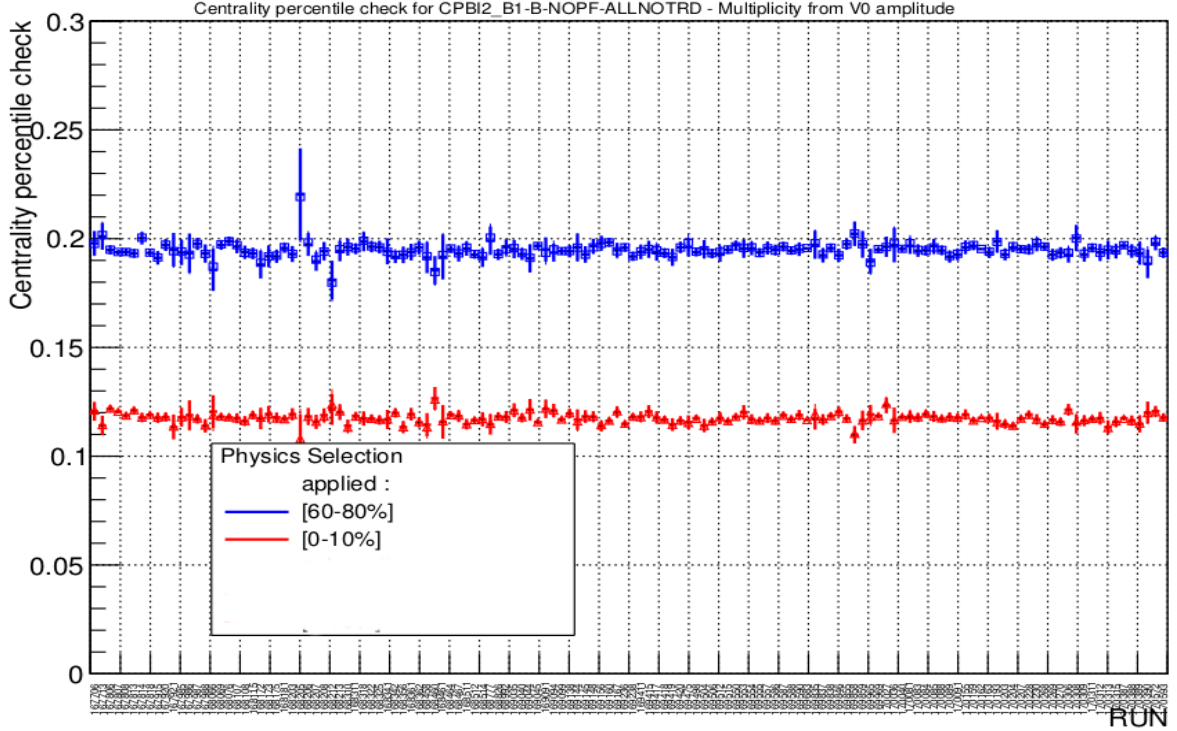


Figure 3.13: Centrality percentile of the central and peripheral Minimum Bias events.

centrality percentile for the minimum bias events was analyzed for the most central (0%–10%) and peripheral (60%–80%) events after physics selection (Fig. 3.13). This shows a flat distribution for both the centrality bins over the whole period of data collection.

3.5.2 High p_T Events

The CPBI1MSH trigger in the 2011 Pb–Pb run corresponded to the high p_T unlike sign dimuon events with at least one muon having the p_T of 4.2 GeV/c. The matched tracks per CPBI1MSH was analyzed for $p_T = 1$ and 2 GeV after applying the physics selection, vertex and R_{Abs} cuts for the 0%–80% centrality range (see Fig. 3.14). Although there is some fluctuation for 1 GeV p_T cut, for 2 GeV p_T cut it

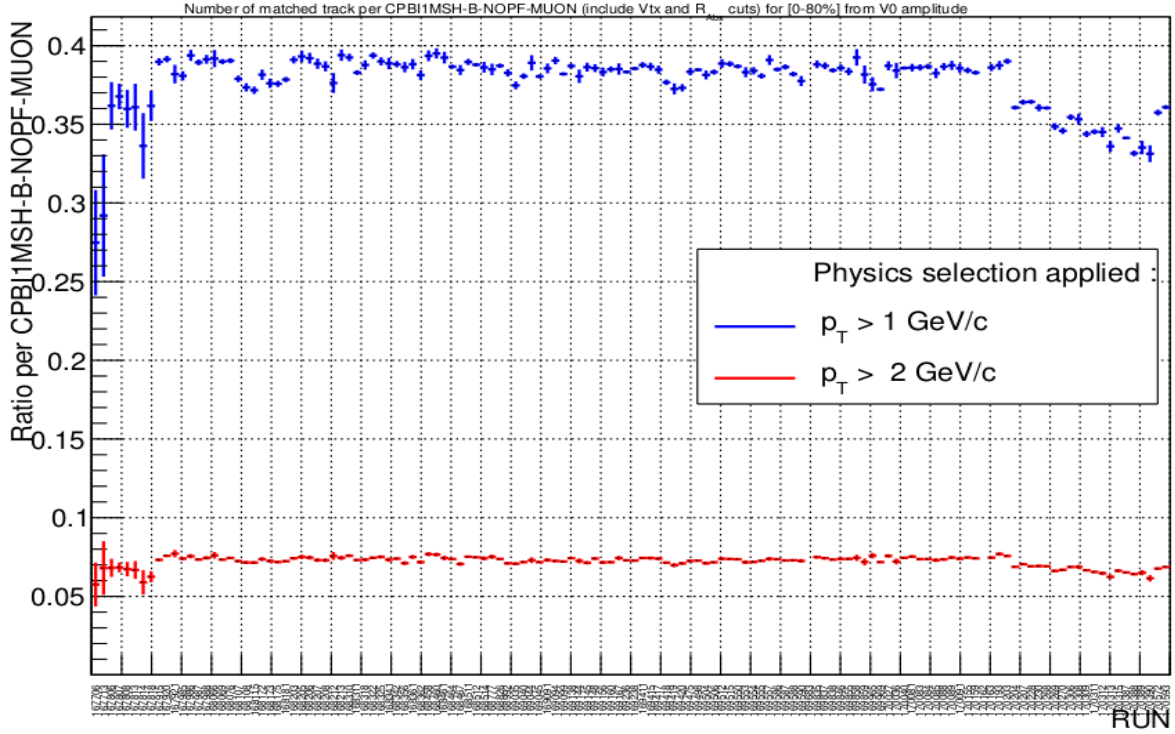


Figure 3.14: Number of matched tracks per CPBI1MSH after applying the $p_T = 1$ and 2 GeV cut.

is almost flat.

The charge of the match tracks was also analyzed for the Muon high p_T events. It was found that after few runs the asymmetry in charge (Q_{asy}) decreases with time (see Fig. 3.15). However after run 169590 the asymmetry again starts to increase. This increase is due to the change in polarity of the magnetic filed. From run 166529 to 169591 the magnetic filed configuration was $(-, -)$, while from run 169628 to 170593 it was $(+, +)$. However it can be concluded that during the Pb-Pb run, the bottom side of the tracker system was more efficient than that of the top.

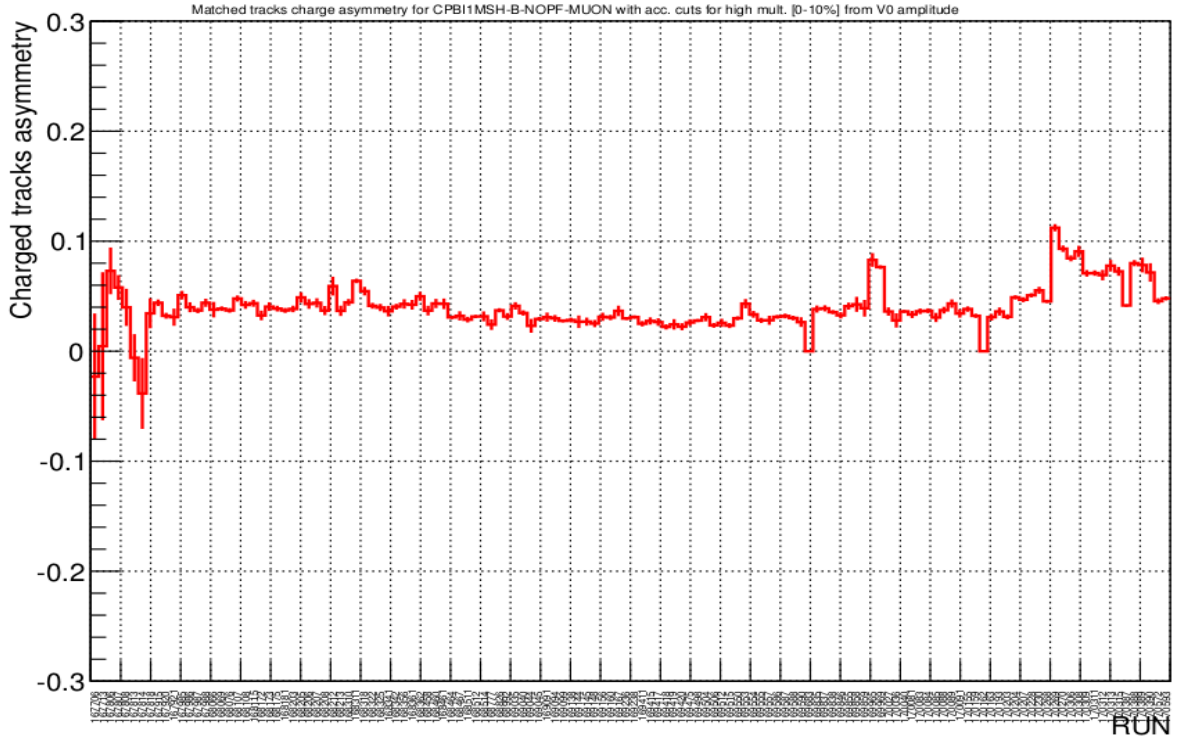


Figure 3.15: Charge asymmetry of the matched tracks for the CPBI1MSH trigger.

3.5.3 Tracking and Trigger Chambers Efficiencies

The overall Muon tracking chamber efficiency is good. There was $\sim 15\%$ loss in efficiency for run 169420 on chamber-1 and $\sim 10\%$ loss on chamber-3 for runs 168203–170593 (see Fig. 3.16). The mean number of clusters per track on chamber-3 was < 0.6 . However when a track is reconstructed, hit on both the chambers of a particular station is considered. This gave the overall efficiencies of each tracking stations above 80%.

The efficiencies of each chambers for the Muon trigger stations is shown in Fig. 3.17. For each chamber the efficiencies of both the bending and non-bending plane is above 95% and the multiniminal probability was above 99% (see Fig. 3.18) for the Muon trigger system.

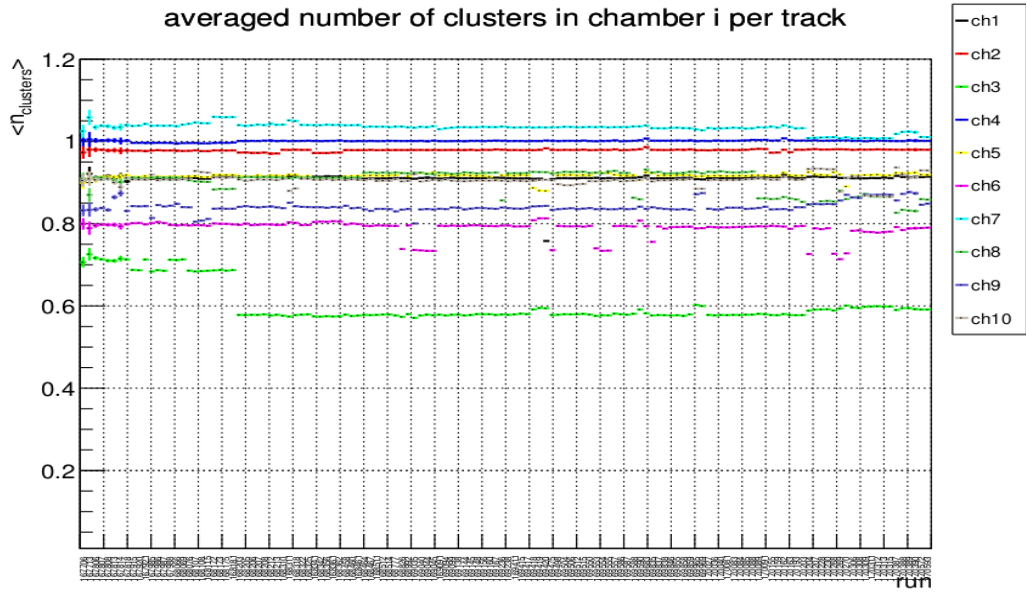


Figure 3.16: The average number of clusters per chamber per track in Pb–Pb for the Muon tracking system.

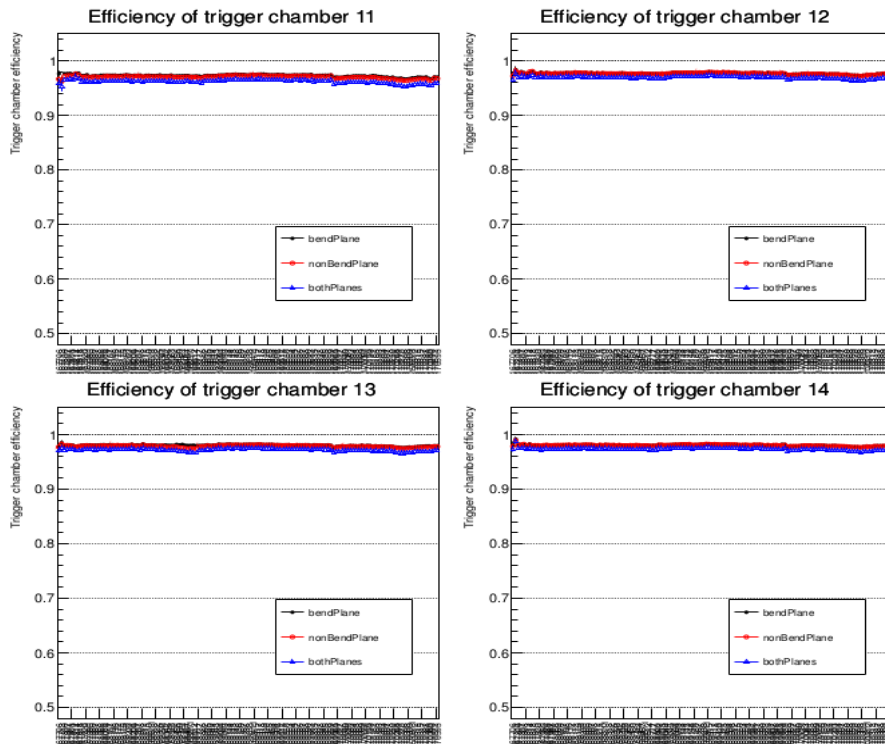


Figure 3.17: Efficiency of bending and non-bending planes in Pb–Pb of the Trigger chambers.

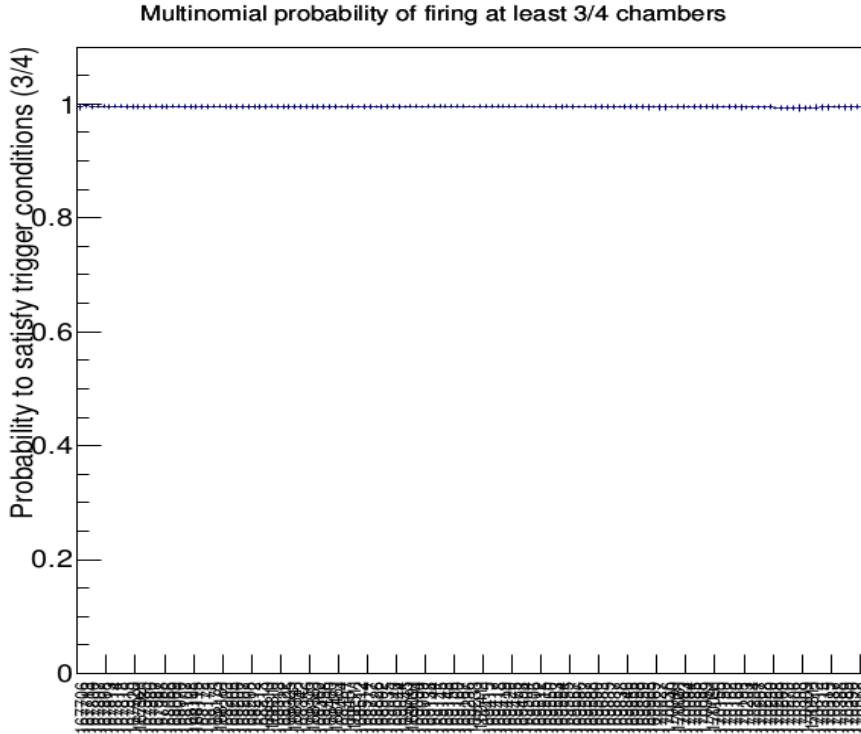


Figure 3.18: Multinomial probability for the Muon trigger system in Pb–Pb.

3.6 Summary

For the pp collisions in LHC11d period, a total of 141 runs (~ 2.47 M CMUU7B) were selected from the ALICE Logbook. Out of these 141 runs 5 runs were not reconstructed due to various issues in the GRP/CTP/Config OCDB. Due to inconsistent behaviour and very low unlike sign events (< 1 k CMUU7B) 10 runs (~ 2.69 k CMUU7B) were rejected. There was large physics selection effect in 2 runs, which are rejected. Some runs had a large beam-gas effect which is understood and identified. These runs were not rejected, as the beam-gas tracks could be rejected for these runs by using the pDCA cut. Finally 127 runs (~ 2.27 M CMUU7B) were tagged as good for the physics analysis.

In case of Pb–Pb collisions in LHC11h period, a total of 139 runs were selected from the ALICE logbook. Out of these 139 runs, 136 runs were reconstructed. Two

runs 169683 and 170162 neither had the muon triggers nor the centrality triggers, but contained only the minimum bias triggers. The Muon tracking chamber efficiency was good ($> 80\%$) and the variation in efficiency was $< 10\%$. The trigger chamber efficiency was stable during the period and the efficiency was above 95%. Finally 136 runs passed the quality assurance, but two of them did not contain opposite sign dimuon events.

Bibliography

- [1] https://alice-logbook.cern.ch/logbook/date_online.php?p_cont=lc&p_cp_n=1&p_cvm=Compact&pcf_ctc=%2C%2C20
- [2] https://alice-logbook.cern.ch/logbook/date_online.php?p_cont=rund&p_run=1247458&p_tab=le
- [3] <http://alimonitor.cern.ch/configuration/>
- [4] <https://twiki.cern.ch/twiki/bin/view/ALICE/QAForTheSelectionOfGoodPhysicsRunsForMuonPhysics>
- [5] <https://twiki.cern.ch/twiki/bin/view/ALICE/MuonppQA2011>
- [6] <https://twiki.cern.ch/twiki/bin/view/ALICE/MuonPbPbQA2011>

Chapter 4

Upsilon(Υ) Production in Pb-Pb Collisions

In this chapter the detail analysis of Υ production in Pb-Pb collisions has been discussed. The data were collected by ALICE Muon Spectrometer ($2.5 < \eta < 4$) at $\sqrt{s_{NN}} = 2.76$ TeV with specific trigger conditions. The data sample corresponds to an integrated luminosity $L_{int} = 68.8 \pm 0.9$ (stat.) ± 2.5 (syst. F_{norm}) $^{+5.5}_{-4.5}$ (syst. σ_{Pb-Pb}) μb^{-1} .

4.1 Data Selection

4.1.1 Trigger Selection

The data selection was done in accordance to the trigger condition. The minimum bias (MB) trigger was defined as the coincidence of a signal in both the V0-A and the V0-C detectors synchronized with the passage of two colliding lead bunches. This MB trigger provided high trigger efficiency ($> 95\%$) for hadronic interactions. An additional threshold on the energy deposited in the ZDCs was

used to reject the contribution from electromagnetic processes. The MB trigger was considerably down-scaled to open the DAQ bandwidth for more rare triggers. In particular, the unlike sign dimuon low- p_T trigger (p_T threshold ~ 1 GeV/c), also called MUL, was used in this analysis. The p_T threshold was defined as the value where the trigger efficiency for single muons was found to be 50%. The MUL trigger was defined as the coincidence of the MB trigger requirements with the detection of two opposite-sign muons with a transverse momentum above the 1 GeV/c threshold. Beam-induced background was further reduced at the offline level by timing cuts on the signals from the V0 and from the ZDC.

4.1.2 Track Selection

The high combinatorial background in Pb-Pb collisions reduces the signal significance. In order to improve the signal-over-background ratio the following selection criteria on single muon tracks were imposed:

- (i) the tracks with pseudo-rapidity in the acceptance of the spectrometer ($2.5 < \eta < 4$) were selected;
- (ii) each track reconstructed in the tracking chambers should match a track segment in the trigger chambers (low- p_T threshold ~ 1 GeV/c). This selection helped to reject the background due to light hadrons which were absorbed by the Iron wall of the Muon Spectrometer;
- (iii) tracks crossing the part of the Front Absorber with the highest density material (steel, tungsten etc.) were rejected by a cut on their transverse radius coordinate at the end of the absorber ($17.6 < R_{ABS} < 89.5$ cm). This cut limited the impact of multiple scattering and energy loss effects which degrade the invariant mass resolution;
- (iv) tracks have to point to the interaction vertex. This selection significantly

reduced the amount of fake and beam-induced tracks contaminating the muon sample;

(v) the transverse momentum of the tracks was required to be larger than 2 GeV/c. It was verified that this selection did not reduce signal counts but reduced the background by about 20% in the $\Upsilon(1S)$ invariant mass range. This feature can be understood by considering that muons from $\Upsilon(1S)$ decay have generally large p_T because of the large mass of the meson, while the muons originating due to the decay of pions and kaons are of low p_T .

4.1.3 Centrality Selection

A cut on each event was also applied according to their degree of centrality by means of the V0 detector amplitude which was fitted using a Glauber model [2, 3]. The centrality classes were defined as intervals in percentages of the hadronic Pb-Pb cross-section. With the Glauber model, it was also possible to estimate the variables related to the collision geometry such as the average number of participant nucleons, $\langle N_{part} \rangle$, the average number of binary collisions, $\langle N_{coll} \rangle$, and the nuclear overlap function, $\langle T_{AA} \rangle$, per centrality class. The $\langle T_{AA} \rangle$ factor is equal to the average number of binary collisions divided by the nucleon-nucleon cross-section and can be interpreted as the nucleon-nucleon equivalent integrated luminosity per heavy-ion collision at a given event centrality [4].

In order to ensure a fully efficient MB trigger, events corresponding to the centrality interval 0% – 90% were selected. The choice of such an event selection was driven by Monte Carlo (MC) simulations which showed that, in this particular centrality range, more than 99% of the events were expected to satisfy the MB trigger conditions leading to a positive MB trigger decision. The efficiency loss in more peripheral collisions was related to the low particle multiplicity. In addition, in the

0% – 90% centrality class the contribution of the electromagnetic background was found to be negligible [2].

In this analysis, the data sample was divided in two classes: 0% – 20% (central collisions) and 20% – 90% (semi-peripheral collisions). The corresponding numerical values for $\langle N_{coll} \rangle$, $\langle N_{part} \rangle$ and $\langle T_{AA} \rangle$ are given in Table 4.1.

Centrality	$\langle N_{coll} \rangle$	$\langle N_{part} \rangle$	$\langle T_{AA} \rangle (\text{mb}^{-1})$
0%–90%	401 ± 41	124 ± 2	6.3 ± 0.2
0%–20%	1211 ± 130	308 ± 4	18.9 ± 0.6
20%–90%	170 ± 16	72 ± 2	2.7 ± 0.1

Table 4.1: Average number of binary collisions, average number of participant nucleons and nuclear overlap function for the various centrality classes considered in this analysis [5].

4.2 Minimum Bias Normalization

A data sample of 17.3×10^6 Pb-Pb collisions triggered with the MUL condition was collected satisfying all the above conditions. Taking advantage of the small part of the DAQ bandwidth kept open for MB triggers, it was possible to obtain the number of MB events corresponding to the available number of MUL events. The procedure was based on a normalization factor estimated run-by-run and corresponding to the inverse of the probability of having the MUL condition verified in an MB event. The scaling factor for this normalization was called F_{norm} and is defined as the number of MB events (N_{MB}) in the statistics divided by the number of events fulfilling MB and unlike sign dimuon low- p_T trigger conditions together ($N_{MUL \in MB}$):

$$F_{norm} = \frac{N_{MB}}{N_{MUL \in MB}} \quad (4.1)$$

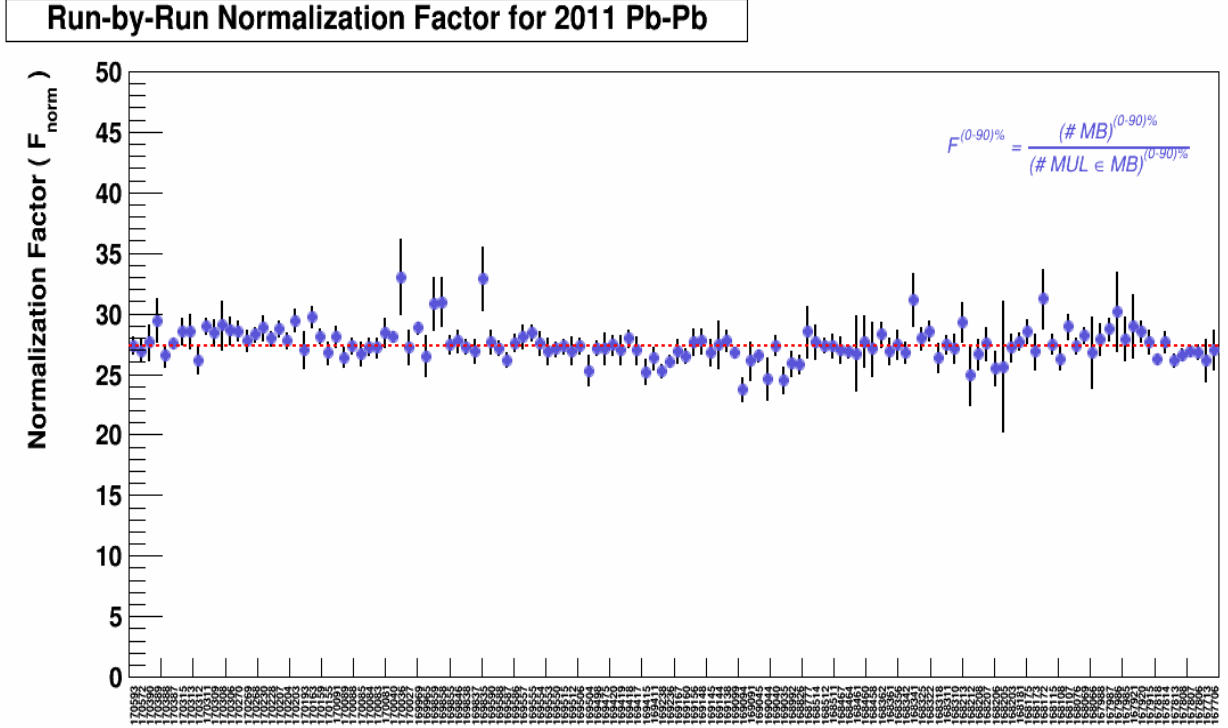


Figure 4.1: The F_{norm} as a function of run number. The dotted line represents the average value, while RMS gives the systematics.

A run-by-run study was carried out in order to calculate the F_{norm} as shown in the Fig. 4.1. The dotted line represents the average value of F_{norm} and the systematic was the RMS value of these 134 runs, resulting ($F_{norm} = 27.50 \pm 0.01(\text{stat.}) \pm 0.99(\text{syst.})$). Since the number of MB events did not depend on the centrality of the Pb-Pb collision (if expressed in percentage of the nuclear cross section), the number of MB events in a selected centrality interval was assumed to scale with the width of the range. Assuming a nuclear Pb-Pb cross-section $\sigma_{PbPb} = 7.7 \pm 0.1(\text{stat.})^{+0.6}_{-0.5} (\text{syst.})\text{b}$ [1], the data sample corresponded to an integrated luminosity $L_{int} = 68.8 \pm 0.9 (\text{stat.}) \pm 2.5 (\text{syst. } F_{norm})^{+5.5}_{-4.5} (\text{syst. } \sigma_{Pb-Pb}) \mu\text{b}^{-1}$.

4.3 Signal Extraction

4.3.1 Fit Procedure

The $\Upsilon(1S)$ candidates were formed by combining pairs of opposite-sign tracks with a rapidity in $2.5 < y < 4$ and with each track fulfilling the requirements described in 4.1.2. The signal extraction was performed by fitting the observed opposite-sign dimuon invariant mass distributions. The sum of the following five functions was considered as the default option (other choices are described later in this section):

(i) the line shape of the Υ was described by three Extended Crystal Ball (CB2) functions. The CB2 function consists of a Gaussian core with a power-law tail on both sides. It was found to reproduce the shape of $\Upsilon(1S)$ resonance from realistic MC simulations. The low invariant mass tail was due to the muon energy loss fluctuation in the front absorber, while the high invariant mass one was due to alignment and calibration biases. The formula for the CB2 can be found in Appendix;

(ii) the underlying continuum was described by a sum of two exponential functions (Double Exponential, or DE in the following). The simulations showed that the main contribution to the dimuon continuum at high invariant mass comes from the semimuonic decays of D and B hadrons [6]. The DE allowed us to satisfactorily reproduce the mass shape of such a background.

In this analysis, the amplitude, the position and the width of the $\Upsilon(1S)$ were left free, while the position and width of $\Upsilon(2S)$ and $\Upsilon(3S)$ were fixed according to

the following formulas:

$$M_{\Upsilon(2S)} = M_{\Upsilon(2S)}^{PDG} + (M_{\Upsilon(1S)}^{Fit} - M_{\Upsilon(1S)}^{PDG}) \times \frac{M_{\Upsilon(2S)}^{PDG}}{M_{\Upsilon(1S)}^{PDG}} \quad (4.2)$$

$$M_{\Upsilon(3S)} = M_{\Upsilon(3S)}^{PDG} + (M_{\Upsilon(1S)}^{Fit} - M_{\Upsilon(1S)}^{PDG}) \times \frac{M_{\Upsilon(3S)}^{PDG}}{M_{\Upsilon(1S)}^{PDG}} \quad (4.3)$$

$$\sigma_{\Upsilon(2S)} = \sigma_{\Upsilon(1S)}^{Fit} \times \frac{M_{\Upsilon(2S)}^{PDG}}{M_{\Upsilon(1S)}^{PDG}} \quad (4.4)$$

$$\sigma_{\Upsilon(3S)} = \sigma_{\Upsilon(1S)}^{Fit} \times \frac{M_{\Upsilon(3S)}^{PDG}}{M_{\Upsilon(1S)}^{PDG}} \quad (4.5)$$

where $M_{\Upsilon(2S)}^{PDG}$, $M_{\Upsilon(1S)}^{Fit}$, $M_{\Upsilon(2S)}$ are the value of mass of $\Upsilon(2S)$ from PDG, mass of $\Upsilon(1S)$ from the fit and mass of $\Upsilon(2S)$ fixed for the fitting, respectively and $\sigma_{\Upsilon(1S)}^{Fit}$, $\sigma_{\Upsilon(2S)}$ are values of width of $\Upsilon(1S)$ from the fit, with of $\Upsilon(2S)$ fixed for the fitting respectively. The parameters of the DE and the amplitude of the $\Upsilon(2S)$ and the $\Upsilon(3S)$ were also left free. Because of the few entries observed for invariant masses above $\sim 9.8 \text{ GeV}/c^2$, the width and the position of the $\Upsilon(2S)$ and $\Upsilon(3S)$ were constrained. In the nominal procedure, the mass differences between states were fixed from the PDG values [7] and the width for the $\Upsilon(2S)$ and $\Upsilon(3S)$ were forced to scale proportionally with that of the $\Upsilon(1S)$ according to the PDG mass ratio. In addition, since signal distribution tails were poorly constrained by the data, the tail parameters of the CB2 were fixed according to the results from MC simulations.

4.3.2 Fit Results

The above mentioned fitting procedure was applied to the dimuon invariant mass distribution for different centrality and rapidity bins. These fitted mass spectra are shown in Fig. 4.2. The total fit function is represented by the pink line. The red, blue, green lines represent the three CB2 functions used to describe the $\Upsilon(3S)$, $\Upsilon(2S)$, $\Upsilon(1S)$ state distributions and the yellow line represents the DE used to describe the underlying continuum. The numbers of $\Upsilon(1S)$ counts, the position, the width of the $\Upsilon(1S)$ and the χ^2 per degree of freedom (χ^2/ndf) are given in the figures.

The results of the fits are summarized in Table 4.2. The position of the $\Upsilon(1S)$ peak was found to be in good agreement with the PDG meson mass ($9.460 \text{ GeV}/c^2$) [7] within uncertainties. The signal-over-background ratio (S/B) was always larger than unity and the obtained significance ($\frac{S}{\sqrt{S+B}}$) was always larger than 5. It is to be noted that the S/B ratio and the significance were evaluated at 3σ , which implies that, the number of signal and background counts were obtained in an invariant mass range centred on the $\Upsilon(1S)$ peak position and covering ± 3 times its width.

Centrality	Rapidity	Mass (GeV/c^2)	Width (MeV/c^2)	S/B	Significance
0%–90%	$2.5 < y < 4.0$	9.44 ± 0.03	144 ± 27	1.3 ± 0.2	8 ± 1
0%–20%	$2.5 < y < 4.0$	9.44 ± 0.04	136 ± 40	1.0 ± 0.2	5 ± 1
20%–90%	$2.5 < y < 4.0$	9.46 ± 0.04	150 ± 37	1.8 ± 0.4	6 ± 1
0%–90%	$2.5 < y < 3.2$	9.49 ± 0.03	107 ± 25	1.6 ± 0.3	6 ± 1
0%–90%	$3.2 < y < 4.0$	9.34 ± 0.05	159 ± 40	1.1 ± 0.2	5 ± 1

Table 4.2: The fit results for different centrality and rapidity bins.

4.3.3 Systematic Uncertainties

Different variations of the fit method were performed to extract the systematic uncertainties on the signal extraction. Only the fits with a χ^2/ndf smaller than

1.5 were considered and the stabilities of the $\Upsilon(3S)$ peak width and position were verified. The various sources of systematics are discussed below:

4.3.4 Background Description

In addition to the DE function a Double Power Law (DPL) function, defined as the sum of two power law functions, was used to describe the underlying background. For each function, the lower and the upper bounds of the fit range were independently modified within the limits where the background was reasonably fitted. The DPL function led to fits with higher χ^2/ndf than the DE. Nevertheless almost all the fits have a χ^2/ndf below the 1.5 threshold defined previously and thus, the possibility of a DPL shaped background could not be discarded. The systematic uncertainty resulting from this study ranges between 2% and 5% depending on the values of the rapidity or centrality bin.

4.3.5 Mass Position and Signal Width

It was found that for different centrality and rapidity bins the statistical uncertainty on the $\Upsilon(1S)$ position and width from the fit was less than 0.5% and 30% respectively. Taking this uncertainties as an upper limit the positions and the width of the $\Upsilon(2S)$ and the $\Upsilon(3S)$ resonances were independently shifted to different values to find the uncertainty in the $\Upsilon(1S)$ counts. The resulting uncertainty was found to be of the order of 1%.

4.3.6 Signal Tail Parameters

The CB2 tail parameters for Υ states were varied according to the spread of the line shapes obtained with realistic MC simulations. Parameters were first modified

by the same quantity for each state, then the variation was done independently. The overall systematic uncertainty ranges from $\sim 2\%$ to 4% depending on the centrality and rapidity bins. The values from the signal extraction for various bins are reported in Table 4.3.

Centrality	Rapidity	Counts \pm stat. \pm syst.
0%–90%	$2.5 < y < 4.0$	$134 \pm 20(15\%) \pm 7(5\%)$
0%–20%	$2.5 < y < 4.0$	$64 \pm 14(22\%) \pm 4(6\%)$
20%–90%	$2.5 < y < 4.0$	$66 \pm 12(18\%) \pm 4(6\%)$
0%–90%	$2.5 < y < 3.2$	$72 \pm 13(18\%) \pm 4(6\%)$
0%–90%	$3.2 < y < 4.0$	$57 \pm 13(23\%) \pm 6(11\%)$

Table 4.3: The results of signal extraction. Central values and statistical uncertainties are the average of the results obtained for each study. Systematic uncertainties from each source were summed in quadrature. Overall statistical (systematic) uncertainties range between 15% – 23% (5% – 11%).

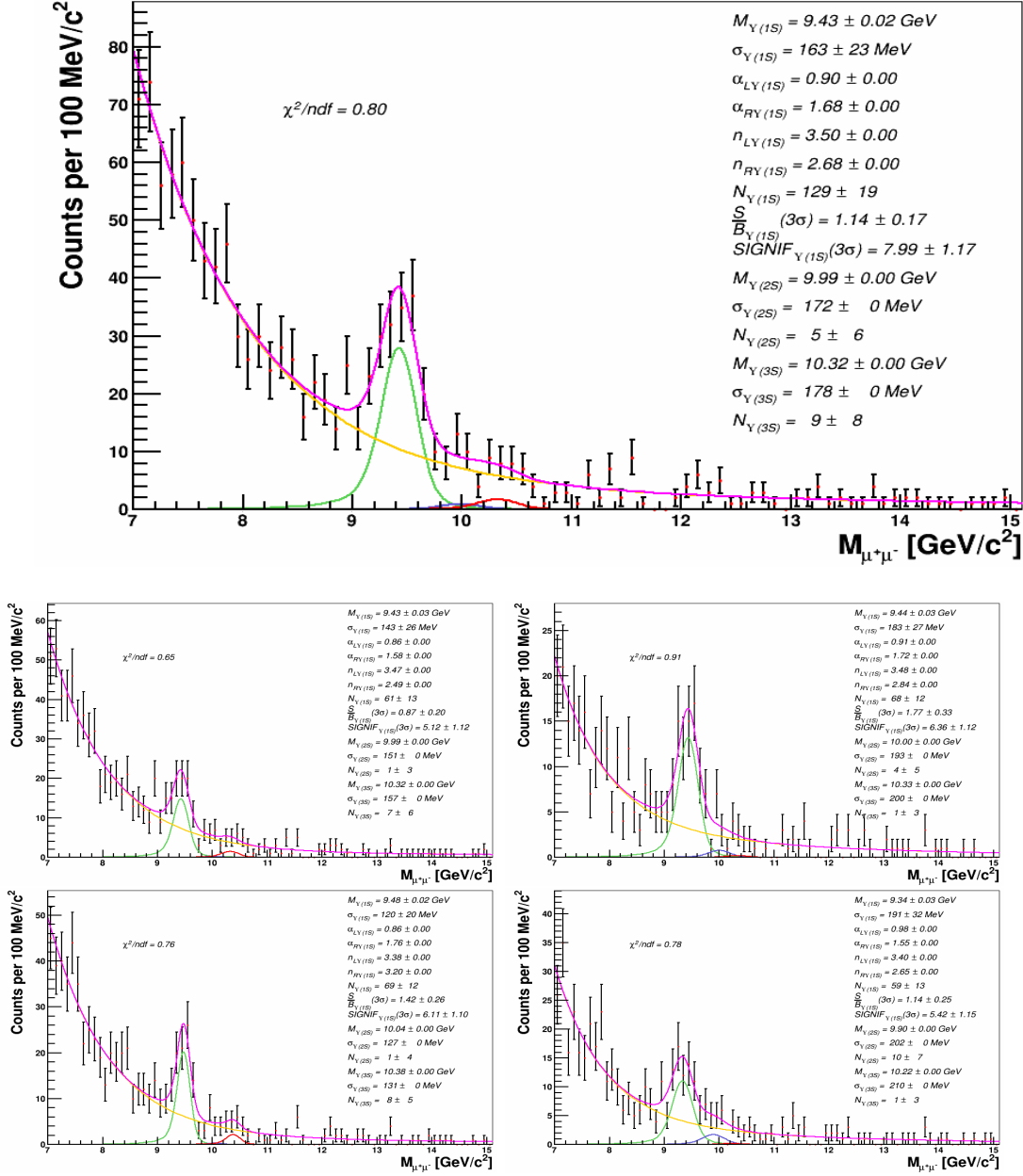


Figure 4.2: Default fit procedure applied to the invariant mass distributions of opposite-sign dimuons in different centrality and rapidity bins. There are five plots top(integrated), middle left(0%–20%), middle right(20%–90%), bottom left(2.5 < y < 3.2) and bottom right(3.2 < y < 4.0).

4.4 $\Upsilon(1S)$ Yield in Pb-Pb Collisions

The yield of $\Upsilon(1S)$ per rapidity unit is expressed as a function of the number of signal counts (section 2.3), $N_{\Upsilon(1S)}$, the number of MB Pb-Pb events, N_{MB} , the acceptance and efficiency correction factor, $A \times \epsilon$, the $\Upsilon(1S) \rightarrow \mu^+ \mu^-$ branching ratio ($BR = 2.48 \pm 0.05\%$) [7], and Δy the rapidity bin width:

$$\frac{dY_{\Upsilon(1S)}}{dy} = \frac{N_{\Upsilon(1S)}}{BR \times N_{MB} \times (A \times \epsilon) \times \Delta y} \quad (4.6)$$

Since the distribution of the number of MB events was found to be flat with centrality as shown in Fig. 4.3, N_{MB} was assumed to scale with the width of the considered centrality bin. The total number of MB events was obtained from the measured number of MUL events, as described in section 4.2.

The yields for each centrality and rapidity range have been reported in Table 4.4. The statistical uncertainties (stat.), the uncorrelated systematic uncertainties (syst.) and the correlated systematic uncertainties (corr.) were obtained by summing in quadrature the contributions from each term of Eq.- 4.6.

Centrality	Rapidity	Yields $\times 10^5$
0%–90%	$2.5 < y < 4.0$	$3.4 \pm 0.5(\text{stat.}) \pm 0.2(\text{uncorr.}) \pm 0.4(\text{corr.})$
0%–20%	$2.5 < y < 4.0$	$7.5 \pm 1.6(\text{stat.}) \pm 0.5(\text{uncorr.}) \pm 0.9(\text{corr.})$
20%–90%	$2.5 < y < 4.0$	$2.1 \pm 0.4(\text{stat.}) \pm 0.1(\text{uncorr.}) \pm 0.2(\text{corr.})$
0%–90%	$2.5 < y < 3.2$	$4.5 \pm 0.8(\text{stat.}) \pm 0.6(\text{uncorr.}) \pm 0.2(\text{corr.})$
0%–90%	$3.2 < y < 4.0$	$2.4 \pm 0.5(\text{stat.}) \pm 0.4(\text{uncorr.}) \pm 0.1(\text{corr.})$

Table 4.4: The yields of $\Upsilon(1S)$ per unit of rapidity obtained in Pb-Pb collisions at $\sqrt{s_{NN}} = 2.76$ TeV for each centrality and rapidity range. Uncorrelated (correlated) systematic uncertainties are quoted as uncorr. (corr.).

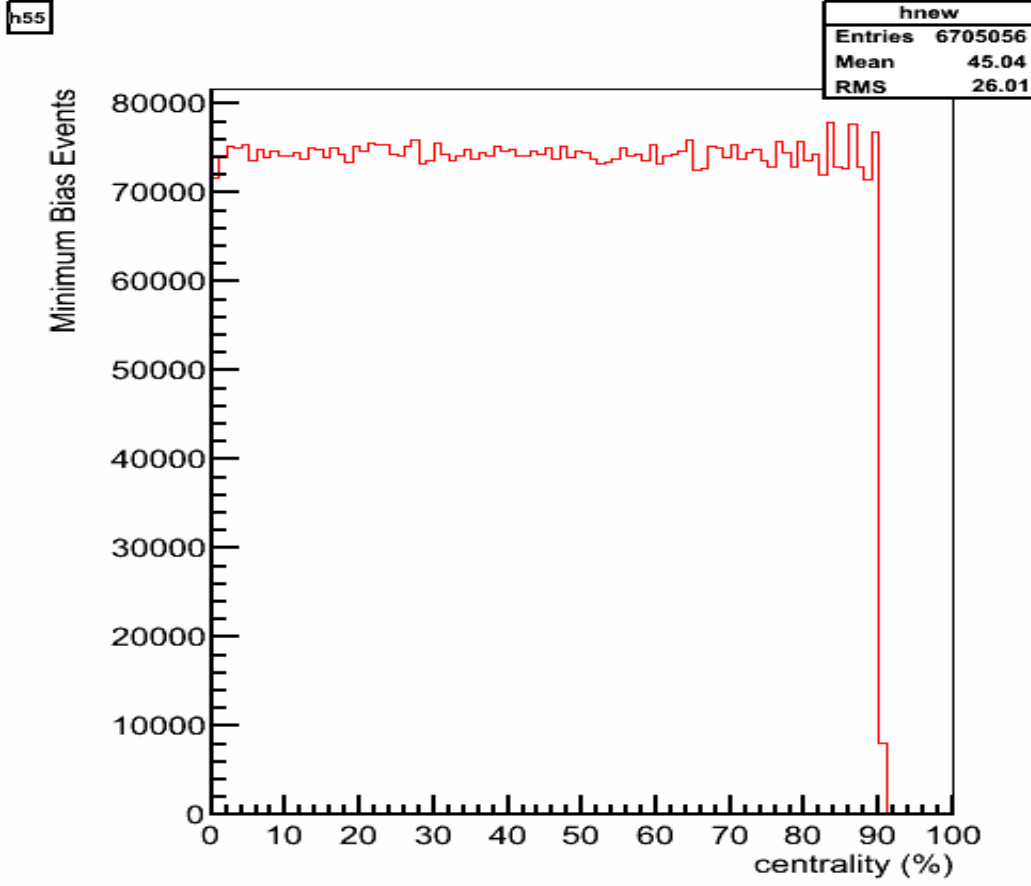


Figure 4.3: Distribution of MB events as a function of centrality in Pb-Pb collisions.

4.5 Monte Carlo Simulation

The product of acceptance and efficiency as well as the line shapes of the CB function, used in the fitting of the Υ signals were extracted from the Monte Carlo (MC) simulations.

4.5.1 Acceptance and Efficiency Correction Factor

The product of acceptance and efficiency ($A \times \epsilon$) is defined as the probability for the decay muons from $\Upsilon(1S)$ produced in the geometrical acceptance of the

Muon Spectrometer to be correctly identified and reconstructed.

$$A \times \varepsilon = \frac{N_{\Upsilon}^{rec}(2.5 \leq y \leq 4.0)}{N_{\Upsilon}^{sim}(2.5 \leq y \leq 4.0)} \quad (4.7)$$

In pure MC simulation the $\Upsilon(1S)$ were generated in the forward rapidity region and then forced to decay into dimuons. The experimental conditions in terms of HV, IV and readout were also considered in the MC simulations. The distributions of generated and the reconstructed $\Upsilon(1S)$ in MC simulation are shown in the Fig. 4.4.

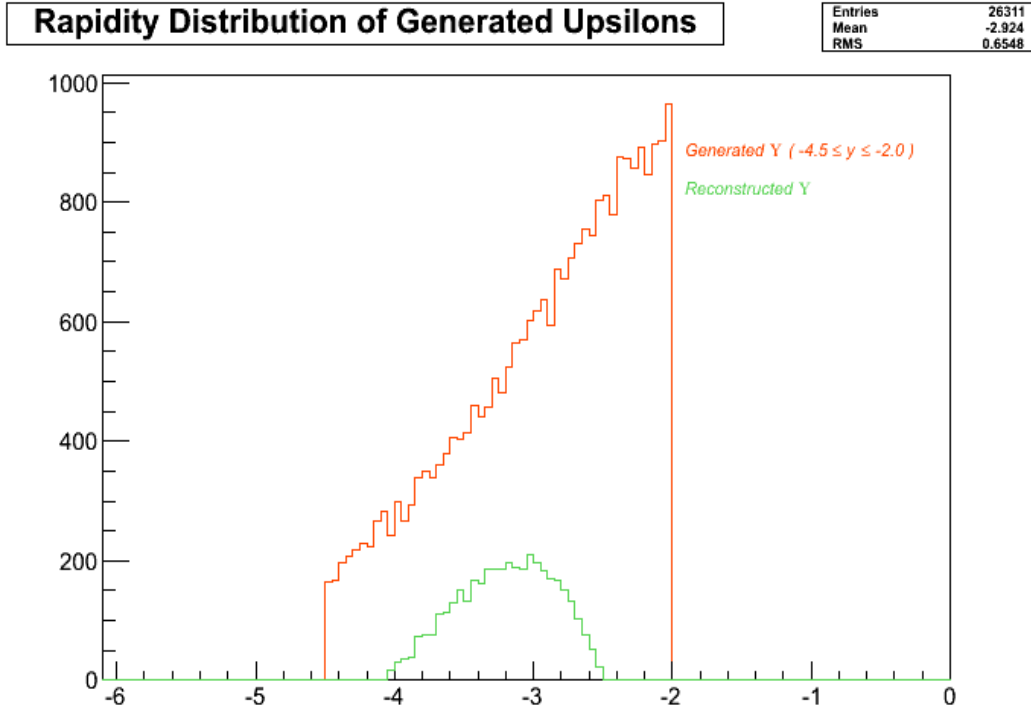


Figure 4.4: The distribution of generated and the reconstructed $\Upsilon(1S)$ in MC simulation.

4.5.2 Embedding Production

The embedding Monte Carlo technique consisted of simulating a signal particle and embedding it with hits generated in the detector for a real MB event. Among MC techniques, the embedding provides the most realistic background conditions. Such a realistic description is necessary in the case of (most central) Pb-Pb collisions because of the high particle multiplicity environment which could alter the track reconstruction efficiency due to overlap of charge clusters in the cathode pad chambers. The $\Upsilon(1S)$ were generated according to realistic parametrization of their p_T and y distributions [8] and were forced to decay into dimuons. The detector response was provided by GEANT3 [4] taking into account the time dependence of the detector efficiency and the residual misalignment of the tracking chambers. The efficiency of the muon trigger system was calculated from data and is based on the analysis of the hit distributions in the four plane of detection chambers. Chamber efficiency maps were made out for each run and used in the simulations. The single-muon tracking efficiencies are evaluated using an algorithm based on reconstructed tracks [10].

The average $A \times \varepsilon$ obtained from the embedding simulations was $21.9 \pm 0.1(\text{stat.})\%$. The results for each rapidity and centrality bin considered further in the analysis are summarized in Table 4.5.

Centrality	Rapidity	$A \times \varepsilon$ (%)
0%–90%	$2.5 < y < 4.0$	$21.9 \pm 0.1(\text{stat.})$
0%–20%	$2.5 < y < 4.0$	$21.6 \pm 0.1(\text{stat.})$
20%–90%	$2.5 < y < 4.0$	$22.6 \pm 0.1(\text{stat.})$
0%–90%	$2.5 < y < 3.2$	$19.3 \pm 0.1(\text{stat.})$
0%–90%	$3.2 < y < 4.0$	$25.7 \pm 0.1(\text{stat.})$

Table 4.5: $A \times \varepsilon$ values for the centrality and rapidity bins considered in the present analysis.

4.5.3 Signal Line Shape

It was observed that the reconstructed $\Upsilon(1S)$ signal from the simulation deviates from the Gaussian shape. This was due to multiple muon scattering in the front absorber and residual mis-alignment. So the signal line shape from the MC simulation could not be fitted with a Gaussian function, rather the fit was good if we take a Double Crystal Ball (CB2) function. The tail parameters for $\Upsilon(1S)$ for various centrality and rapidity bins are given in the Table 4.6. The lower-end tail parameters for the extended crystal ball were denoted by α , n while the upper-end tail parameters were denoted by α' , n' , respectively. It was assumed that the same set of tail parameters also describe the other two resonances of Υ , namely $\Upsilon(1S)$ and $\Upsilon(2S)$, while calculating the systematic uncertainties.

Centrality	Rapidity	α	n	α'	n'
0%–90%	$2.5 < y < 4.0$	0.91 ± 0.01	3.54 ± 0.04	1.69 ± 0.01	2.72 ± 0.04
0%–20%	$2.5 < y < 4.0$	0.87 ± 0.01	3.55 ± 0.08	1.60 ± 0.02	2.56 ± 0.07
20%–90%	$2.5 < y < 4.0$	0.92 ± 0.01	3.52 ± 0.04	1.71 ± 0.01	2.80 ± 0.05
0%–90%	$2.5 < y < 3.2$	0.87 ± 0.01	3.43 ± 0.06	1.74 ± 0.02	3.28 ± 0.08
0%–90%	$3.2 < y < 4.0$	0.99 ± 0.01	3.45 ± 0.05	1.57 ± 0.02	2.70 ± 0.05

Table 4.6: Extended Crystal Ball tail parameters for the centrality and rapidity bins considered in this analysis.

4.5.4 Systematic Uncertainties

4.5.5 Monte Carlo Parametrization

The estimate of $A \times \epsilon$ depends on the $\Upsilon(1S)$ p_T and y shapes used as input distributions in the MC simulations. In order to evaluate the sensitivity of the results on this initial choice, several $A \times \epsilon$ calculations were performed with significantly different p_T and y parametrisations [8] corresponding to different systems, energies and centralities. The input distributions were chosen different enough to

include the a priori unknown nuclear matter effects. The maximum spread observed among the obtained $A \times \varepsilon$ values varied between 4% and 7% (in relative) depending on the considered rapidity bin. These values were used as systematic uncertainties.

4.5.6 Muon Tracking Efficiency

The systematic uncertainty on the efficiency of track reconstruction was estimated by comparing the results from simulations with those obtained from data. In both the cases, the efficiency was evaluated with an algorithm [10] based on the analysis of hit distributions in the tracking chambers. The systematic uncertainty was determined at the single muon level and was properly combined according to the kinematic distributions of decay muons from $\Upsilon(1S)$ to obtain the uncertainty at the dimuon level. This contribution was 8% for the two centrality bins under study, while it is 7% (9%) for the $2.5 < y < 3.2$ ($3.2 < y < 4$) bin. Another uncertainty arose from restricted blind areas on the various chambers, covering the same geometric acceptance. Their presence affected the algorithm used to determine the tracking efficiency and gave rise to additional 2% systematic uncertainty. This uncertainty is not fully uncorrelated with the previous one and has to be added bin by bin.

4.5.7 Muon Trigger Efficiency

A systematic uncertainty on trigger efficiency of 2% came from the comparison of MC results obtained with different chamber efficiency maps. The maps were obtained from data for various detector occupancies and particle transverse momenta.

4.5.8 Matching Efficiency

In addition, it was necessary to consider a 1% systematic uncertainty on the matching of the trigger and tracking information. In order to estimate this value, the matching efficiency obtained from data with different cuts on the χ^2 of the matching was compared with simulation results obtained in the same conditions.

4.6 Nuclear Modification Factor

The suppression of quarkonia can be quantified by measuring the Nuclear Modification Factor R_{AA} , which is obtained by dividing the yield in AA collisions per unit of rapidity by $\langle T_{AA} \rangle$, the average nuclear overlap function and by $\frac{d\sigma^{pp}}{dy}$, the pp reference y-differential cross-section

$$R_{AA} = \frac{\frac{dY_{\Upsilon(1S)}}{dy}}{\langle T_{AA} \rangle \times \frac{d\sigma^{pp}}{dy}} \quad (4.8)$$

4.7 Baseline: pp Reference Cross Section

In order to measure the R_{AA} of Υ at 2.76 TeV, we need the measurements of Υ production both in pp and Pb-Pb collisions at 2.76 TeV. However, due to lack of statistics ALICE cannot measure the Υ cross-section in pp collisions at 2.76 TeV. Fortunately, few $\Upsilon(1S)$ cross-section measurements in pp collisions at different TeV energies exist and most of them refer to central rapidities [11, 12, 13, 14]. Based on this data, the mid-rapidity differential cross-section of $\Upsilon(1S)$ in pp collisions at $\sqrt{s} = 2.76$ TeV ($\frac{d\sigma}{dy}|_{y=0}$) was estimated by means of an interpolation procedure. The mid-rapidity cross-section was then extrapolated to forward rapidities. For that purpose, y-differential distributions were predicted with differ-

ent Pythia6.4 [15] tunes which were first selected according to their ability to reproduce the available forward and mid-rapidity data at $\sqrt{s} = 7$ TeV [14, 16].

4.7.1 Interpolation of $\Upsilon(1S)$ Cross Section at Mid-rapidity

The measurements used for the interpolation of the Υ cross-section at mid-rapidity are summarised in Table 4.7. Different functions were considered to describe the energy dependence of the cross-section and to determine $\frac{d\sigma}{dy}|_{y=0}$ at $\sqrt{s} = 2.76$ TeV. The statistical, systematic and luminosity uncertainties of each measurement were summed in quadrature in order to be used in the fit. As shown in Fig. 4.5, the energy dependence of the cross-section was well described by a power-law or a logarithmic function. Other functional forms were also tested, such as the sum of a logarithmic and a power-law function, or a three-parameter exponential function. The description of the data provided by such forms was less satisfactory and therefore they have been discarded. However, we have checked that the obtained interpolation results are compatible within uncertainties with those obtained with the power-law and logarithmic function.

Experiment	\sqrt{s} (TeV)	$BR_{\mu\mu} \times \frac{d\sigma}{dy} _{y=0}$ [pb]	Rapidity Range
CDF [11]	1.8	680 ± 15 (stat.) ± 56 (syst.)	$ y < 0.4$
D0 [12]	1.96	628 ± 16 (stat.) ± 63 (syst.) ± 38 (lumi.)	$ y < 0.6$
CMS [13]	2.76	921 ± 128 (stat.) ± 157 (syst.) ± 55 (lumi.)	$ y < 1.2$
CMS [14]	7	2025^{+284}_{-263} (stat. + syst. + lumi.)	$ y < 0.4$

Table 4.7: Experimental results used for the interpolation of the $\Upsilon(1S)$ cross-section at mid-rapidity.

Besides the purely empirical fit, a second option was considered for the interpolation. Models such as the Color Evaporation Model [8] predict that the quarkonium cross-section is proportional to the bare quark pair production cross-section.

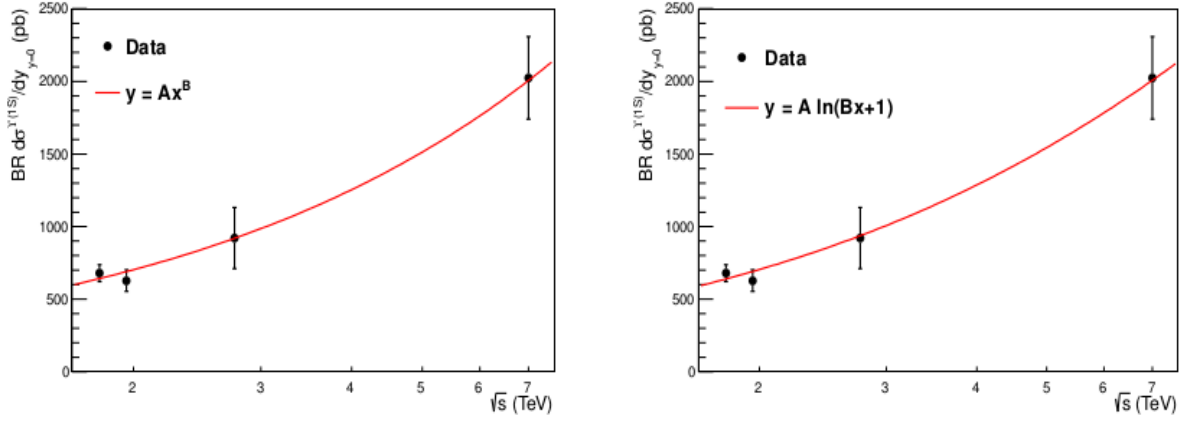


Figure 4.5: Energy dependence of the Υ cross-section at mid-rapidity, with overlaid power-law (left) and logarithmic (right) fit.

In such an approach, one can consider:

$$\frac{d\sigma^{\Upsilon}}{dy}(y, \sqrt{s}) = \alpha \frac{d\sigma^{b\bar{b}}}{dy}(y, \sqrt{s}) \quad (4.9)$$

where $\frac{d\sigma^{b\bar{b}}}{dy}$ is the $b\bar{b}$ cross-section calculated in perturbative QCD.

The available FONLL [9] predictions for the beauty cross-section were used for the interpolation. They provided a central value and an uncertainty band obtained by varying the calculation parameters such as the quark mass or the factorisation scale. Three energy dependence curves were defined, corresponding to the central value and the lower and upper edges of the uncertainty band. For each of the three curves, the α parameter was determined by fitting the ratio of data to FONLL to a constant value. Fig. 4.6 shows the three FONLL predictions scaled by the α constant together with the measured cross-sections. It is found that the model provides a good description of the data and thus can be used for the interpolation. The point at $\sqrt{s} = 2.76$ TeV provides the interpolated value.

The interpolation results at $\sqrt{s} = 2.76$ TeV obtained from the fit with the

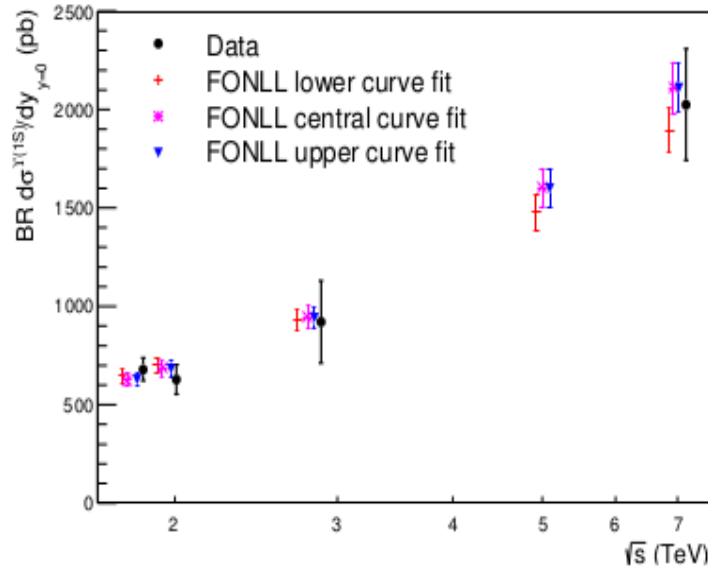


Figure 4.6: Energy dependence of the $\Upsilon(1S)$ cross-section at mid-rapidity, with overlaid FONLL predictions re-scaled by the α parameter. The points corresponding to different predictions at the same energy are slightly shifted horizontally, for visibility.

power-law and logarithmic functional forms and with the three FONLL curves were averaged. It was chosen to combine the largest fit uncertainty (6.2%) with the shape uncertainty defined as the difference between the average and the maximum and minimum of the obtained values (-1.1%+1.6%).

The interpolation at 2.76 TeV was strongly driven by the CDF and D0 measurements at 1.8 and 1.96 TeV. Although the two results were compatible within uncertainties, the data point at higher energy being below the data point at lower energy. In order to check the stability of the result, the procedure was repeated by alternatively excluding the CDF and D0 data point from the fit. A -4%(+6%) difference between the averaged value was obtained with all data and that obtained by excluding the CDF (D0) data point was observed and added to the systematic uncertainties.

The total uncertainty was obtained by summing in quadrature the three above-mentioned uncertainties¹ yielding a final result of $\frac{d\sigma^\Upsilon}{dy}|_{y=0}$ ($\sqrt{s} = 2.76$ TeV) = (935 ± 82) pb.

4.7.2 Extrapolation of $\Upsilon(1S)$ Cross Section at Forward-rapidity

The CMS Collaboration showed that Pythia6.4 [15] was able to reproduce the rapidity and the transverse momentum differential distributions of Υ in pp collisions at $\sqrt{s} = 7$ TeV [14]. Taking advantage of this fact, the strategy to obtain the reference in the Muon Spectrometer rapidity range can be sketched as follows:

- (i) test the Υ productions from Pythia6.4 with different tunes against 7 TeV data from LHC experiments;
- (ii) use the tunes in agreement with 7 TeV data to generate Υ events in pp collisions at $\sqrt{s} = 2.76$ TeV;
- (iii) normalise the generated rapidity distribution at $\sqrt{s} = 2.76$ TeV to the mid-rapidity value estimated by means of interpolation method;
- (iv) obtain a forward rapidity estimate for Υ cross-section by combining the calculations relative to the different Pythia6.4 tunes.

The quarkonium production in Pythia6.4 can be performed following the prediction of two models: the Colour Singlet Model (CSM) [19] and the non-relativistic QCD (NRQCD) [20]. The Pythia interface in the ALICE simulation framework was customised in order to handle these two models for the bottomonium generation. With the NRQCD setting, it is possible to produce all the bottomonium states, while the CSM one just produces the $\Upsilon(1S)$. Feed-down to $\Upsilon(1S)$ from higher mass bottomonia is thus included only in the NRQCD setting.

¹When dealing with asymmetric uncertainties, the largest between the positive and negative bar was taken.

In order to test the ability of Pythia6.4 to reproduce the rapidity distribution at $\sqrt{s} = 7$ TeV, the production of Υ was performed using the two different models, with the different parton distribution function (PDF) sets already available in the framework and different Pythia tunes. For each simulation, 80×10^3 bottomonium events were generated in the rapidity range $0 < y < 5.5$.

The $\Upsilon(1S)$ measurements in pp collisions at $\sqrt{s} = 7$ TeV from CMS [14] and LHCb [16] were chosen in order to test the Pythia6.4 calculations in the widest possible rapidity range. The statistical and systematic uncertainties quoted by the two experiments were summed in quadrature. The procedure for this test can be summarised as follow:

- (i) the rapidity distributions $\frac{dN^\Upsilon}{dy}$ of the generated Υ were binned as the experimental data;
- (ii) the ratios between the data and the simulation were fitted with a constant;
- (iii) the χ^2 of the fits was used as a measure of how compatible the generated distributions are with the measured one.

A $\chi^2/\text{ndf} < 1.5$ was adopted as the limit for accepting the fit. In Fig. 4.7, the simulated rapidity distributions that passed the tests were plotted together with the experimental points for a visual comparison. Beforehand, the distributions were multiplied by the normalisation parameter provided by the constant fit.

The extrapolation from mid to forward rapidity was performed by combining the results obtained simulating bottomonium states at $\sqrt{s} = 2.76$ TeV with the tunes that passed the test at 7 TeV as described previously. Rapidity distributions were obtained and normalised to the mid-rapidity interpolated crosssection. The $\frac{d\sigma^\Upsilon}{dy}$ in the muon spectrometer acceptance was computed for the rapidity bins used in this analysis as the integral, in the considered bin, of the rapidity distribution divided by the bin width.

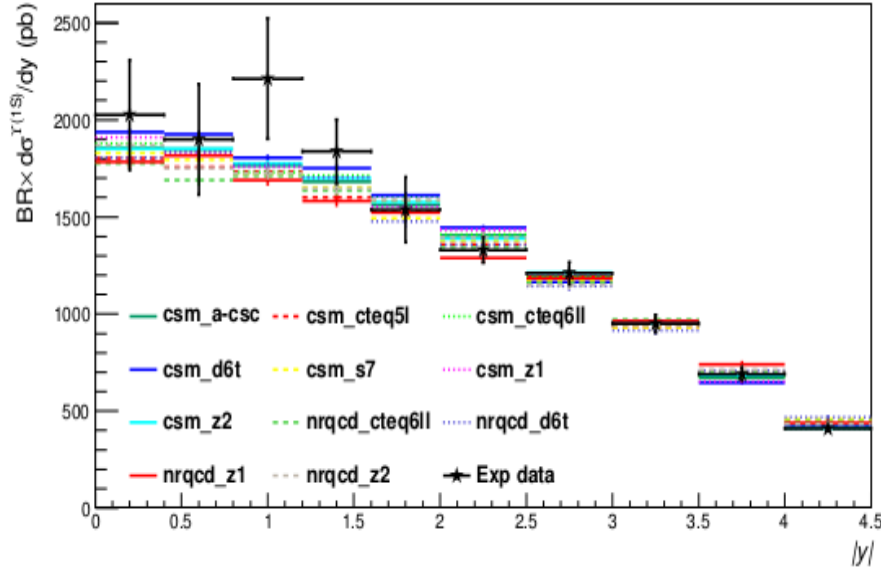


Figure 4.7: Experimental data points from CMS ($|y| < 2$) [14] and LHCb ($2.0 < y < 4.5$) [16] and $\frac{d\sigma^\Upsilon}{dy}$ distribution obtained from Pythia6.4.

In Table 4.8, the results for the $\frac{d\sigma^\Upsilon}{dy}$ at forward rapidity are summarised (after dividing by the $\Upsilon(1S) \rightarrow \mu^+\mu^-$ branching ratio $BR = 0.0248$ [7]). They were obtained with an average over the values coming from the different Pythia6.4 Υ productions at 2.76 TeV. Two separate contributions of the systematic uncertainty are quoted. The first component (Extr.) is associated to the extrapolation from mid to forward-rapidity and results from the spread of calculations obtained with the different tunes that passed the test at 7 TeV. It is evaluated as the difference between the average value and the maximum and minimum values, while the second component (Norm.) is related to the normalisation to the mid-rapidity point. The normalisation uncertainties are fully correlated with rapidity. The extrapolation uncertainties are taken uncorrelated with rapidity, since the spread observed among calculations is not the same from one bin to an other. The statistical uncertainties (from the number of generated Υ) and the uncertainty on the branching

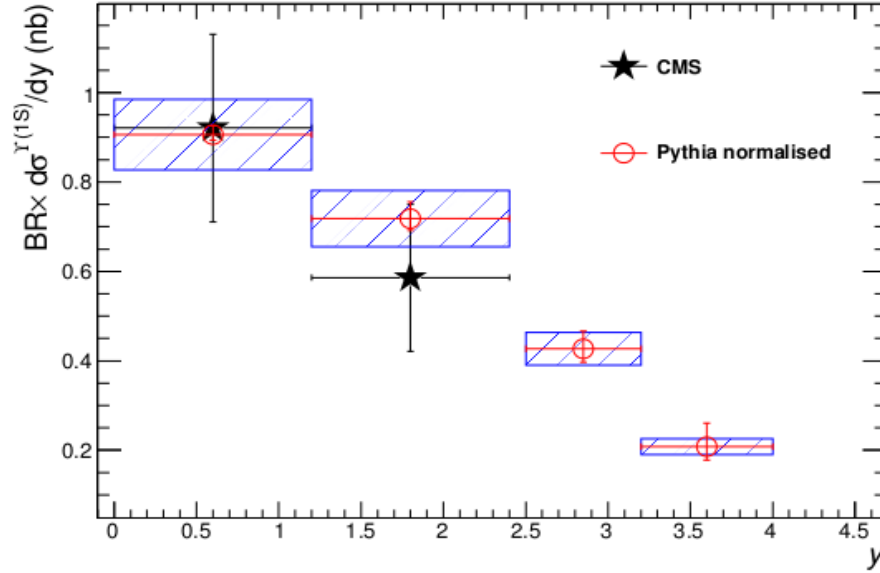


Figure 4.8: Combined Pythia6.4 $\text{BR} \times \frac{d\sigma^\Upsilon}{dy}$ for pp collisions at $\sqrt{s} = 2.76$ TeV, plotted together with CMS data points at mid-rapidity [13]. The error bars represent the uncorrelated uncertainty (Extr.) while the boxes represent the correlated one (Norm.).

ratio are negligible with respect to the systematic uncertainties. In Fig. 4.8, the obtained values at forward rapidity are plotted together with the CMS measurement [13] of $\frac{d\sigma^\Upsilon}{dy}$ in two rapidity bins.

Rapidity	$\frac{d\sigma^\Upsilon}{dy}$ (nb)
$2.5 < y < 4.0$	$12.5^{+1.9}_{-1.2}$ (Extr.) ± 1.1 (Norm.)
$2.5 < y < 3.2$	$17.2^{+1.6}_{-1.2}$ (Extr.) ± 1.5 (Norm.)
$3.2 < y < 4.0$	$8.4^{+2.1}_{-1.2}$ (Extr.) ± 0.7 (Norm.)

Table 4.8: Combined results for $\frac{d\sigma^\Upsilon}{dy}$ (nb) in pp collisions at $\sqrt{s} = 2.76$ TeV at forward rapidity. The uncertainty on the normalization (Norm.) is quoted separately from the one related to the spread between the extrapolated values at forward rapidity (Extr.).

4.7.3 Interpolation of $\Upsilon(1S)$ Cross Section Using LHCb Measurement

The above mentioned method gave us the pp cross-section in our desired rapidity bins. However in the mean time LHCb published a paper [21] on Υ cross-section at forward rapidity ($2.0 < y < 4.5$) at $\sqrt{s} = 2.76$ TeV for various rapidity bins as shown in the Table 4.9. LHCb provided the cross-section in the rapidity range $2.5 < y < 4$, but not in the $2.5 < y < 3.2$ and $3.2 < y < 4$ bins where we have extracted the signal, so an interpolation in rapidity was performed.

Rapidity	$BR \times \sigma^\Upsilon$ (nb)
$2.5 < y < 4.0$	0.670 ± 0.025 (stat.) ± 0.026 (syst.)
$2.0 < y < 2.5$	0.404 ± 0.034 (stat.) ± 0.022 (syst.)
$2.5 < y < 3.0$	0.321 ± 0.018 (stat.) ± 0.012 (syst.)
$3.0 < y < 3.5$	0.227 ± 0.013 (stat.) ± 0.008 (syst.)
$3.5 < y < 4.0$	0.124 ± 0.011 (stat.) ± 0.005 (syst.)
$4.0 < y < 4.5$	0.035 ± 0.008 (stat.) ± 0.002 (syst.)

Table 4.9: Inclusive $\Upsilon(1S)$ cross-section in pp collisions at $\sqrt{s} = 2.76$ TeV from LHCb [21] in various rapidity bins at forward rapidity.

The LHCb data points for various rapidity bins were fitted with various polynomial functions. The functions were integrated over the required rapidity ranges and, for each range, the fit results were averaged. The uncorrelated systematic uncertainties were obtained by summing in quadrature the largest fit uncertainty and the half spread of the different results obtained with the different fitting functions. Results in the $2.5 < y < 3.2$ and $3.2 < y < 4$ rapidity bins are given in Table 4.10. The LHCb systematic uncertainties were reported to be strongly correlated with rapidity but the degree of correlation was not provided. As an educated guess we have chosen to consider the minimum relative systematic uncertainty quoted for the various rapidity bins (Table 4.9) as fully correlated and it corresponds to the correlated uncertainty in our final results (Table 4.10).

ALICE preliminary results [22] were released when LHCb data were not avail-

Rapidity	$\frac{d\sigma^\Upsilon}{dy}$ (nb)
$2.5 < y < 3.2$	24.19 ± 1.04 (uncorr.) ± 0.86 (corr.)
$3.2 < y < 4.0$	12.75 ± 0.81 (uncorr.) ± 0.45 (corr.)

Table 4.10: Inclusive $\Upsilon(1S)$ cross-section per unit of rapidity in pp collisions at $\sqrt{s} = 2.76$ TeV obtained from the rapidity interpolation of LHCb data [21]. This result is 30% to 35% higher than data-driven method (Table 4.8). Results do not include the branching ratio of $\Upsilon(1S)$ decay to dimuon.

able and the pp reference cross-section was estimated using a data-driven method as explained in the earlier subsections (Table 4.8). Depending on the considered rapidity bin, the pp reference obtained with this approach and the LHCb data differ by 30% to 35%. Taking into account the uncertainties, the ALICE preliminary R_{AA} is 1.3 to 2.2σ larger than that of the final result.

4.8 Summary on Uncertainties

The source of statistical uncertainties are given in Table 4.11. The main source of statistical uncertainty comes from signal extraction.

Source	Centrality	Rapidity
N_{MB}	0.04%	0.04%
Signal Extraction	18%–22%	18%–23%
$A \times \epsilon$	0.6%	0.3%
pp Reference cross-section	< 1%	< 1%
Total	18%–23%	18%–24%

Table 4.11: Summary of statistical uncertainties.

The source of systematic uncertainties are given in Table 4.12. The systematic uncertainties are distinguished in uncorrelated (U) and correlated (C) uncertainties.

The uncorrelated systematic uncertainties for the R_{AA} estimated as a function of centrality come from the signal extraction and the nuclear overlap function. The correlated uncertainties arise from the pp reference cross-section, the estimate of

Source		Centrality	Rapidity
T_{AA}		3%–4% U	3% C
N_{MB}		4% C	4% C
Signal Extraction	background description	5%–6% U	4%–7% U
	mass position	0.3%–1% U	1%–5% U
	signal width	0.3%–0.6% U	0.4%–1% U
	tail parameters	2%–3% U	3%–4% U
	pDCA cut	0.3% U	0.1%–0.7% U
p_T and y parametrisation		4% C	5%–7% U
tracking efficiency		10% C	9%–11% U
trigger efficiency		2% C	2% U
matching efficiency		1% C	1% U
pp reference cross-section		4% C	4%–7% U, 4% C

Table 4.12: Summary of systematic uncertainties.

the number of MB events ² and the acceptance and efficiency correction.

The uncorrelated uncertainties for the R_{AA} as a function of rapidity come from the signal extraction and the efficiency correction. A part of the systematic uncertainties on the pp reference cross-section is also uncorrelated with rapidity. The correlated uncertainties are then the remaining part of the uncertainties on the pp reference cross-section, those on the number of MB events and those on the nuclear overlap function (in the 0% – 90% centrality bin).

For both studies as a function of centrality and rapidity, the acceptance and efficiency correction is the dominant contribution to the overall systematic uncertainty. The uncertainties on signal extraction come next. Quantitative information are summarized in Table 4.13.

Bin Condition	Signal Extraction (%)	$A \times \epsilon$ (%)	N_{MB} (%)	$\langle T_{AA} \rangle$ (%)	σ_{pp} (uncorr.) (%)	σ_{pp} (corr.) (%)
0%–90%	5	11	4	3	none	4
0%–20%	7	11	4	3	none	4
20%–90%	6	11	4	4	none	4
$2.5 < y < 3.2$	5	12	4	3	4	4
$3.2 < y < 4.0$	10	12	4	3	7	4

Table 4.13: Summary of systematic uncertainties for various bins.

²This uncertainty reflects the spread of the F_{norm} scaling factor over the data taking period.

4.9 Results

The R_{AA} values for the various centrality and rapidity bins along with the average number of participants $\langle N_{part} \rangle$ are summarized in Table 4.14.

Centrality ($\langle N_{part} \rangle$)	Rapidity	R_{AA}
0%–90% (124)	$2.5 < y < 4.0$	$0.30 \pm 0.05(\text{stat.}) \pm 0.02(\text{uncorr.}) \pm 0.04(\text{corr.})$
0%–20% (308)	$2.5 < y < 4.0$	$0.22 \pm 0.05(\text{stat.}) \pm 0.02(\text{uncorr.}) \pm 0.03(\text{corr.})$
20%–90% (72)	$2.5 < y < 4.0$	$0.44 \pm 0.09(\text{stat.}) \pm 0.03(\text{uncorr.}) \pm 0.05(\text{corr.})$
0%–90% (124)	$2.5 < y < 3.2$	$0.30 \pm 0.05(\text{stat.}) \pm 0.04(\text{uncorr.}) \pm 0.02(\text{corr.})$
0%–90% (124)	$3.2 < y < 4.0$	$0.29 \pm 0.07(\text{stat.}) \pm 0.05(\text{uncorr.}) \pm 0.02(\text{corr.})$

Table 4.14: Values of the R_{AA} measured in Pb-Pb collisions at $\sqrt{s_{NN}} = 2.76$ TeV.

The R_{AA} of inclusive $\Upsilon(1S)$ measured in the range $2.5 < y < 4$ and $p_T > 0$ is shown in Fig. 4.9(left) as a function of $\langle N_{part} \rangle$. The statistical uncertainties (bars) dominate over the correlated systematic uncertainties (open boxes) and the uncorrelated systematic uncertainties (filled boxes). In 0%–90% central events, the R_{AA} is $R_{AA}^{0\%-90\%} = 0.30 \pm 0.05(\text{stat.}) \pm 0.02(\text{uncorr.}) \pm 0.04(\text{corr.})$, indicating a strong suppression of inclusive $\Upsilon(1S)$. In addition, the suppression increases with centrality.

The R_{AA} of inclusive $\Upsilon(1S)$ integrated over centrality (0%–90%) is shown in Fig. 4.9(right) in two rapidity bins ($2.5 < y < 3.2$ and $3.2 < y < 4$), for $p_T > 0$. The statistical uncertainties (bars) are larger than the uncorrelated systematic uncertainties (filled boxes) and larger than the correlated systematic uncertainties (open boxes). Correlated systematic uncertainties are dominated by the other sources. No clear rapidity dependence can be observed within the statistical and uncorrelated systematic uncertainties.

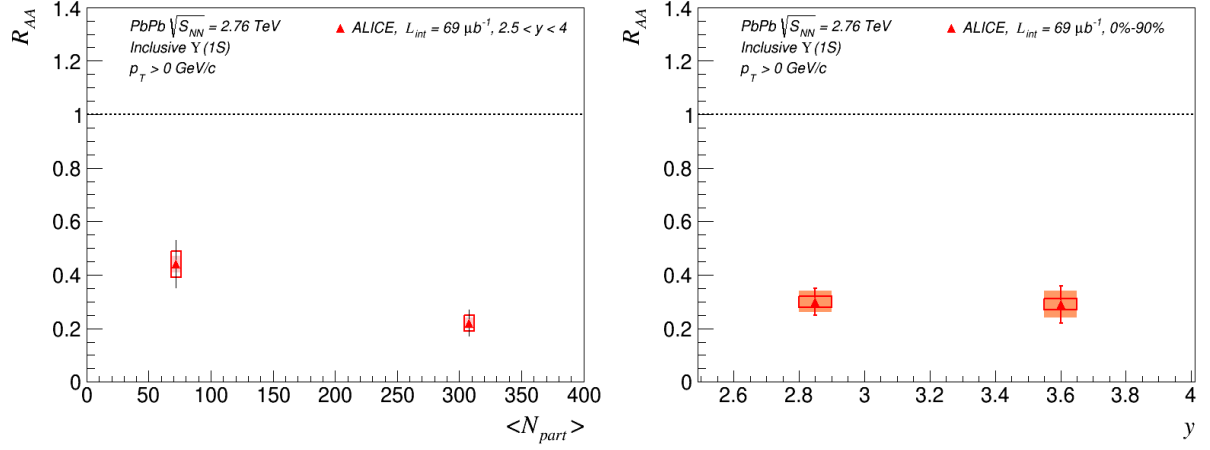


Figure 4.9: Nuclear modification factor of the inclusive $\Upsilon(1S)$ as a function of the average number of participant nucleons (left) and as a function of rapidity (right). Bars stand for statistical uncertainties and filled (open) boxes uncorrelated (correlated) for uncertainties.

4.10 Discussion

4.10.1 Comparison with J/ψ data from ALICE at forward rapidity

In Fig. 4.10(left), the R_{AA} of inclusive $\Upsilon(1S)$ is compared with the ALICE R_{AA} of inclusive J/ψ [23] obtained in the same kinematic range ($2.5 < y < 4$, $p_T > 0$). The $\Upsilon(1S)$ suppression is larger than that of the J/ψ . In particular, the R_{AA} value is about two time larger for J/ψ than for $\Upsilon(1S)$ in central collisions while the results are closer for semi-peripheral ones. Fig. 4.10(right) shows the ALICE $\Upsilon(1S)$ and J/ψ [23] R_{AA} as a function of rapidity. Both results are integrated over the 0%–90% centrality range. $\Upsilon(1S)$ states are more suppressed than J/ψ and the difference between the R_{AA} values is the largest in the $2.5 < y < 3.2$ rapidity range.

Comparisons between theory and data have suggested an important contribution of J/ψ (re-)generation in Pb-Pb collisions at $\sqrt{s_{NN}} = 2.76$ TeV [23], while in

the $\Upsilon(1S)$ case this contribution is expected to be much less important. Besides, the feed-down contribution to the $\Upsilon(1S)$ state is expected to be substantial and could be of the order of 40%–50% [16, 24, 25] from χ_b , $\Upsilon(2S)$ and $\Upsilon(3S)$. These states are expected to be suppressed at LHC energies. For these reasons it is plausible that the observed R_{AA} is smaller for inclusive Υ measurement than that for inclusive J/ψ measurement, although the energy loss for charm quark is expected to be higher than that of the bottom quark [26].

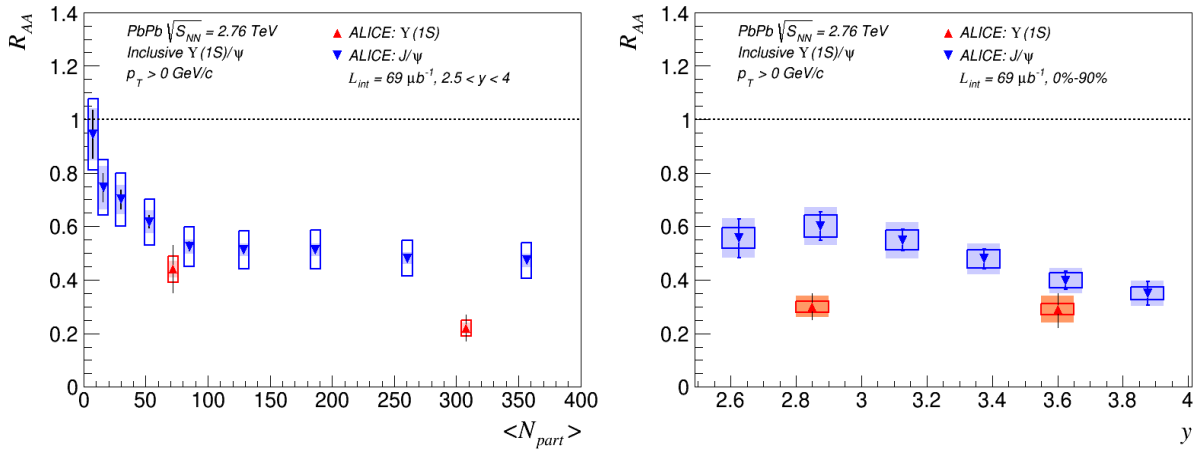


Figure 4.10: Comparison of the ALICE nuclear modification factor of inclusive $\Upsilon(1S)$ and J/ψ [23] in the same kinematic range. Left (Right): results are shown as a function of the average number of participant nucleons (rapidity). Bars stand for statistical uncertainties and filled (open) boxes for uncorrelated (correlated) uncertainties.

4.10.2 Comparison with $\Upsilon(1S)$ data from the CMS Collaboration

The R_{AA} of inclusive $\Upsilon(1S)$ measured in the $2.5 < y < 4$ rapidity range is compared with the CMS data obtained in the range $|y| < 2.4$ [27]. Both ALICE and CMS experiments measure the $\Upsilon(1S)$ state down to $p_T = 0$. The comparison of the R_{AA} as a function of the average number of participant nucleons is shown

in Fig. 4.11(left). In central collisions ($\langle N_{\text{part}} \rangle = 308$), the suppression observed at forward rapidity is stronger than at mid-rapidity.

The ALICE and CMS R_{AA} as a function of rapidity are compared in Fig. 4.11(right). The CMS and ALICE data are integrated over an equivalent centrality range (0%–100% for CMS and 0%–90% for ALICE). The value of the $\Upsilon(1S)$ R_{AA} in $2.5 < y < 4$ is significantly lower than in $|y| < 2.4$.

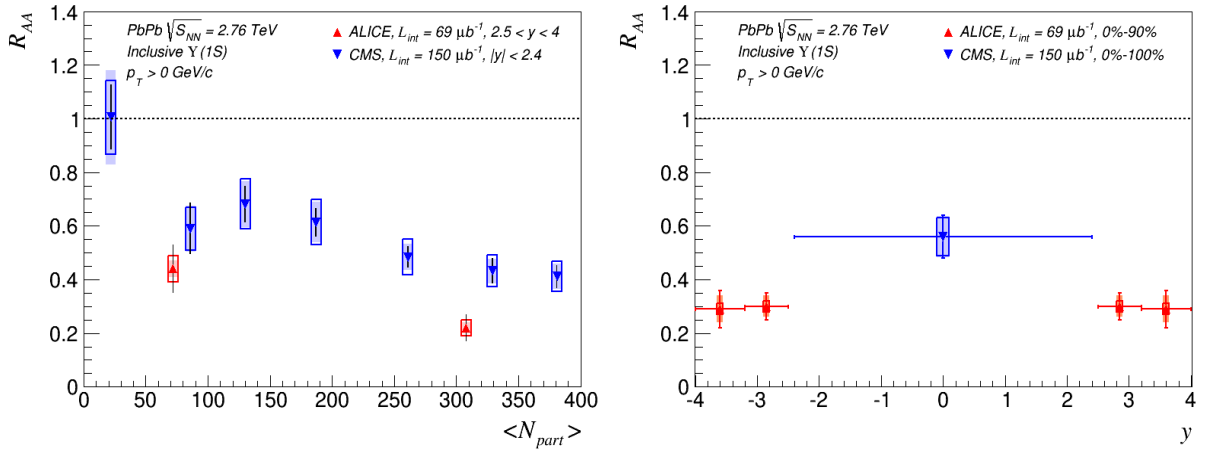


Figure 4.11: Left (Right): ALICE and CMS [27] nuclear modification factor of inclusive $\Upsilon(1S)$ production as a function of the average number of participant nucleons (rapidity). Bars stand for statistical uncertainties and filled (open) boxes uncorrelated (correlated) for uncertainties. On the right plot, open points are reflected with respect to the measured ones.

4.11 Comparison with theoretical predictions

4.11.1 Dynamical model

The observed $\Upsilon(1S)$ nuclear modification factor has been compared with the theoretical predictions by M. Strickland et al. [28, 29, 30]. The predictions are based on a potential model to determine the impact of the Quark-Gluon Plasma phase on bottomonium suppression. The short-range part of the potential was

computed to leading-order in the strong coupling constant using finite temperature Quantum Chromodynamics in the heavy quark limit [31, 32, 33, 34, 35]. For the long-range part, a parametrisation of the finite-temperature Cornell potential [36] was used. The resulting potential is complex-valued with the imaginary part being related to the in-medium decay of heavy quark bound states due to Landau damping of the gluon quasi-particle excitations in the plasma. Bottomonium states and their decay widths are studied using this potential and then the obtained information is integrated over the space-time evolution of the Quark-Gluon Plasma using a hydrodynamics formalism (HYDRO) [37, 38, 39] which assumes finite local momentum-space anisotropy due to finite shear viscosity. In particular, the effect of the momentum space anisotropy is taken into account on the real and imaginary part of the heavy quark potential [40]. The model only includes the effects of in-medium suppression of bottomonium states. Therefore, it does not include recombination or Cold Nuclear Matter (CNM) effects.

In Fig. 4.12 two sets of calculations are presented [28]. They correspond to different initial temperature profiles in rapidity. One case assumes a broad plateau containing a boost-invariant central rapidity region with half-Gaussian tails in the forward and backward directions which corresponds to limited fragmentation. This profile is expected in the Bjorken picture of heavy-ion collisions [41]. The other case assumes a Gaussian profile which corresponds to the Landau picture [42]. Three plasma shear viscosity to entropy density ratios were considered for each profile ($4\pi\eta/s = 1, 2, 3$) and are depicted by the bottom, the middle and the top lines, respectively. None of the proposed calculations reproduce the ALICE data and the observed suppression is underestimated in all cases. In particular, the R_{AA} rapidity dependence predicted in the wide range probed by ALICE and CMS is the opposite of the measured one. However, the suppression calculated

with the minimum possible value of $4\pi\eta/s$ ($4\pi\eta/s = 1$) in the Bjorken scenario is the most pronounced, shows the largest centrality dependence and is closest to the measurement results.

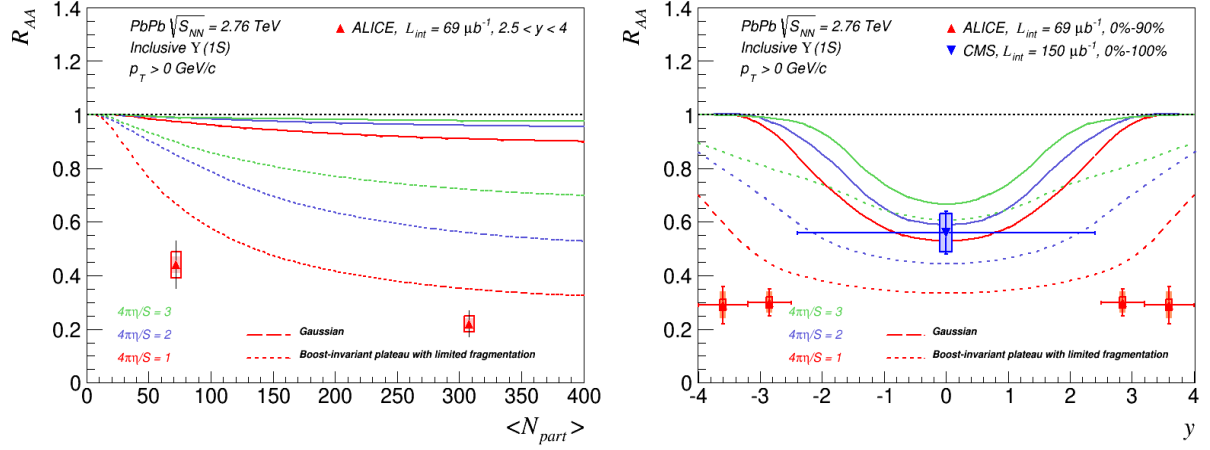


Figure 4.12: Left (Right): ALICE R_{AA} of inclusive $\Upsilon(1S)$ as a function of the average number of participant nucleons (rapidity) compared with theoretical predictions from [28]. The CMS data point at mid-rapidity is included in the rapidity plot. Bars stand for statistical uncertainties and filled (open) boxes for uncorrelated (correlated) uncertainties. On the right plot, open points are reflected with respect to the measured ones.

4.11.2 Transport models

The observed $\Upsilon(1S)$ R_{AA} has also been compared with the theoretical predictions by A. Emerick et al. [43, 44, 45]. In this model a strongly bound bottomonia scenario assuming that Υ states remain at their vacuum mass and binding energy independently of the QGP temperature is considered. Therefore, the in-medium dissociation of the direct $\Upsilon(1S)$ is very small while that of the higher mass states is substantial. In this framework $\Upsilon(1S)$ are slightly regenerated. The suppression and regeneration contributions are implemented by means of a rate equation and the spatio-temporal evolution of the medium is described with a fireball model tuned according to the recent LHC measurements [46].

The rate equation requires an initial condition for the number of bottomonia at the QGP formation time and the implemented regeneration component requires the knowledge of the beauty quark cross-section. These information have been evaluated from data driven methods. The CNM effects are described by means of an effective absorption cross-section (σ_{abs}) including the effects of the nuclear modifications of parton distribution functions, the effects of the absorption in CNM and the Cronin effect.

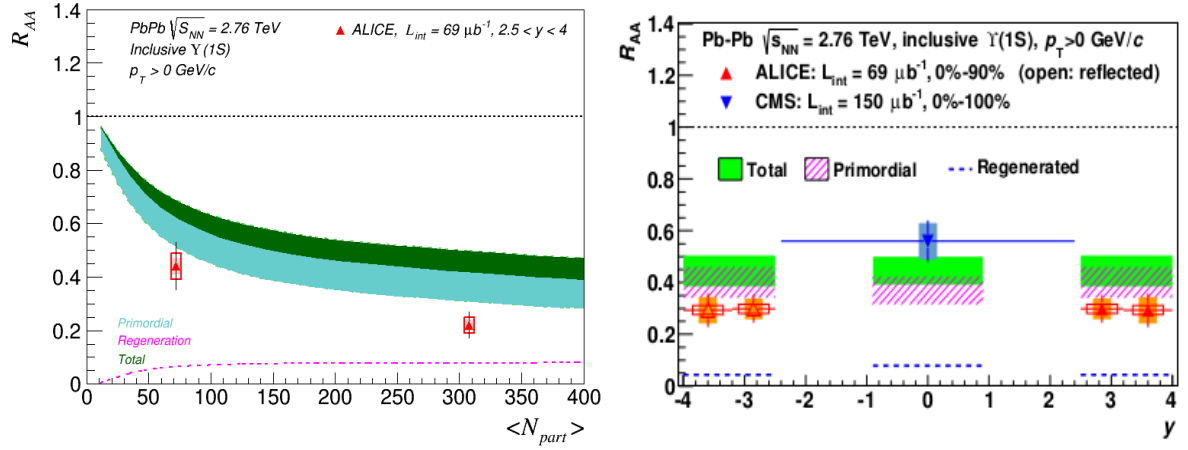


Figure 4.13: ALICE nuclear modification factor of inclusive $\Upsilon(1S)$ as a function of the average number of participant nucleons (left) and rapidity (right) compared with theoretical predictions from [43, 44, 45]. The CMS data point at mid-rapidity is included in the rapidity plot. Bars stand for statistical uncertainties and filled (open) boxes for uncorrelated (correlated) uncertainties. On the right plot, open points are reflected with respect to the measured ones.

In Fig. 4.13(left), the predictions are shown as a function of the number of participant nucleons. The R_{AA} of inclusive, primordial and regenerated $\Upsilon(1S)$ are represented as bands obtained with two extreme values for σ_{abs} ($\sigma_{\text{abs}} = 0$ mb and $\sigma_{\text{abs}} = 2.0$ mb). As expected, the primordial $\Upsilon(1S)$ component dominates over the regeneration one. The R_{AA} measured by ALICE is shown in the same figure and is overestimated by the calculation which, however, reproduces the decreasing trend of the R_{AA} . In Fig. 4.13(right), the predictions are compared with the ALICE and

CMS data shown as a function of rapidity. Due to the complementary nature of the rapidity dependence of suppression and regeneration, the transport model predicts a R_{AA} which remains rather constant as a function of rapidity. However, this result is not confirmed by the ALICE and CMS data.

In Fig. 4.14, the ALICE R_{AA} is compared with the predictions of another transport model by Zhou et al [47, 48]. The calculation results are rather close to those from [43, 44] but the theoretical approach is different. Contrary to [43, 44] which explores the sensitivity of heavy ion data to Υ state spectral properties within a given scenario for the temperature dependence of the state binding energies, in the present case, potential model results are quantitatively implemented in [47, 48]. Nevertheless, in both models, it is assumed an ideal hydro-dynamical evolution for the QGP and the use of the kinematic rate equation implies a small regeneration component for $\Upsilon(1S)$. Besides, the feed-down from higher mass bottomonia effects are included and direct $\Upsilon(1S)$ are almost not dissociated in the QGP. Finally, CNM effects are considered and, in [47, 48], they are evaluated employing the EKS98 shadowing parametrization [49].

In Fig. 4.14, the R_{AA} is shown as a function of the centrality together with the predictions from [47, 48]. The model calculations reproduce the centrality dependence of the ALICE data, but the observed suppression is underestimated. In Fig. 9 (right), the ALICE and CMS R_{AA} are shown as a function of the rapidity. The model reproduces well the CMS data but underestimates the strong suppression observed at forward rapidity and fails to reproduce its rapidity dependence.

In the transport [43, 44, 45, 47, 48] and the dynamical [43, 44, 45] models the inclusive $\Upsilon(1S)$ suppression is largely explained by the in-medium dissociation of higher mass bottomonia. Since both the models overestimate the measured R_{AA} , it might indicate that they underestimate the suppression of direct $\Upsilon(1S)$ as

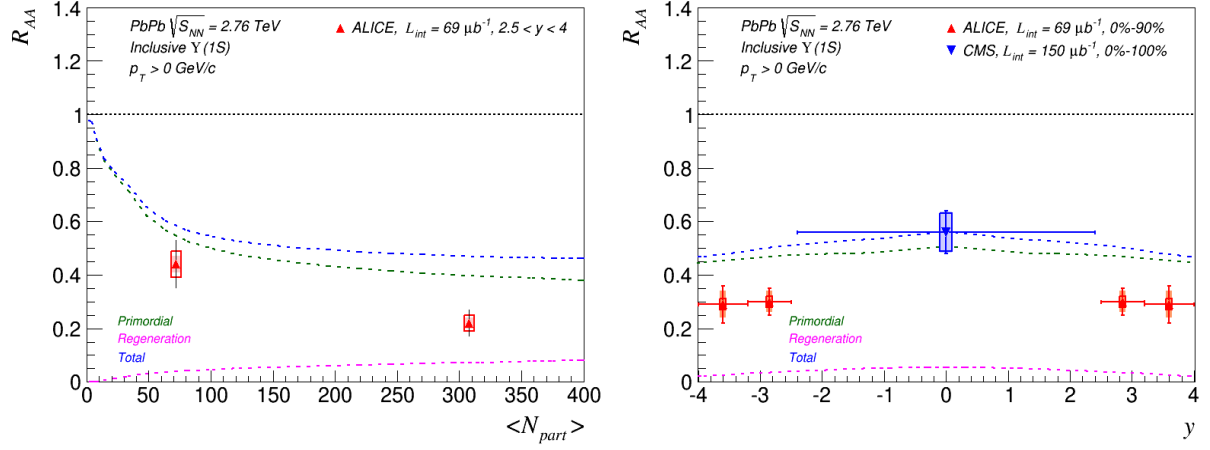


Figure 4.14: ALICE nuclear modification factor of inclusive $\Upsilon(1S)$ as a function of the average number of participant nucleons (left) and as a function of rapidity (right) compared with theoretical predictions from [47, 48]. The CMS data point at mid-rapidity is included in the rapidity plot. Bars stand for statistical uncertainties and filled (open) boxes for uncorrelated (correlated) uncertainties. On the right plot, open points are reflected with respect to the measured ones.

well. However, the assumptions on the magnitude of CNM effects and on the contribution of the feed-down from higher mass bottomonia need to be verified and constrained by accurate data.

4.12 Summary

The inclusive $\Upsilon(1S)$ nuclear modification factor in Pb-Pb collisions at $\sqrt{s_{NN}} = 2.76$ TeV has been measured down to $p_T = 0$ in the $2.5 < y < 4$ rapidity and 0%–90% centrality ranges. We obtained $R_{AA}^{0\%-90\%} = 0.30 \pm 0.05(\text{stat.}) \pm 0.02(\text{uncorr.}) \pm 0.04(\text{corr.})$ corresponding to a strong suppression of inclusive $\Upsilon(1S)$. Two centrality ranges were studied and the suppression is more pronounced in most central collisions. The R_{AA} was also measured in two rapidity bins and, within uncertainties, no significant rapidity dependence was observed in the range probes by the ALICE muon spectrometer.

The data were compared with the ALICE J/ψ results obtained in the same kinematic range. The $\Upsilon(1S)$ is more suppressed than the J/ψ and the difference of R_{AA} is particularly pronounced in the 0%–20% ($2.5 < y < 3.2$) centrality (rapidity) bin. The interpretation of these results is not straightforward due to the different sizes of the expected feed-down and (re-)generation effects for the two quarkonium states.

The $\Upsilon(1S)$ R_{AA} was also compared with CMS data measured in the $|y| < 2.4$ rapidity region and down to $p_T = 0$. The inclusive $\Upsilon(1S)$ yield measured at forward rapidity by ALICE is more suppressed than that measured at mid-rapidity by CMS.

The predictions provided within a spectral function approach with complex potential [29], based on a plasma description by means of an anisotropic hydrodynamic formalism, not including regeneration effects and neglecting CNM effects overestimate the ALICE R_{AA} . Two transport models, [43] and [47], including CNM effects and a small regeneration component for bottomonia in a plasma evolving according to ideal hydrodynamics were also considered. They underestimate the suppression measured by ALICE. These models also fail to reproduce the rapidity dependence of the observed suppression at LHC.

A better understanding of Υ production in AA collisions requires a precise measurement of feed-down from higher mass bottomonia and CNM effects at forward rapidity. In the next chapter, we will discuss p–Pb collisions at $\sqrt{s_{NN}} = 5.02$ TeV, which will give further insight to the CNM effects on Υ productions.

Bibliography

- [1] B. Abelev et al. [ALICE Collaboration], Phys. Rev. Lett. **109** (2012) 252302 [arXiv:1203.2436 [nucl-ex]].
- [2] B. Abelev et al. [ALICE Collaboration], arXiv:1301.4361 [nucl-ex].
- [3] A. Toia, J. Phys. G **38** (2011) 124007, [arXiv:1107.1973 [nucl-ex]].
- [4] M. L. Miller, K. Reygers, S. J. Sanders, and P. Steinberg, Ann. Rev. Nucl. Part. Sci. **57** (2007) 205 [nucl-ex/0701025].
- [5] K. Aamodt et al. [ALICE Collaboration], Phys. Rev. Lett. **106** (2011) 032301 [arXiv:1012.1657 [nucl-ex]].
- [6] V. Kumar, P. Shukla and R. Vogt, Phys. Rev. C **86** (2012) 054907 [arXiv:1205.3860 [hep-ph]].
- [7] J. Beringer et al. [Particle Data Group Collaboration], Phys. Rev. D **86** (2012) 010001.
- [8] F. Bossu, Z. C. del Valle, A. de Falco, M. Gagliardi, S. Grigoryan and G. Martinez Garcia, arXiv:1103.2394 [nucl-ex].

Bibliography

- [9] GEANT - Detector description and simulation tool, CERN Program Library Long Write-up W5013, CERN Geneva.
- [10] K. Aamodt et al. [ALICE Collaboration], Phys. Lett. B **704** (2011) 442 [Erratum-ibid. B **718** (2012) 692] [arXiv:1105.0380 [hep-ex]].
- [11] D. Acosta et al. [CDF Collaboration], Phys. Rev. Lett. 88 (2002) 161802.
- [12] V. M. Abazov et al. [D0 Collaboration], Phys. Rev. Lett. 94 (2005) 232001 [Erratum-ibid. 100 (2008) 049902] [hep-ex/0502030].
- [13] S. Chatrchyan et al. [CMS Collaboration], JHEP 1205, 063 (2012) [arXiv:1201.5069 [nucl-ex]].
- [14] V. Khachatryan et al. [CMS Collaboration], Phys. Rev. D 83, 112004 (2011) [arXiv:1012.5545 [hep-ex]].
- [15] T. Sjostrand, S. Mrenna and P. Z. Skands, JHEP 0605, 026 (2006) [hep-ph/0603175].
- [16] R. Aaij et al. [LHCb Collaboration], Eur. Phys. J. C 72, 2025 (2012) [arXiv:1202.6579 [hep-ex]].
- [17] M. Gluck, J. F. Owens and E. Reya, Phys. Rev. D **17** (1978) 2324.
- [18] M. Cacciari, S. Frixione, N. Houdeau, M. L. Mangano, P. Nason and G. Ridolfi, JHEP **1210** (2012) 137 [arXiv:1205.6344 [hep-ph]].

Bibliography

- [19] N. Brambilla et al. [Quarkonium Working Group Collaboration], hep-ph/0412158.
- [20] G. T. Bodwin, E. Braaten and G. P. Lepage, Phys. Rev. D **51**, 1125 (1995) [Erratum-ibid. D **55**, 5853 (1997)] [hep-ph/9407339].
- [21] R. Aaij et al. [LHCb Collaboration], Eur. Phys. J. C **74** (2014) 2835 [arXiv:1402.2539 [hep-ex]].
- [22] P. Khan for the ALICE Collaboration, arXiv:1310.2565 [nucl-ex].
- [23] B. B. Abelev et al. [ALICE Collaboration], arXiv:1311.0214 [nucl-ex].
- [24] R. Aaij et al. [LHCb Collaboration], JHEP **1211** (2012) 031 [arXiv:1209.0282 [hep-ex]].
- [25] T. Affolder et al. [CDF Collaboration], Phys. Rev. Lett. **84** (2000) 2094 [hep-ex/9910025].
- [26] E. Braaten and M. H. Thoma, Phys. Rev. D **44** (1991) R2625(R).
- [27] S. Chatrchyan et al. [CMS Collaboration], Phys. Rev. Lett. **109** (2012) 222301 [arXiv:1208.2826 [nucl-ex]].
- [28] M. Strickland, AIP Conf. Proc. **1520** (2013) 179 [arXiv:1207.5327 [hep-ph]].
- [29] M. Strickland, Phys. Rev. Lett. **107** (2011) 132301 [arXiv:1106.2571 [hep-ph]].

- [30] M. Strickland and D. Bazow, Nucl. Phys. A **879**, 25 (2012) [arXiv:1112.2761 [nucl-th]].
- [31] M. Laine, O. Philipsen, P. Romatschke and M. Tassler, JHEP **0703**, 054 (2007) [hep-ph/0611300].
- [32] A. Dumitru, Y. Guo and M. Strickland, Phys. Lett. B **662**, 37 (2008) [arXiv:0711.4722 [hep-ph]].
- [33] N. Brambilla, J. Ghiglieri, A. Vairo and P. Petreczky, Phys. Rev. D **78**, 014017 (2008) [arXiv:0804.0993 [hep-ph]].
- [34] Y. Burnier, M. Laine and M. Vepsalainen, Phys. Lett. B **678**, 86 (2009) [arXiv:0903.3467 [hep-ph]].
- [35] A. Dumitru, Y. Guo and M. Strickland, Phys. Rev. D **79**, 114003 (2009) [arXiv:0903.4703 [hep-ph]].
- [36] F. Karsch, M. T. Mehr and H. Satz, Z. Phys. C **37**, 617 (1988).
- [37] R. Ryblewski and W. Florkowski, J. Phys. G **38**, (2011) 015104 [arXiv:1103.1260 [nucl-th]].
- [38] M. Martinez and M. Strickland, Nucl. Phys. A **848** (2010) 183 [arXiv:1007.0889 [nucl-th]].
- [39] M. Martinez and M. Strickland, Nucl. Phys. A **856** (2011) 68 [arXiv:1011.3056 [nucl-th]].

- [40] M. Margotta, K. McCarty, C. McGahan, M. Strickland and D. Yager-Elorriaga, Phys. Rev. D **83** (2011) 105019 [Erratum-ibid. D **84** (2011) 069902] [arXiv:1101.4651 [hep-ph]].
- [41] J. D. Bjorken, Phys. Rev. D **27** (1983) 140.
- [42] L. D. Landau, Izv. Akad. Nauk SSSR, Ser. Fiz. **17**, 51 (1953).
- [43] A. Emerick, X. Zhao and R. Rapp, Eur. Phys. J. A **48** (2012) 72 [arXiv:1111.6537 [hep-ph]].
- [44] L. Grandchamp, S. Lumpkins, D. Sun, H. van Hees and R. Rapp, Phys. Rev. C **73** (2006) 064906 [hep-ph/0507314].
- [45] R. Rapp et al. priv. comm.
- [46] X. Zhao and R. Rapp, Nucl. Phys. A **859** (2011) 114 [arXiv:1102.2194 [hep-ph]].
- [47] K. Zhou, N. Xu and P. Zhuang, arXiv:1309.7520 [nucl-th].
- [48] K. Zhou, N. Xu, Z. Xu and P. Zhuang, arXiv:1401.5845 [nucl-th].
- [49] K. J. Eskola, V. J. Kolhinen and C. A. Salgado, Eur. Phys. J. C **9** (1999) 61 [hep-ph/9807297].

Chapter 5

Upsilon(Υ) Production in p-Pb Collisions

In this chapter the detail analysis of Υ production in p-Pb collisions has been discussed. Like Pb-Pb, the data has been collected by ALICE Muon Spectrometer in specific trigger conditions at $\sqrt{s_{NN}} = 5.02$ TeV in January and February 2013. The analysis has been performed at forward rapidity ($2.04 < y_{cms} \leq 3.54$) as well as backward rapidity ($-4.46 < y_{cms} \leq -2.96$) with data sample corresponding to an integrated luminosity of $5.01 \pm 0.17 \text{ nb}^{-1}$ and $5.81 \pm 0.18 \text{ nb}^{-1}$ respectively.

5.1 Data Selection

In ALICE the Muon Spectrometer is in one direction, which is by convention considered as negative z-direction¹. As a result when two different kind of beams (like proton and lead) are collided, the coverage of the Muon Spectrometer be-

¹In the ALICE reference frame, the positive z-direction is along the counter clockwise beam direction. Thus, the muon spectrometer covers a negative pseudo-rapidity (η) range and a negative y_{lab} range. In this note the results will be presented with a positive y_{lab} notation keeping the η values signed.

comes positive or negative depending on the direction of the higher energy beam with respect to the Muon Spectrometer. In p-Pb, beam-1 consists of protons at 4 TeV energy circulating towards the Muon spectrometer in the negative z direction while beam-2 consists of fully stripped Pb ions at ($\frac{82 \times 4}{204}$) TeV energy per nucleon circulating in the positive z direction. This configuration resulted in collisions at $\sqrt{s_{NN}} = 5.02$ TeV and in a nucleon-nucleon center-of-mass system that moves with a rapidity of $\Delta y_{NN} = 0.465$ in the proton beam. Thus the rapidity in center-of-mass system of the Muon spectrometer cover the region $2.04 < y_{cms} < 3.54$ in p-Pb collisions and $-4.46 < y_{cms} < -2.96$ in Pb-p collisions. These two rapidity ranges overlap in the region $2.96 < |y_{cms}| < 3.54$ which correspond to $3.43 < y_{lab} < 4$ and $2.5 < y_{lab} < 3.07$ for p-Pb and Pb-p collisions, respectively.

5.1.1 Event Selection

The data passed the standard quality check for the detectors considered in the analysis (V0, SPD, ZDC, muon tracking and trigger chambers). Different triggers were activated during data taking. The Minimum Bias (MB) trigger was defined as the coincidence of signal in VZERO-A and VZERO-C detectors synchronized with the passage of the colliding lead and proton bunches. During the rare trigger periods (LHC13d and LHC13e for p-Pb and LHC13f for Pb-p collisions), the MB trigger was down-scaled at the L0 level to allow more DAQ bandwidth for the rare triggers. In particular, the unlike sign dimuon low- p_T trigger (p_T^μ threshold² ~ 0.5 GeV/c) or MUL was used in this analysis. Beam induced background was reduced at the offline level by timing cuts on the signals from the VZERO and from the ZDC. This physics selection removed from few percent up to 10% of the events

²The threshold is defined as the p_T^μ value below which the trigger efficiency for single muons becomes lower than 50%.

depending on the run and the collision type.

In total, after applying the event physics selection, a data sample of 9.27 million p-Pb collisions and 20.90 million Pb-p collisions triggered by unlike-sign dimuon were collected. This number had to be multiplied by the normalization factor F to obtain the equivalent number of Minimum Bias events. The total integrated luminosities were measured to amounts for $5.01 \pm 0.17 \text{ nb}^{-1}$ in p-Pb collisions and $5.81 \pm 0.18 \text{ nb}^{-1}$ in Pb-p collision. In the following, the two periods LHC13d and LHC13e with p-Pb collisions are considered all together.

5.1.2 Track Selection

In order to reduce the background, the following tight selection criteria on single muon tracks were applied:

- all tracks reconstructed in the tracking chambers should match a track segment in the trigger chambers (low- p_T threshold $\sim 0.5 \text{ GeV}/c$). Because of the thick iron wall located upstream of the trigger system, this cut rejected efficiently the tracks of light hadrons which escape from the front absorber and a part of the low momentum muons coming mainly from π and K decays.
- only tracks with pseudo-rapidity in $-4 < \eta < -2.5$ were selected in order to reject the ones reconstructed at the edges of the detector where the efficiency is small.
- tracks with a transverse radius coordinate at the end of the absorber (R_{abs}) in the interval $17.6 < R_{\text{abs}} < 89.5 \text{ cm}$ were selected. The tracks crossing the high density material around the beam pipe, where multiple scattering is large, were then significantly rejected. This cut improved the mass resolution.

- tracks should point to the interaction vertex. This requirement can be achieved by selecting tracks according to the value of their $p \times \text{DCA}$. This quantity is defined as the product of the track momentum (p) by the distance of the extrapolated track to the transverse plane containing the vertex (DCA: Distance of Closest Approach). This additional selection significantly reduced the amount of fake tracks contaminating the muon sample, which leads to increase of the combinatorial background.

5.2 Signal Extraction

The Υ candidates were formed by combining pairs of opposite-sign (OS) tracks reconstructed in the muon spectrometer and selected as previously described. In addition, dimuons with a rapidity in the range $2.5 < y_{\text{lab}} < 4$ were selected. The OS dimuon invariant mass distribution was fitted with the sum of five functions — three Double Crystal Ball functions for the three resonances of Υ and sum of two double exponential functions to describe the background continuum. These functions have been discussed extensively in the previous chapter.

5.2.1 Fit Procedure

In this analysis, the amplitude parameters of the three Extended Crystal Ball functions were left free as well as the position and the width of the $\Upsilon(1S)$. Because of the low statistics observed for invariant masses above $\sim 9 \text{ GeV}/c^2$, the width and the position of the $\Upsilon(2S)$ and $\Upsilon(3S)$ were constrained. The position of the $\Upsilon(2S)$ and $\Upsilon(3S)$ peaks were fixed to that of the $\Upsilon(1S)$ according to the PDG [2] mass difference, while their widths were forced to scale proportionally to that of the $\Upsilon(1S)$ according to the ratio of the resonance masses. Besides, the signal distribu-

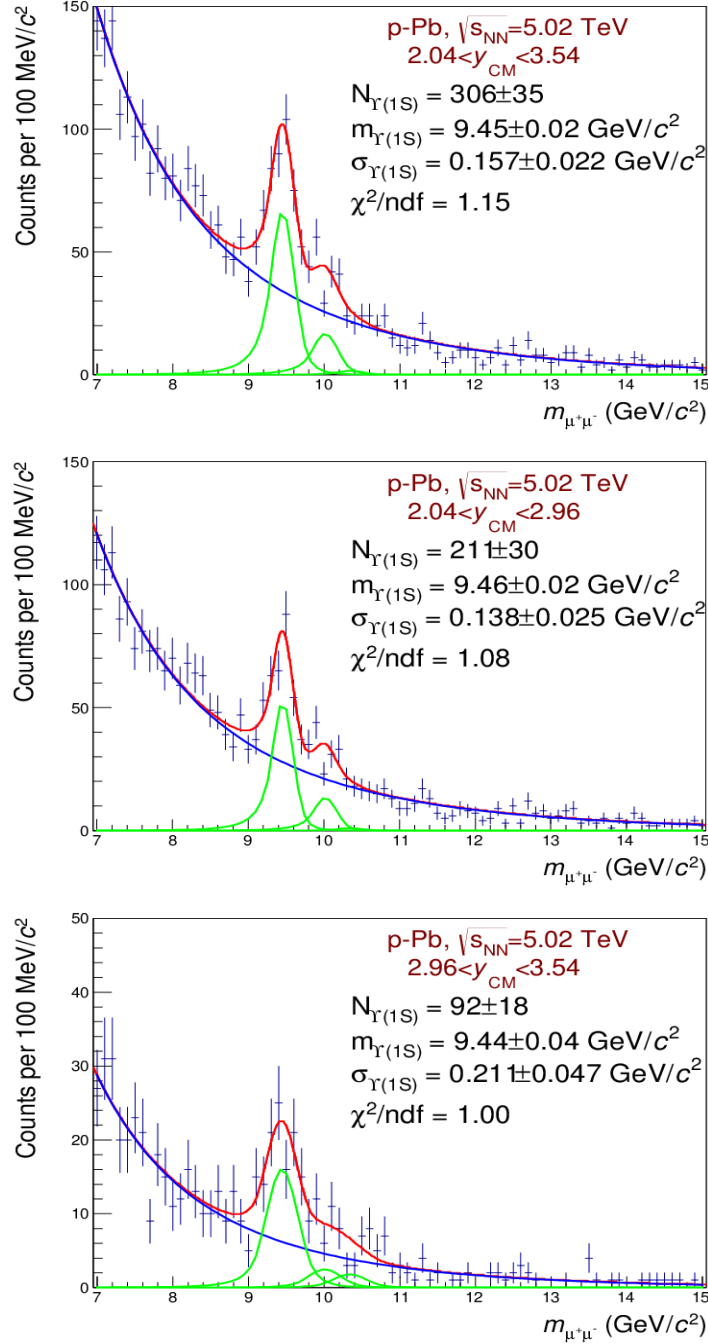


Figure 5.1: Fit procedure applied on the invariant mass distributions of opposite-sign dimuons in the different rapidity bins consider in this analysis at forward rapidity. The total fit function is represented by the red line. The green lines represent the three Extended Crystal Ball used to describe the Υ state distributions and the blue line represents the Double Exponential used to describe the underlying continuum. The numbers of $\Upsilon(nS)$ counts, the position, the width of the $\Upsilon(1S)$ and the χ^2/ndf are shown.

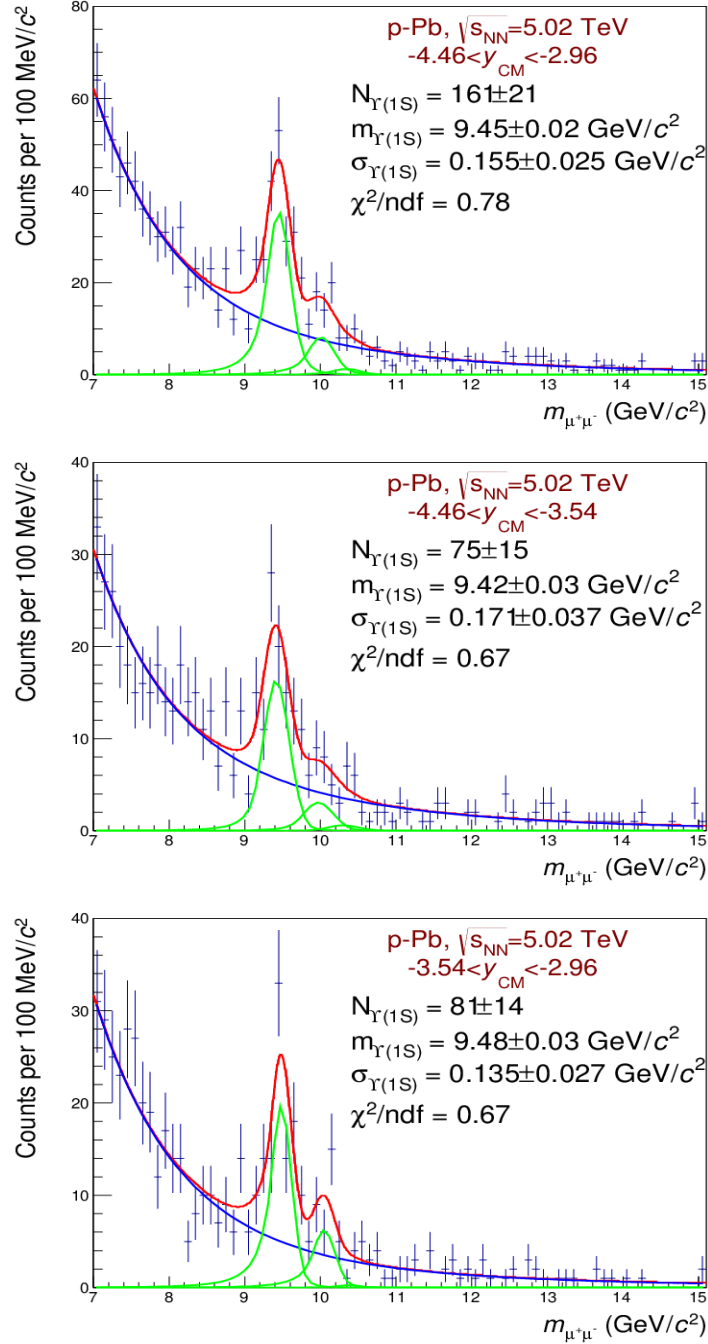


Figure 5.2: Fit procedure applied on the invariant mass distributions of opposite-sign dimuons in the different rapidity bins consider in this analysis at backward rapidity. The total fit function is represented by the red line. The green lines represent the three Extended Crystal Ball used to describe the Υ state distributions and the blue line represents the Double Exponential used to describe the underlying continuum. The numbers of $\Upsilon(nS)$ counts, the position, the width of the $\Upsilon(1S)$ and the χ^2/ndf are shown.

tion tails were poorly constrained by the data. Consequently, the tail parameters of the Extended Crystal Ball function were fixed according to the results from realistic Monte Carlo simulations. All parameters of the Double Exponential used for the background distribution were left free. The fit procedure described above was applied to the invariant mass distribution in different rapidity bins (Fig. 5.1 for forward rapidities and Fig. 5.2 for backward rapidities).

5.2.2 Fit Results

Table 5.1 summarizes the principal results from the fit procedure (the number of signal counts can be found in Fig. 5.1 and 5.1). The position of the $\Upsilon(1S)$ peak is found to be in good agreement with the meson mass ($9.460 \text{ GeV}/c^2$) [2] within relatively large statistical uncertainty. The width of the $\Upsilon(1S)$ peak is in agreement with that observed from realistic simulations within uncertainties. The signal-over-background ratio ($S/B(3\sigma)$) is of the order of the unity and the obtained significance ($\frac{S}{\sqrt{S+B}}(3\sigma)$) is always larger than 6. The large values of significance clearly ensures that the structure observed in the invariant mass range $[9 - 10] \text{ GeV}/c^2$ is not a statistical fluctuation. The number of $\Upsilon(1S)$ is obtained by integrating the CB2 used to describe the $\Upsilon(1S)$ peak. The considered statistical uncertainty on the signal counts is that on the integration and takes into account the covariance matrix of the function parameters.

This fit procedure also allows us to extract a number of $\Upsilon(2S)$ and $\Upsilon(3S)$ counts, since their normalizations are left free. In the case of the $\Upsilon(2S)$ in the rapidity ranges $-4.46 < y_{\text{cms}} < -2.96$ and $2.04 < y_{\text{cms}} < 3.54$ the significance is larger than 3. A summary of the Signal-over-Background ratio and the significance for the $\Upsilon(2S)$ can be found in Table 5.2. In the case of the $\Upsilon(3S)$ state, the significance is too low (< 1) to clearly separate the signal from the underlying background.

Collision	Rapidity	Counts	Mass (GeV)	Width (MeV)	S/B	Significance
p-Pb	$2.04 < y_{cms} < 3.54$	306 ± 35	9.45 ± 0.02	157 ± 22	0.9 ± 0.1	11.4 ± 1.6
p-Pb	$2.04 < y_{cms} < 2.96$	211 ± 30	9.46 ± 0.02	138 ± 25	0.8 ± 0.1	9.3 ± 1.6
p-Pb	$2.96 < y_{cms} < 3.54$	92 ± 18	9.44 ± 0.04	211 ± 47	1.1 ± 0.2	6.7 ± 1.7
Pb-p	$-4.46 < y_{cms} < -2.96$	161 ± 21	9.45 ± 0.02	155 ± 25	1.5 ± 0.2	9.3 ± 1.5
Pb-p	$-4.46 < y_{cms} < -3.54$	75 ± 15	9.42 ± 0.03	171 ± 37	1.2 ± 0.2	6.5 ± 1.6
Pb-p	$-3.54 < y_{cms} < -2.96$	81 ± 14	9.48 ± 0.03	135 ± 26	1.7 ± 0.3	6.8 ± 1.5

Table 5.1: The Signal count, mass position, width, signal-to-background ratio, significance for the $\Upsilon(1S)$ state obtained applying the fit procedure. Values are shown for the different rapidity ranges considered in the analysis.

Collision	Rapidity	S/B	Significance
p-Pb	$2.04 < y_{cms} < 3.54$	0.3 ± 0.1	4.1 ± 1.6
Pb-p	$-4.46 < y_{cms} < -2.96$	0.5 ± 0.2	3.5 ± 1.6

Table 5.2: The signal-to-background ratio, significance for the $\Upsilon(2S)$ state obtained applying the fit procedure. Values are shown for the two rapidity ranges considered in the analysis.

It is to be noted that the fit function doesn't always match perfectly the upper point of the $\Upsilon(1S)$ peak for some particular fits. The upper data point corresponds to a statistical fluctuation. Indeed the invariant mass distribution was shifted by half of a bin and the structure disappeared. After applying the shift, the number of $\Upsilon(1S)$ counts, the width of the peak and its position doesn't change significantly.

5.2.3 Systematic Uncertainties

In the previous section different hypotheses were made to perform the fit of the invariant mass distributions (choice of the background fit function, scaling of specific parameters for the $\Upsilon(2S)$ and $\Upsilon(3S)$ C2B and fixing of all C2B tails). In this section the systematic uncertainties related to these hypotheses are described. It was checked that all fits have a good χ^2 per degree of freedom ($\chi^2/\text{ndf} < 2.$) and provide a stable position and width for the $\Upsilon(1S)$ peak. The systematic studies are detailed for each of the sources as follows:

Background Fit Function: Two functions were used to describe the underlying

background, the Double Exponential (DE) and a Double Power-Law (DPL) which are defined as a sum of two exponential and power-law functions respectively. For each function, the lower and the upper bounds of the fit range were independently modified within the limits where the background is reasonably fitted ($[4 - 8]$ GeV/ c^2 and $[12 - 20]$ GeV/ c^2 , respectively). The systematic uncertainty resulting from this study ranges between 2% and 5% depending on the considered rapidity bin.

Mass Position: The positions of the CB2 used to describe the $\Upsilon(2S)$ and $\Upsilon(3S)$ distributions were fixed, thus leading to a potential source of systematic uncertainties. In order to estimate this uncertainty, the positions of these resonances were simultaneously shifted by various values between ± 0.05 GeV/ c^2 which corresponded to $\sim \pm 0.5\%$ of the mass of the $\Upsilon(1S)$. This range corresponded to the statistical uncertainty on the $\Upsilon(1S)$ position provided by the fit. The systematic uncertainties resulting from this study are about 1%;

Signal Width: The widths of the CB2 used to describe the $\Upsilon(2S)$ and $\Upsilon(3S)$ distributions were fixed. The related systematic uncertainties were estimated by scaling independently both widths by various values. Since the masses of the Υ mesons are known accurately from PDG, the value of the scaling factors can be chosen according to the uncertainty on the $\Upsilon(1S)$ width from the fits. The range for these factors was found to be $0.8 - 1.2$. The resulting systematic uncertainties are 1%.

Tail Parameters: The tails of the CB2 used to describe the Υ distribution line shape were fixed from Monte Carlo simulations. It was supposed that the same set of parameters can describe the tails of the CB2 used for each Υ states, since the decay kinematic of the three Υ states are close. For each CB2, the eight parameters of the two tails were multiplied independently by different factors. In MC simula-

tions, we can observe a bump on the left tail of the signal peak. For this reason, we varied the fitting range around the bump position and choose the factors in order to take into account the corresponding variation of the tail parameters. Depending on the rapidity bin and on the tail parameters the narrowest (widest) range was $0.9 - 1.10$ ($0.75 - 1.25$). These range were large enough to include statistical uncertainties on the fit. The obtain uncertainties amount to $2\% - 3\%$

Collision	Rapidity	$N_{\Upsilon(1S)}$
p-Pb	$2.04 < y_{cms} < 3.54$	305 ± 34 (stat.) ± 13 (syst.)
p-Pb	$2.04 < y_{cms} < 2.96$	211 ± 29 (stat.) ± 9 (syst.)
p-Pb	$2.96 < y_{cms} < 3.54$	94 ± 18 (stat.) ± 5 (syst.)
Pb-p	$-4.46 < y_{cms} < -2.96$	161 ± 21 (stat.) ± 9 (syst.)
Pb-p	$-4.46 < y_{cms} < -3.54$	76 ± 15 (stat.) ± 4 (syst.)
Pb-p	$-3.54 < y_{cms} < -2.96$	81 ± 13 (stat.) ± 5 (syst.)

Table 5.3: Summary of signal extraction of $\Upsilon(1S)$.

Collision	Rapidity	$N_{\Upsilon(2S)}$
p-Pb	$2.04 < y_{cms} < 3.54$	83 ± 23 (stat.) ± 10 (syst.)
Pb-p	$-4.46 < y_{cms} < -2.96$	42 ± 14 (stat.) ± 5 (syst.)

Table 5.4: Summary of signal extraction of $\Upsilon(2S)$. Values are given for the integrated rapidity bins, one for forward rapidity and other for the backward rapidity, that are possible to study.

Table 5.3 gives the final values from the signal extraction for $\Upsilon(1S)$. Central values and statistical uncertainties obtained in the different systematic uncertainty study (background, position and mass of $\Upsilon(2S)$ and $\Upsilon(3S)$ as well as CB2 tail parameters) were averaged and systematic uncertainties were summed in quadrature. Overall statistical (systematic) uncertainties range between $11\% - 20\%$ ($4\% - 6\%$). The largest source was related to the function chosen to describe the background. The results of signal extraction for $\Upsilon(2S)$ are also shown in table 5.4. The count number and the corresponding uncertainties were obtained with the same method as used for the $\Upsilon(1S)$. The largest systematic uncertainty arise from the fixing of the $\Upsilon(2S)$ and $\Upsilon(3S)$ widths.

5.3 Monte Carlo Simulation

A realistic Monte Carlo simulation was carried out to apply the correction for acceptance and efficiency ($A \times \epsilon$). The signal was obtained by generating $\Upsilon(1S)$ with a fast generator according to a parametrisation of their p_T and y distributions [3] and by forcing the resonances to decay into dimuons. For each considered run, the number of generated $\Upsilon(1S)$ accounted for 5% of the number of recorded CMUL trigger. Therefore the statistic uncertainty of each run was taken into account. The particle transport allowing the estimate of the detector response was provided by GEANT3 [4]. The actual alignment of the tracking chambers and the detector dead areas were then taken into account. The time dependence of the detector set up characteristics was also considered as the simulation was carried out on a run-by-run basis.

5.3.1 Signal Line Shape

An invariant mass distribution of OS dimuons from $\Upsilon(1S)$ decay was obtained with the realistic Monte Carlo simulation. The shape of the integrated signal distribution deviates from a simple Gaussian behaviour. Muon multiple scattering and energy loss fluctuations in the front absorber as well as residual mis-alignment of the tracking chambers led to a tail at low and high invariant mass. The use of an Extended Crystal Ball function was found to be necessary to describe the two tails (Fig. 5.3). The width of the simulated signal line shape varied between 102 and 197 MeV depending on the considered rapidity bins. The width from data could be described by such simulations. For each bin considered in this analysis, MC distributions were fitted and the obtained tail parameters were used in the fit.

A "bump" appears on the CB2 left tail at an invariant mass of about 8 GeV/c².

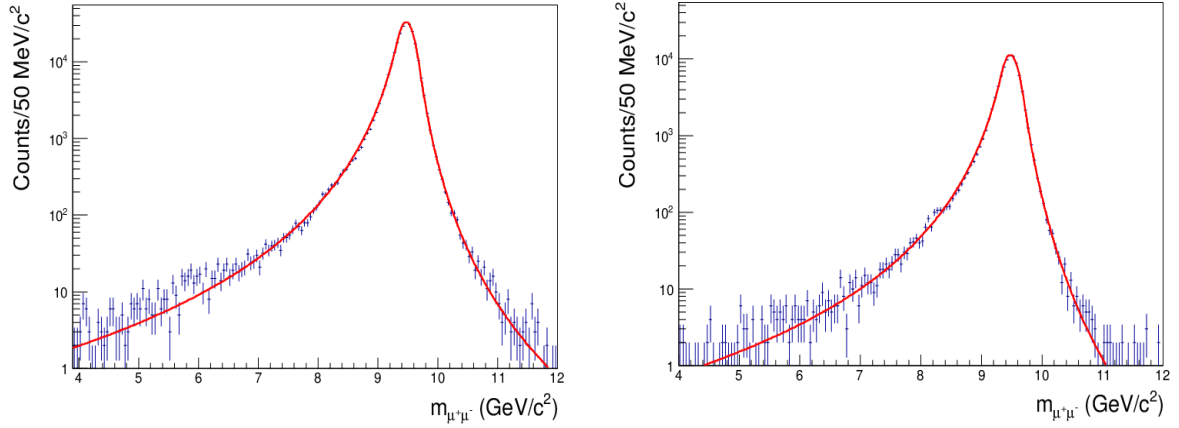


Figure 5.3: Run-by-run integrated signal distribution from Monte Carlo production fitted with an Extend Crystal Ball function for p-Pb period (left) and for Pb-p period (right) for the $2.5 < y_{\text{lab}} < 4$ rapidity range.

The lower bound of the fit was varied around $8 \text{ GeV}/c^2$ and the tail parameters were found to vary by 10% or 25% depending on the parameter. Therefore, the possible effect of such a structure on the signal count was taken into account in the systematic uncertainties.

5.3.2 Acceptance Efficiency Correction Factor

The product of acceptance times efficiency ($A \times \epsilon$) is defined as the probability for the decay muons from $\Upsilon(1S)$ produced in the geometrical acceptance of the detector to be correctly identified and reconstructed, taking into account the efficiency of the tracking and triggering systems. Fig. 5.4 shows the $A \times \epsilon$ for each run of the data taking periods. It is worth noting the low values for 17 low tracking efficiency runs at the end of the LHC13f period (run from 197142 to 197247 and from 197348 to 197388). This is due to high voltage trip in the detection elements towards the end of Pb-p data taking period. Table 5.5 summarised the obtained values of $\Upsilon(1S)$ $A \times \epsilon$ for the bins considered in this analysis.

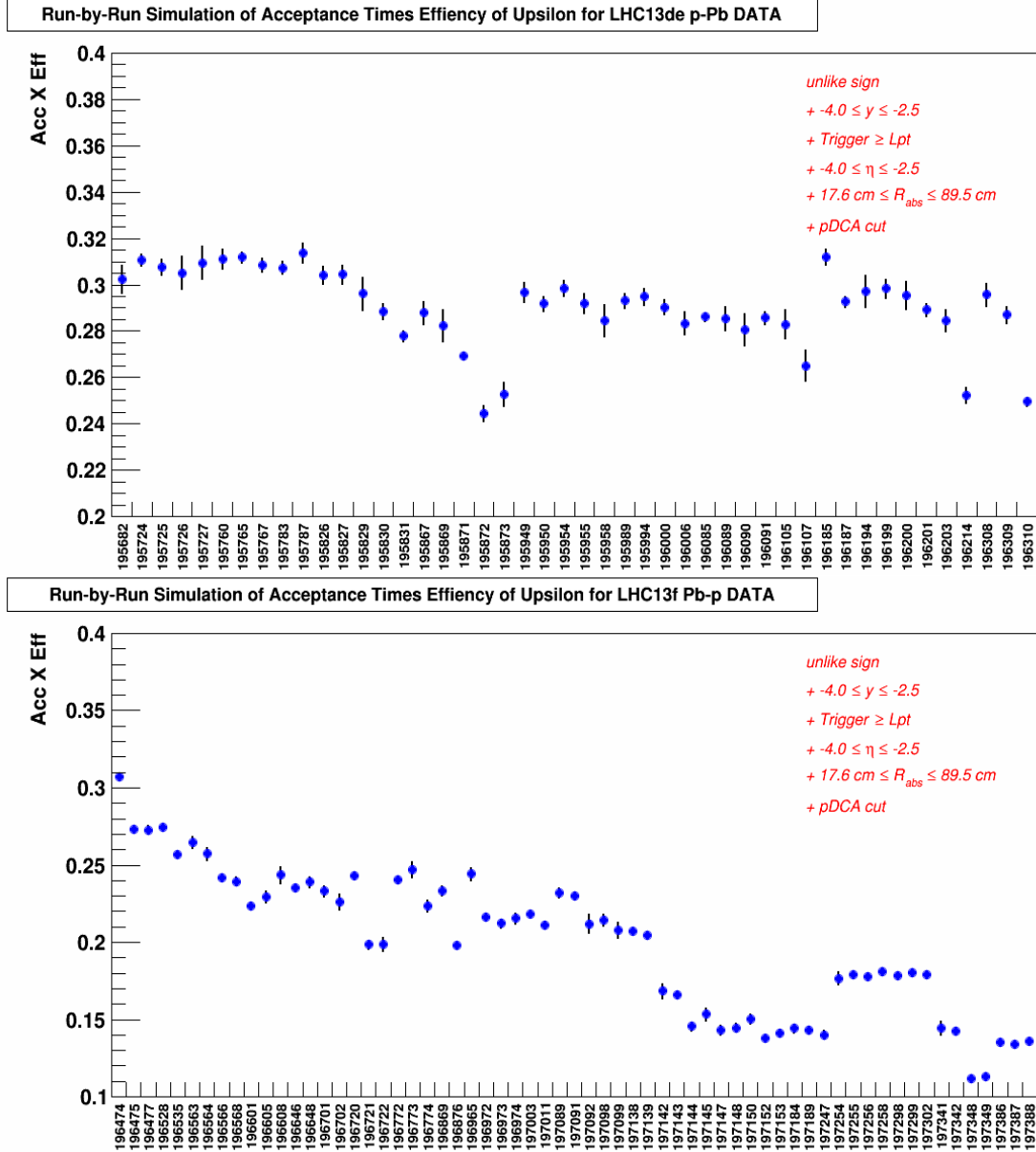


Figure 5.4: Run-by-run $A \times \epsilon$ for the LHC13d and LHC13e periods (top) along with that of LHC13f (bottom) in the $2.5 < y < 4$ rapidity range.

Collision	Rapidity	$A \times \epsilon$ (%)
p-Pb	$2.04 < y_{cms} < 3.54$	29.03 ± 0.20 (stat.)
p-Pb	$2.04 < y_{cms} < 2.96$	30.94 ± 0.22 (stat.)
p-Pb	$2.96 < y_{cms} < 3.54$	24.58 ± 0.39 (stat.)
Pb-p	$-4.46 < y_{cms} < -2.96$	20.06 ± 0.33 (stat.)
Pb-p	$-4.46 < y_{cms} < -3.54$	22.72 ± 0.44 (stat.)
Pb-p	$-3.54 < y_{cms} < -2.96$	17.21 ± 0.52 (stat.)

Table 5.5: The $A \times \epsilon$ of $\Upsilon(1S)$ for p-Pb and Pb-p period with statistical uncertainties.

The $\Upsilon(2S)$ $A \times \epsilon$ and the corresponding systematic uncertainties were evaluated with the same method and the same input distributions as for the $\Upsilon(1S)$. The observed differences between the $\Upsilon(2S)$ and $\Upsilon(1S)$ $A \times \epsilon$ are less than 0.5%.

5.3.3 Systematic Uncertainties

The estimate of the $A \times \epsilon$ factor depended on the $\Upsilon(1S)$ p_T and y shapes used as input distributions in the Monte Carlo simulation. In order to evaluate the sensitivity of the results on this initial choice, several estimates of the factor was performed with significantly different p_T and y parametrisations corresponding to pp and p-Pb collisions at different energies. The maximum spread observed among the results provide the uncertainties bin by bin. Obtained values are summarized in table 5.6.

Collision	Rapidity	Systematic Uncertainties (%)
p-Pb	$2.04 < y_{cms} < 3.54$	5
p-Pb	$2.04 < y_{cms} < 2.96$	6
p-Pb	$2.96 < y_{cms} < 3.54$	4
Pb-p	$-4.46 < y_{cms} < -2.96$	5
Pb-p	$-4.46 < y_{cms} < -3.54$	2
Pb-p	$-3.54 < y_{cms} < -2.96$	6

Table 5.6: Systematic uncertainties on $A \times \epsilon$ of $\Upsilon(1S)$ for p-Pb and Pb-p period. This one is related to the choice of the parametrisation used as input distribution for MC simulations.

Moreover, there are uncertainties due to the ability of simulations in reproducing the actual detector efficiency. The systematic uncertainty related to:

- tracking efficiency is 6% (4%) for the Pb-p (p-Pb) period;
- trigger efficiency is 2%;
- matching tracker track/trigger segment is 1%.

It is worth stressing that the $\Upsilon(1S)$ is assumed to be unpolarised in p-Pb collisions (and in pp collisions). Therefore, no polarisation related uncertainty was assigned to the $A \times \epsilon$ factor. All systematic uncertainties on $A \times \epsilon$ are uncorrelated with y_{cms} and the total systematic on it is between 6% and 9% depending on the rapidity bin.

5.4 Baseline: Proton-Proton Reference Cross Section

In order to measure the R_{pPb} of Υ at 5.02 TeV, we need the measurement of Υ production both in pp and p-Pb collisions at 5.02 TeV. However, the measurement of Υ production in pp collisions at 5.02 TeV does not exist. We also needed the $\Upsilon(1S)$ cross section for pp collisions in the proper rapidity intervals. So, an interpolation was performed using the data published by the LHCb Collaboration at the center-of-mass energies $\sqrt{s} = 2.76$ [5], 7 [6] and 8 [7] TeV. For each energy, LHCb provides measurements of the $\Upsilon(1S)$ rapidity-differential cross section times the dimuon branching ratio ($BR \times d\sigma/dy$) in the rapidity ranges $2 < y < 2.5$, $2.5 < y < 3$, $3 < y < 3.5$, $3.5 < y < 4$, $4 < y < 4.5$. For each energy, the LHCb results in adjacent bins were combined to obtain the cross section in the 5 ranges of interest for the ALICE proton-lead data analysis, shown in Table 5.7. The systematic uncertainties on the data were assumed to be fully correlated with rapidity.

The energy interpolation was performed separately for the five ranges and the result used for the computation of R_{pPb} in the corresponding rapidity range. The centers of the ranges labelled in the table as 1, 3 and 5 coincided with those of the R_{pPb} measurement. For the ranges labelled as 2 and 4, there was a shift of 0.035 units of rapidity, which was taken into account while calculating the systematic uncertainties.

Range ID	Interpolation range (central value)	R_{pPb} range (central value)
1	$2 < y < 3$ ($y = 2.5$)	$2.035 < y < 2.965$ ($y = 2.5$)
2	$2 < y < 3.5$ ($y = 2.75$)	$2.035 < y < 3.535$ ($y = 2.785$)
3	$3 < y < 3.5$ ($y = 3.25$)	$2.965 < y < 3.535$ ($y = 3.25$)
4	$3 < y < 4.5$ ($y = 3.75$)	$2.965 < y < 4.465$ ($y = 3.715$)
5	$3.5 < y < 4.5$ ($y = 4$)	$3.535 < y < 4.465$ ($y = 4$)

Table 5.7: Rapidity ranges used for the interpolation and for the measurement of the $\Upsilon(1S)$ nuclear modification factor. The central value of each range is also reported.

For each bin, the data were fitted according to several hypotheses for the shape, and the fit parameters are used to compute the cross section at $\sqrt{s} = 5.02$ TeV. Three types of shapes were used:

- two-parameter functions: linear ($p_0 + p_1 \sqrt{s}$), power law ($p_0 \sqrt{s}^{p_1}$) and exponential ($p_0 [1 - e^{\sqrt{s}/p_1}]$);
- a Leading Order Color Evaporation Model [8] (LO-CEM) calculation, which assumes that the $\Upsilon(1S)$ cross section at a given energy and rapidity is proportional to the cross section for $b\bar{b}$ production by gluon fusion, integrated between $\hat{s} = 4m_b^2$ and $\hat{s} = 4m_B^2$, where m_b is the beauty quark mass, m_B is the B meson mass and $\sqrt{\hat{s}}$ is the energy in the center of mass of the elementary process in which the beauty quark pair is produced.
- the energy and rapidity dependence of the total $b\bar{b}$ production cross section, computed in the FONLL [9] approach with the CTEQ6.6 set of parton distri-

bution functions. Three different shapes are obtained, defined by the energy evolution of the central value and of the upper and lower edges of the uncertainty band. The uncertainty band is obtained by varying the scales and masses within reasonable limits.

In the LO-CEM and FONLL approaches, the only free parameter of the fit is the normalisation. The ratio between the LHCb data and the theory as a function of energy is fitted with a constant function, and the interpolation is performed by multiplying the obtained parameter by the theoretical value at $\sqrt{s} = 5.02$ TeV.

For each rapidity range, the final result is obtained as the weighted average of the results obtained with all surviving shapes. The weight is given by the uncertainty on the result of the rescaled fit. The systematic uncertainty on the interpolated cross section has three components:

Fit Uncertainty: it takes into account the uncertainties on the data used for the interpolation and the degree of agreement of data with the fitting shapes; it is quantified by the average relative uncertainty on the results of the rescaled fits. It ranges from 7% to 11%;

Shape Uncertainty: it is related to the choice of the fitting shape; it is quantified by the maximum difference between the weighted average and the results of the individual fits. It ranges from 2% to 7%;

Range Uncertainty: the maximum difference between the differential cross sections when computed in the interpolation and measurement ranges, as predicted by the LO-CEM and FONLL models used for the interpolation. It is 1% for range 2 and 3% for range 4.

The fits obtained with three among the tested shapes are shown in Fig. 5.5 and 5.6, for the rapidity range $2 < y < 3.5$ and $3 < y < 4.5$ respectively.

The obtained results and uncertainties are reported in Table 5.8. The total un-

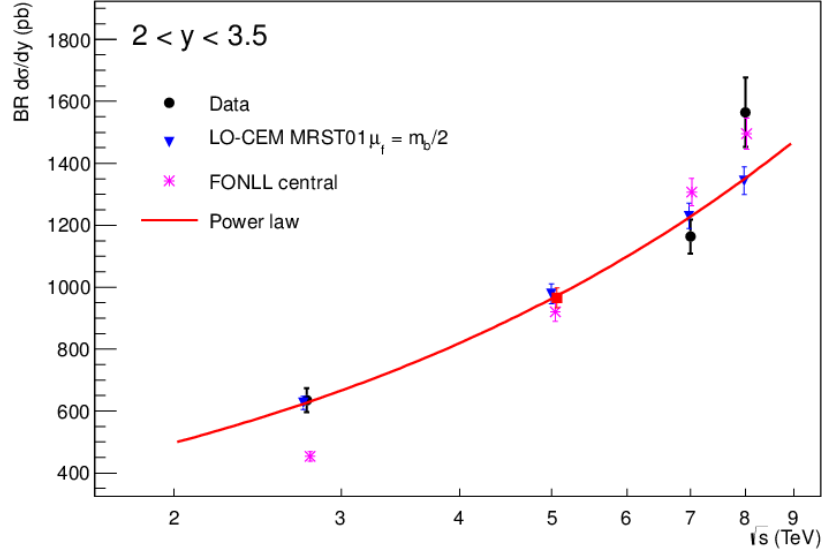


Figure 5.5: $\Upsilon(1S)$ cross section in $2 < y < 3.5$ as a function of energy [5, 6, 7]. Fits according to three different shapes are also shown, as well as the interpolated values at $\sqrt{s} = 5.02$ TeV.

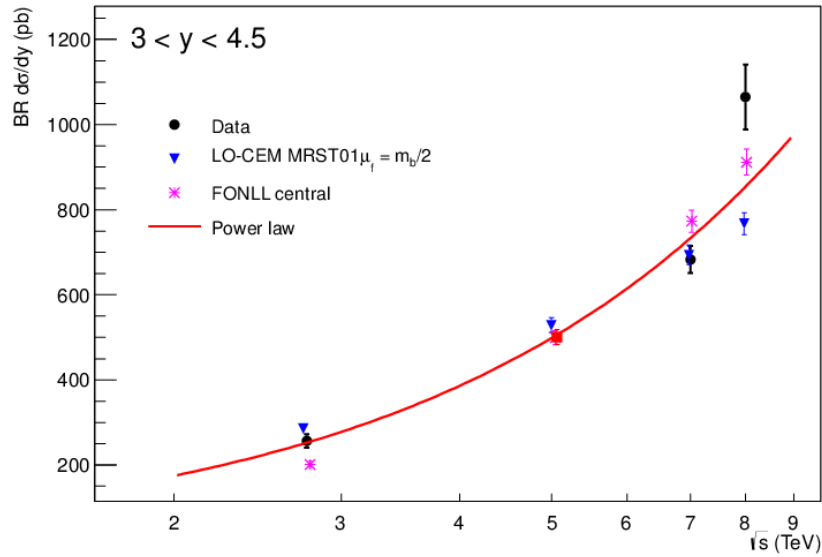


Figure 5.6: $\Upsilon(1S)$ cross section in $3 < y < 4.5$ as a function of energy [5, 6, 7]. Fits according to three different shapes are also shown, as well as the interpolated values at $\sqrt{s} = 5.02$ TeV.

certainty ranges from 7.5% to 13%. The uncertainties are quoted as uncorrelated with rapidity, in the assumption that the original correlation between the uncertainties in different ranges at the same energy is washed out by the interpolation procedure.

Range ID	Fit unc.	Shape unc.	Range unc.	$BR \times d\sigma/dy$ (pb)
1	6.8%	3.2%	-	1064 ± 80
2	7.5%	2.3%	1%	967 ± 76
3	10.6%	5.4%	-	751 ± 89
4	10.4%	3.2%	3%	513 ± 58
5	10.9%	7.4%	-	384 ± 51

Table 5.8: Interpolation uncertainties and results for the $\Upsilon(1S)$ cross section at $\sqrt{s} = 5.02$ TeV. The numbering of rapidity ranges is as defined in Tab. 5.7.

5.5 Summary of Systematic Uncertainties

Source of Systematic Uncertainties	Backward Rapidities $-4.46 < y_{\text{cms}} < -2.96$	Forward Rapidities $2.04 < y_{\text{cms}} < 3.54$
Signal extraction: $\Upsilon(1S)$	5%-6%(U)	4%-6%(U)
Signal extraction: $\Upsilon(2S)$	12%(U)	12%(U)
Input MC parametrization: $\Upsilon(1S)$	2%-5%(U)	4%-6%(U)
Input MC parametrization: $\Upsilon(2S)$	5%(U)	5%(U)
Tracking efficiency	6%(U)	4%(U)
Trigger efficiency	2%(U)	2%(U)
Matching efficiency	1%(U)	1%(U)
$\langle T_{AA} \rangle$	3.6%(C)	3.6%(C)
N_{MB}	1%(U)	1%(U)
$\sigma_{\text{pp}}^{\Upsilon(1S)}$ (interpolation)	11%-13% (U)	7%-12%(U)
\mathcal{L} (correlated)	1.6%(C)	1.6%(C)
\mathcal{L} (uncorrelated)	2.7%(U)	2.9%(U)

Table 5.9: Summary of the relative systematic uncertainties on each quantity entering in the calculations of the results. Type U uncertainties are given as a range including the smallest and the largest values observed in the bins considered in this analysis.

The summary of systematic uncertainties for $\Upsilon(1S)$ and $\Upsilon(2S)$ are given in Table 5.9. The uncorrelated uncertainties are denoted by U, while the correlated uncertainties are denoted by C.

5.6 Results

5.6.1 Υ Yield in p-Pb Collisions

The yield of $\Upsilon(1S)$ per rapidity unit is defined as:

$$\frac{dY_{\Upsilon(1S)}}{dy} = \frac{N_{\Upsilon(1S)}}{BR \cdot N_{MB} \cdot A \times \varepsilon \cdot \Delta y} \quad (5.1)$$

where:

- $N_{\Upsilon(1S)}$ is the number of $\Upsilon(1S)$ obtained from signal extraction. It depends on the considered rapidity bin;
- N_{MB} is the number of minimum bias p-Pb events. The total number of minimum bias event is obtained by re-normalising the measured number of CMUL events. The normalisations factor is 1129 ± 11 for p-Pb and 589 ± 6 for Pb-p;
- $A \times \varepsilon$ is the acceptance times efficiency correction. It depends on the considered rapidity bin;
- BR is the $\Upsilon(1S) \rightarrow \mu^+ \mu^-$ branching ratio (2.48 ± 0.05)%.
- Δy is the rapidity bin width.

The yield for each considered rapidity bin is given in Table 5.10 for $\Upsilon(1S)$ and Table 5.11 for $\Upsilon(2S)$. The statistical and systematic uncertainties were obtained by summing in quadrature the contribution from each source of Eqn. 5.1.

Collision Type	Rapidity Range	Yield $\times 10^6$
		$Y \pm \text{stat.} \pm \text{uncorr.} \pm \text{corr.}$
p-Pb	$2.04 < y_{\text{cms}} < 3.54$	$2.697 \pm 0.299 \pm 0.220 \pm 0.054$
p-Pb	$2.04 < y_{\text{cms}} < 2.96$	$2.827 \pm 0.386 \pm 0.250 \pm 0.057$
p-Pb	$2.96 < y_{\text{cms}} < 3.54$	$2.599 \pm 0.503 \pm 0.217 \pm 0.052$
Pb-p	$-4.46 < y_{\text{cms}} < -2.96$	$1.751 \pm 0.227 \pm 0.177 \pm 0.035$
Pb-p	$-4.46 < y_{\text{cms}} < -3.54$	$1.183 \pm 0.228 \pm 0.106 \pm 0.024$
Pb-p	$-3.54 < y_{\text{cms}} < -2.96$	$2.693 \pm 0.438 \pm 0.292 \pm 0.054$

Table 5.10: $\Upsilon(1S)$ yields per unit of rapidity obtained in p-Pb collisions at $\sqrt{s_{\text{NN}}} = 5.02$ TeV for each bin considered in the analysis.

Collision Type	Rapidity Range	Yield $\times 10^6$
		$Y \pm \text{stat.} \pm \text{uncorr.} \pm \text{corr.}$
p-Pb	$2.04 < y_{\text{cms}} < 3.54$	$9.46 \pm 2.60 \pm 1.33 \pm 0.83$
Pb-p	$-4.46 < y_{\text{cms}} < -2.96$	$5.81 \pm 1.91 \pm 8.56 \pm 0.51$

Table 5.11: $\Upsilon(2S)$ yields per unit of rapidity obtained in p-Pb collisions at $\sqrt{s_{\text{NN}}} = 5.02$ TeV for each bin considered in the analysis.

5.6.2 Cross Section Ratio of $\Upsilon(1S)$ and $\Upsilon(2S)$

The ratio $[\Upsilon(2S)/\Upsilon(1S)]$ of the invariant yields of $\Upsilon(2S) \rightarrow \mu^+\mu^-$ to $\Upsilon(1S) \rightarrow \mu^+\mu^-$ can be deduced by using Eq. 5.1 for both $\Upsilon(1S)$ and $\Upsilon(2S)$ and results in

$$[\Upsilon(2S)/\Upsilon(1S)] = \frac{N[\Upsilon(2S)]/(A \times \epsilon)_{\Upsilon(1S)}}{N[\Upsilon(1S)]/(A \times \epsilon)_{\Upsilon(2S)}}. \quad (5.2)$$

Here the branching ratio of the dimuon decay channel does not enter the calculation. Additionally, since the same data sample is used N_{MB} cancels out in the ratio. The systematic uncertainties on the ratios were obtained by quadratically combining the systematic uncertainties entering in each element of Eq. 5.2. Nevertheless, since the decay kinematics of the two Υ states are close, the systematic uncertainties on tracking, trigger and matching efficiency, estimated for the same detector in the same working conditions, cancel out in the ratio. The ratios of the invariant yields of $\Upsilon(2S) \rightarrow \mu^+\mu^-$ to $\Upsilon(1S) \rightarrow \mu^+\mu^-$ in p-Pb collisions at $\sqrt{s_{\text{NN}}} = 5.02$ TeV are:

$$[\Upsilon(2S)/\Upsilon(1S)]_{\text{pPb}}(-4.46 < y_{\text{cms}} < -2.96) = 0.258 \pm 0.091(\text{stat}) \pm 0.039(\text{syst}),$$

$$[\Upsilon(2S)/\Upsilon(1S)]_{\text{pPb}}(2.03 < y_{\text{cms}} < 3.53) = 0.273 \pm 0.081(\text{stat}) \pm 0.040(\text{syst}).$$

Within our large uncertainties, the ratio remains constant from backward to forward rapidity and it is impossible to conclude different CNM effects for the two states.

5.6.3 Nuclear Modification Factor of $\Upsilon(1S)$

The Nuclear Modification Factor in the p-Pb collisions R_{pPb} is defined by:

$$R_{\text{pA}} = \frac{\frac{dY_{\Upsilon(1S)}}{dy}}{\langle T_{\text{pA}} \rangle \cdot \frac{d\sigma^{pp}}{dy}} \quad (5.3)$$

where,

- $\langle T_{\text{pA}} \rangle$ is the average nuclear overlap function. In this analysis we consider all events without any selection on centrality. Therefore the $\langle T_{\text{pA}} \rangle$ is considered for the 0% – 100% VOM centrality class and is $9.83 \pm 0.35(\text{syst.}) \cdot 10^{-2} \text{ mb}^{-1}$ [10];
- and $\frac{d\sigma^{pp}}{dy}$ is the pp reference y-differential cross-section interpolated from LHCb results.

As stated previously, the following convention was defined: the rapidity is positive in the Muon spectrometer in p-Pb collisions and negative in Pb-p . This is motivated by the Bjorken x (x_{bj}) value of the probed gluon in the nucleus. Bjorken

x gives the momentum fraction carried by an inclusively observed particle in inelastic scattering. In p-Pb collisions, the Pb beam is coming from the Muon spectrometer, therefore $\Upsilon(1S)$ detected in the Muon spectrometer are produced from gluons in the Pb beam with a x_{bj} value of the order of $5 \cdot 10^{-5}$, while in Pb-p collisions the x_{bj} values of the gluons probed in the Pb beam are of the order of $2 \cdot 10^{-2}$.

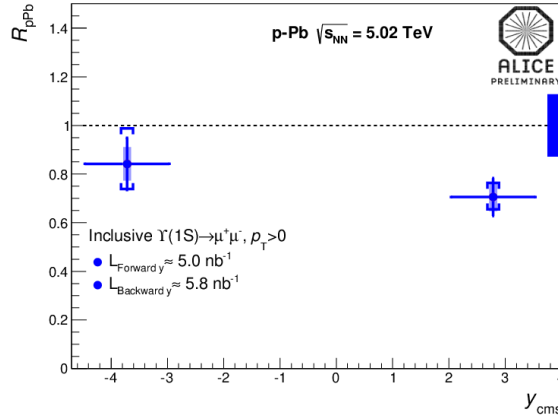


Figure 5.7: Inclusive $\Upsilon(1S)$ nuclear modification factor evolution as a function of y_{cms} .

The R_{pPb} of inclusive $\Upsilon(1S)$ measured by ALICE at $\sqrt{s_{NN}} = 5.02$ TeV and down to $p_T = 0$ is shown in Fig. 5.7 as a function of y_{cms} . The statistical uncertainties are represented by bars and the uncorrelated systematic uncertainties by full boxes. The fully correlated systematic uncertainty is represented by a box at $y_{cms} = 1$. At the backward rapidity the results are compatible with unity indicating small CNM effects. At the forward rapidity the suppressions is more pronounced.

Table 5.12 summarises bin-by-bin the different values of the R_{pPb} of inclusive $\Upsilon(1S)$. Both statistical and systematic uncertainties were obtained by summing in quadrature the related contributions of Eqn. 5.3.

The measured nuclear modification factor for the J/ψ in ALICE was, $R_{pPb} (2.04 < y_{cms} < 3.54) = 0.70 \pm 0.01(\text{stat.}) \pm 0.05(\text{syst.uncorr.}) \pm 0.03(\text{syst.part.corr.}) \pm 0.05(\text{syst.corr.})$ and $R_{pPb} (-4.46 < y_{cms} < -2.96) = 1.08$

Collision Type	Rapidity Range	R_{pPb}
		Value \pm stat. \pm uncorr. \pm corr.
p-Pb	$2.04 < y_{cms} < 3.54$	$0.704 \pm 0.078 \pm 0.080 \pm 0.025$
p-Pb	$2.04 < y_{cms} < 2.96$	$0.670 \pm 0.092 \pm 0.078 \pm 0.024$
p-Pb	$2.96 < y_{cms} < 3.54$	$0.873 \pm 0.169 \pm 0.127 \pm 0.031$
Pb-p	$-4.46 < y_{cms} < -2.96$	$0.861 \pm 0.112 \pm 0.131 \pm 0.031$
Pb-p	$-4.46 < y_{cms} < -3.54$	$0.777 \pm 0.150 \pm 0.124 \pm 0.028$
Pb-p	$-3.54 < y_{cms} < -2.96$	$0.905 \pm 0.147 \pm 0.146 \pm 0.032$

Table 5.12: Numerical values bin-by-bin measured in p-Pb collisions at $\sqrt{s_{NN}} = 5.02$ TeV. Statistical uncertainties are quoted as stat., uncorrelated systematic uncertainties are quoted as uncorr. and fully correlated uncertainties are quoted as glob.

$$\pm 0.01(\text{stat.}) \pm 0.09(\text{syst.uncorr.}) \pm 0.03(\text{syst.part.corr.}) \pm 0.07(\text{syst.corr.}) [11].$$

5.6.4 Forward-Backward Ratio $R_{FB}^{\Upsilon(1S)}$

In order to cancel out the pp reference cross section and its associated systematic uncertainties, the ratio of the nuclear modification factor measured at forward rapidity and that measured at backward rapidity is defined as follows.

$$R_{FB}^{\Upsilon(1S)}(2.96 < |y_{cms}| < 3.54) = \frac{Y_{\Upsilon(1S)}^{p-Pb}(3.47 < y_{lab} < 4)}{Y_{\Upsilon(1S)}^{Pb-p}(2.5 < y_{lab} < 3.07)}. \quad (5.4)$$

The $\langle T_{pA} \rangle$ also cancel out. The R_{FB} corresponds to the ratio of measured yields at forward and backward rapidities in the common rapidity $2.96 < |y_{cms}| < 3.54$ which corresponds to a rapidity range of $3.47 < y_{lab} < 4$ in p-Pb and $2.5 < y_{lab} < 3.07$ in Pb-p.

Our integrated $R_{FB}^{\Upsilon(1S)}$ in p-Pb collisions at $\sqrt{s_{NN}} = 5.02$ TeV and $p_T > 0$ is $0.95 \pm 0.24(\text{stat.}) \pm 0.14(\text{syst.})$. The systematic uncertainty was obtained by summing in quadrature the uncertainties on signal extraction, re-normalization of the number of CMUL events to that of MB events and $A \times \epsilon$ for both yields. The measured value of $R_{FB}^{J/\psi(1S)}$ from ALICE was $0.60 \pm 0.01(\text{stat.}) \pm 0.06(\text{syst.})$ [11]. Thus, the measured forward-backward asymmetry is more pronounced in the case of J/ψ .

5.7 Discussions

The inclusive $\Upsilon(1S)$ R_{pPb} integrated over the backward or forward rapidity ranges, are compared to several model calculations in Fig. 5.8. In the left panel, the results are compared to a next-to-leading order (NLO) CEM calculation using the EPS09 parameterization of the nuclear modification of the gluon PDF (commonly referred to as gluon shadowing) at NLO [12] (blue shaded band) and to a parton energy loss calculation [13] with (green shaded band) or without (red band) EPS09 gluon shadowing at NLO. In the case of the CEM+EPS09 calculation, the band reflects the uncertainties of the calculation that are dominated by the ones of the EPS09 parameterization [14]. In the cases of the parton energy loss model calculations, the bands represent the uncertainty from the EPS09 parameterization or from the parton transport coefficient and the parameterization used for the pp reference cross section. None of the calculations fully describe the backward and forward rapidity data and all tend to overestimate the observed $\Upsilon(1S)$ R_{pPb} . The parton energy loss with EPS09 calculation reproduces the $\Upsilon(1S)$ R_{pPb} at forward rapidity but tend to overestimate it at backward rapidity. The opposite trend is found for the parton energy loss calculation.

In the right panel, the results are compared to a calculation of a $2 \rightarrow 2$ production model ($gg \rightarrow \Upsilon g$) at leading order (LO) using the EPS09 shadowing parameterization also at LO [15]. Two bands are shown to highlight the uncertainties linked to two different effects. The extent of the blue band shows the EPS09 LO related uncertainties in the shadowing region, *i.e.* at low x_{Bj} . The red band shows the uncertainty in the EMC region, *i.e.* at high x_{Bj} . As the authors of [15] discuss, the gluon nPDF is poorly known in this region and the $\Upsilon(1S)$ R_{pPb} at backward rapidity could add useful constraints to the model calculations. It is worth noting that the two blue bands in the left and right panels of Fig. 5.8 differ by their cen-

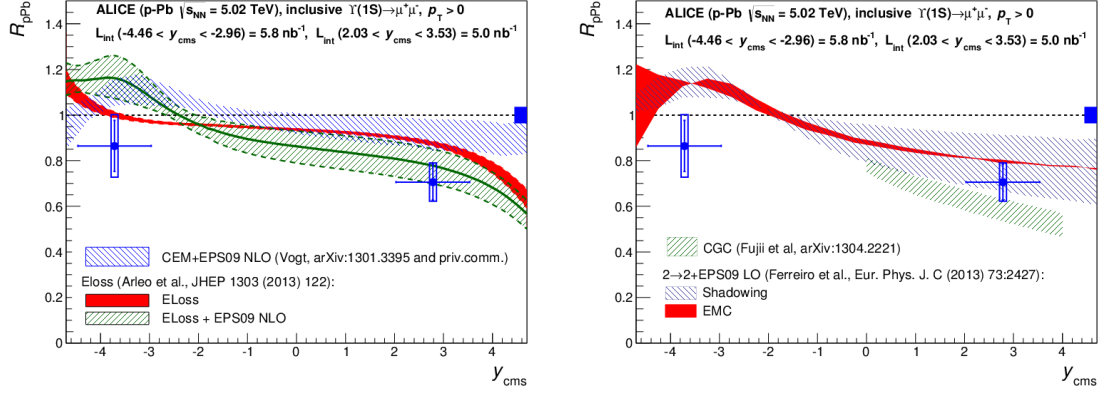


Figure 5.8: Nuclear modification factor of inclusive $\Upsilon(1S)$ in p-Pb collisions at $\sqrt{s_{NN}} = 5.02$ TeV as a function of rapidity. The vertical error bars represent the statistical uncertainties and the open boxes the uncorrelated systematic uncertainties. The full boxes around $R_{pPb} = 1$ show the size of the correlated uncertainties. Also shown are several model calculations: (left) parton energy loss [13] with and without EPS09 shadowing at NLO and CEM with EPS09 shadowing at NLO [12]; (right) CGC based [18] and CSM with EPS09 shadowing at LO [15].

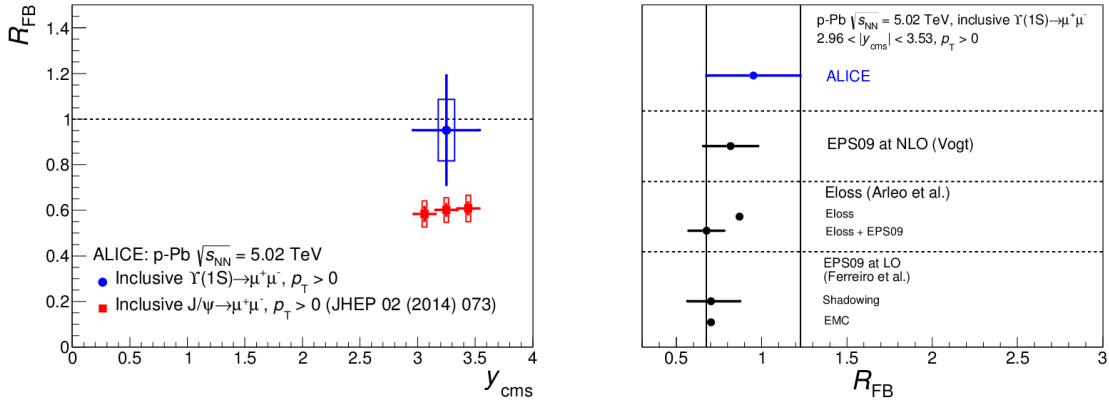


Figure 5.9: (Left) Forward to backward ratio R_{FB} of inclusive $\Upsilon(1S)$ yields compared to the J/ψ R_{FB} [11]. The vertical error bars represent the statistical uncertainties and the open boxes the uncorrelated systematic uncertainties. (Right) Inclusive $\Upsilon(1S)$ R_{FB} compared to theoretical model calculations. The statistical and systematic uncertainties for the experimental value are added in quadrature. For the model calculations, uncertainties are quoted when available.

tral curve and the extent of the uncertainties. The two approaches are similar and although the production models used are different, most of the difference comes from the usage of the NLO or LO EPS09 gluon shadowing parameterizations. It can be argued that using a NLO parameterization is more appropriate than a LO one, however it is worth mentioning that other gluon shadowing parameterizations [16, 17] (also at NLO) are available and that the uncertainty band of the EPS09 LO parameterization practically includes them. Therefore, the blue uncertainty band in the right panel of Fig. 5.8 can be considered as including the uncertainty due to different gluon shadowing parameterizations. The backward rapidity $\Upsilon(1S)$ R_{pPb} data does not support the strong gluon anti-shadowing included in the EPS09 parameterization. In the right panel of Fig. 5.8, a calculation based on the CGC framework coupled with a CEM production model is also shown (green shaded band) for positive y_{cms} . It is worth noting that, although this calculation only slightly underestimates the $\Upsilon(1S)$ R_{pPb} , it is not able to reproduce the J/ψ R_{pPb} in the same rapidity range [11].

The inclusive $\Upsilon(1S)$ R_{FB} is compared in Fig. 5.9 to the inclusive J/ψ R_{FB} [11] in the same rapidity range (left panel) and to several model calculations (right panel). In the rapidity range $2.96 < |y_{cms}| < 3.53$ the $\Upsilon(1S)$ R_{FB} is compatible with unity and is larger than that of the J/ψ . All models describe the data within the present uncertainties of the measurement.

5.8 Summary

The Υ production in p-Pb collisions at $\sqrt{s_{NN}} = 5.02$ TeV by the ALICE experiment was measured at the LHC. The $\Upsilon(1S)$ production cross section and nuclear modification factor is calculated in the rapidity ranges $-4.46 < y_{cms} < -2.96$

and $2.03 < y_{\text{cms}} < 3.53$ down to zero transverse momentum. At forward rapidity, R_{pPb} shows a suppression of $\Upsilon(1\text{S})$ production in p-Pb compared to pp collisions. At backward rapidity, the $\Upsilon(1\text{S})$ R_{pPb} is consistent with unity, suggesting a small gluon anti-shadowing. Models including the nuclear modification of the gluon PDF [15, 12] or a contribution from coherent parton energy loss [13] tend to overestimate our measured R_{pPb} and cannot simultaneously describe the forward and backward rapidity suppressions. A CGC based model [18] is in agreement with our Υ results at forward rapidity but cannot describe the J/ψ R_{pPb} [11]. The forward to backward ratio R_{FB} of the inclusive $\Upsilon(1\text{S})$ yields in $2.96 < |y_{\text{cms}}| < 3.53$ is compatible with unity within large uncertainties. Within our uncertainties, the $[\Upsilon(2\text{S})/\Upsilon(1\text{S})]$ ratio shows no evidence of different CNM effects on the two states. Additional measurements with higher statistics are needed to further constrain the models and extrapolate the CNM effects to Pb-Pb collisions.

Bibliography

- [1] B. Abelev et al. [ALICE Collaboration], Phys. Rev. Lett. **109** (2012) 252302 [arXiv:1203.2436 [nucl-ex]].
- [2] K. Nakamura *et al.* (Particle Data Group), J. Phys. G **37**, 075021 (2010).
- [3] F. Bossù, Z. Conesa del Valle, A. de Falco, M. Gagliardi, S. Grigoryan, G. Martinez Garcia, arXiv:1103.2394 [nucl-ex].
- [4] GEANT - Detector description and simulation tool, CERN Program Library Long Write-up W5013, CERN Geneva.
- [5] R. Aaij et al. [LHCb Collaboration], Eur. Phys. J. C **74** (2014) 2835.
- [6] R. Aaij et al. [LHCb Collaboration], Eur. Phys. J. C **72** (2012) 2025.
- [7] R. Aaij et al. [LHCb Collaboration], J. High Energy Phys. **1306** (2013) 064.
- [8] M. Gluck *et al.*, Phys. Rev. D **17**, 2324 (1978).
- [9] M. Cacciari et al., J. High Energy Phys. **1210** (2012) 137.
- [10] ALICE Collaboration, CERN-PH-EP-2012-306.

- [11] B. B. Abelev, et al., J/ψ production and nuclear effects in p-Pb collisions at $\sqrt{s_{NN}} = 5.02$ TeV, JHEP 1402 (2014) 073. arXiv:1308.6726.
- [12] J. Albacete, N. Armesto, R. Baier, G. Barnafoldi, J. Barrette, et al., Predictions for p+Pb Collisions at $\sqrt{s_{NN}} = 5$ TeV, Int. J. Mod. Phys. E22 (2013) 1330007. arXiv:1301.3395.
- [13] F. Arleo, S. Peigne, Heavy-quarkonium suppression in p-A collisions from parton energy loss in cold QCD matter, JHEP 1303 (2013) 122. arXiv:1212.0434.
- [14] K. Eskola, H. Paukkunen, C. Salgado, EPS09: A New Generation of NLO and LO Nuclear Parton Distribution Functions, JHEP 0904 (2009) 065. arXiv:0902.4154.
- [15] E. Ferreira, F. Fleuret, J. Lansberg, N. Matagne, A. Rakotozafindrabe, Υ production in p(d)A collisions at RHIC and the LHC, Eur. Phys. J. C73 (2011) 2427. arXiv:1110.5047.
- [16] D. de Florian, R. Sassot, Nuclear parton distributions at next-to-leading order, Phys. Rev. D69 (2004) 074028. arXiv:hep-ph/0311227.
- [17] D. de Florian, R. Sassot, P. Zurita, M. Stratmann, Global Analysis of Nuclear Parton Distributions, Phys. Rev. D85 (2012) 074028. arXiv:1112.6324.
- [18] H. Fujii, K. Watanabe, Heavy quark pair production in high energy pA collisions: Quarkonium, Nucl. Phys. A915 (2013) 1–23. arXiv:1304.2221.

Chapter 6

Summary and Outlook

In this thesis the data collected by the Muon Spectrometer of ALICE for pp, Pb–Pb and p–Pb collisions was analyzed. The quality assurance of the pp and Pb–Pb data was done to select the good quality runs for the physics analysis. Finally, the Pb–Pb and p–Pb data was analyzed to understand the hot and cold nuclear effect of the QCD matter on the Υ production.

6.1 Quality Assurance

In the pp collisions, the charge particle multiplicity was low. So, it was a good opportunity to validate the quality assurance procedure and understand the data and detector conditions. It was found that for large beam-gas events pDCA cut can be useful to eliminate those beam-gas tracks and to improve the data quality. In case of Pb–Pb collisions in LHC11h period, a total of 139 runs were selected from the ALICE logbook. Out of these 139 runs, 136 runs were reconstructed. Two runs 169683 and 170162 neither had the muon triggers nor the centrality triggers, but contained only the minimum bias triggers. The Muon tracking chamber efficiency

was good ($> 80\%$) and the variation in efficiency was $< 10\%$. The trigger chamber efficiency was stable during the period and the efficiency was above 95%. Finally 136 runs passed the quality assurance, but two of them did not contain opposite sign dimuon events.

6.2 Υ production in Pb–Pb

The inclusive $\Upsilon(1S)$ nuclear modification factor in Pb-Pb collisions at $\sqrt{s_{NN}} = 2.76$ TeV has been measured down to $p_T = 0$ in the $2.5 < y < 4$ rapidity and 0%–90% centrality ranges. A strong suppression of inclusive $\Upsilon(1S)$ was observed with $R_{AA}^{0\%-90\%} = 0.30 \pm 0.05(\text{stat.}) \pm 0.02(\text{uncorr.}) \pm 0.04(\text{corr.})$. Two centrality ranges were studied and the suppression is found to be more pronounced in most central collisions. The R_{AA} was also measured in two rapidity bins and, within uncertainties, no significant rapidity dependence was observed in the range probed by the Muon Spectrometer of ALICE.

The data were compared with the ALICE J/ψ results obtained in the same kinematic range. It was found that the $\Upsilon(1S)$ is more suppressed than the J/ψ and the difference of R_{AA} is particularly pronounced in the 0%–20% ($2.5 < y < 3.2$) centrality (rapidity) bin. The interpretation of these results is not straightforward due to the different sizes of the expected feed-down and (re-)generation effects for the two quarkonium states. The $\Upsilon(1S)$ R_{AA} was also compared with CMS data measured in the $|y| < 2.4$ rapidity region and down to $p_T = 0$. The inclusive $\Upsilon(1S)$ yield measured at forward rapidity by ALICE is more suppressed than that measured at mid-rapidity by CMS.

The theoretical predictions provided within a spectral function approach with complex potential, based on a plasma description by means of an anisotropic hy-

hydrodynamic formalism, not including regeneration effects and neglecting CNM effects, underestimate the suppression. Two transport models including CNM effects and a small regeneration component for bottomonia in a plasma evolving according to ideal hydrodynamics were also considered. They also underestimate the suppression measured by ALICE. These models also fail to reproduce the rapidity dependence of the observed suppression at LHC.

6.3 Υ production in p–Pb

The Υ production in p–Pb collisions also measured at $\sqrt{s_{NN}} = 5.02$ TeV. The $\Upsilon(1S)$ production cross section and nuclear modification factor is calculated in the rapidity ranges $-4.46 < y_{cms} < -2.96$ and $2.03 < y_{cms} < 3.53$. At forward rapidity, R_{pPb} shows a suppression of $\Upsilon(1S)$ production in p–Pb compared to pp collisions. At backward rapidity, the $\Upsilon(1S)$ R_{pPb} is consistent with unity, suggesting a small gluon anti-shadowing.

The theoretical Models including the nuclear modification of the gluon PDF or a contribution from coherent parton energy loss tend to overestimate our measured R_{pPb} and cannot simultaneously describe the forward and backward rapidity suppressions. A CGC based model is in agreement with our Υ results at forward rapidity but cannot describe the J/ψ R_{pPb} . The forward to backward ratio R_{FB} of the inclusive $\Upsilon(1S)$ yields in $2.96 < |y_{cms}| < 3.53$ is compatible with unity within large uncertainties. Within our uncertainties, the $[\Upsilon(2S)/\Upsilon(1S)]$ ratio shows no evidence of different CNM effects on the two states. Additional measurements with higher statistics are needed to further constrain the models and extrapolate the CNM effects to Pb–Pb collisions.

6.4 Future ALICE Upgrade Program

In order to improve the data quality at higher rates the ALICE Collaboration is planning to upgrade the current detectors. It is planned that after the second long shutdown in 2018 – 2019, the LHC will progressively increase its luminosity reaching an interaction rate of about 50 kHz, i.e. instantaneous luminosities of $L = 6 \times 10^{27} \text{ cm}^{-2} \text{ s}^{-1}$ in Pb–Pb collisions. The upgrade will include:

- (i) new ITS with a factor of 3 higher resolution between a track and its primary vertex;
- (ii) the replacement of TPC with Gas Electron Multiplier (GEM) detectors;
- (iii) improvement of the readout electronics for TPC, TRD, TOF, EMCal and Muon Spectrometer for higher data taking rate;
- (iv) new online systems (HLT, DAQ and CTP) for high data taking rates and increase the data mass storage to about 20 GB/s;
- (v) the completion of EMCal for nearly 2π coverage.

Furthermore, to increase the secondary vertex reconstruction capabilities for muon measurements installation of a Muon Forward Tracker (MFT) has been approved.

6.5 Outlook

The Υ production cross section is low. But in LHC we were able to measure the R_{AA} of $\Upsilon(1S)$ with reasonable precision using the ALICE Muon Spectrometer. To measure the suppression we needed the measurement of Υ in pp, Pb–Pb and p–Pb collisions at the same energy in same rapidity coverage. The production cross section of Υ was measured in Pb–Pb and p–Pb collisions with reasonable statistics. However, cross section in pp collisions could not be measured due to

lack of statistics. Instead pp cross section of Υ was taken from the result published by the LHCb collaboration in the same rapidity coverage. For the measurement of R_{AA} at 2.76 TeV (in case of Pb–Pb) LHCb results at 2.76 was used and an energy interpolation was done for the measurement of R_{pPb} at 5.02 TeV (in case of p–Pb) using the LHCb data at 2.76, 7 and 8 TeV. This was the first measurement of the R_{AA} of inclusive $\Upsilon(1S)$ in heavy-ion collision at forward rapidity, which could be used to constrain the theoretical understanding of the heavy-quark resonance production at LHC energies. In order to have a more precise understanding of the suppression and the feed-down from the excited states $\Upsilon(2S)$, $\Upsilon(3S)$ and χ_b , we need the direct measurement of suppression of the excited Υ states. Due to limited statistics, the suppression of $\Upsilon(2S)$ and $\Upsilon(3S)$ could not be measured in the forward rapidity. However, this will be possible with the improved statistics from run-2. In addition, finer centrality, rapidity and p_T binning with smaller uncertainties will also be possible, which in turn will further constrain the theoretical models. With the newly approved MFT, one may expect improvement of mass resolution also due to precise vertex determination.

The temperature produced in the Pb–Pb collisions at ALICE is ~ 500 MeV. This is quite high compared to the critical temperature (T_c), which is ~ 170 MeV. The dissociation temperatures of $\Upsilon(3S)$, $\Upsilon(2S)$ and $\Upsilon(1S)$ are $\sim 1.2 T_c$, $1.6 T_c$ and $4 T_c$ respectively and $\Upsilon(1S)$ is not expected to be suppressed, while $\Upsilon(2S)$ and $\Upsilon(3S)$ will be suppressed. This will allow us to estimate the temperature of the fireball from the ratios of $\Upsilon(2S)$ over $\Upsilon(1S)$ and $\Upsilon(3S)$ over $\Upsilon(1S)$.

The dissociation temperature for $\psi(2S)$ and J/ψ are $\sim 1.1 T_c$ and $2.1 T_c$ respectively. So, it is expected that at LHC energies both $\psi(2S)$ and J/ψ production is suppressed. However, as it is seen from the Pb–Pb data, the inclusive suppression of J/ψ is less than that of the $\Upsilon(1S)$. This can be explained by considering the

regeneration process, which is higher for the J/ψ due to high abundance of the $c\bar{c}$ pairs compared to $b\bar{b}$. However, it may be interesting to measure the ratio of R_{AA} of $\psi(2S)$ and $\Upsilon(3S)$ as a function of centrality, since both their dissociation temperatures are similar. If their ratio is close to unity, it would imply that $\psi(2S)$ production in Pb–Pb collisions does not have sizable contribution from recombination.

From the p–Pb data, it is observed that the forward-backward ratio $R_{FB}^{\Upsilon(1S)}$ is close to unity, which seems to indicate that the cold nuclear matter effects are small. However, the models incorporating the CNM effects fail to describe the observed R_{pPb} at the backward rapidities. This is because, all the models predict anti-shadowing at the backward rapidities, while the data do not seem to support this prediction.

The present study seem to indicate that Υ is the ideal probe to investigate the matter produced in the Pb–Pb collisions at LHC energies, since it has negligible contribution from recombination and CNM effects as compared to J/ψ .

Appendix

1. Crystal Ball Function

The Crystal Ball function ¹ consists of a Gaussian portion core and a power-law low-end tail, below a certain threshold. This is a probability density function and is commonly used to model various lossy processes in high-energy physics. The function itself and its derivative are both continuous. The Crystal Ball (CB) is given by:

$$f(x; N, \mu, \sigma, \alpha, n) = N \cdot \begin{cases} e^{-\frac{(x-\mu)^2}{2\sigma^2}}, & \text{for } \frac{x-\mu}{\sigma} > -\alpha \\ A \cdot (B - \frac{x-\mu}{\sigma})^{-n}, & \text{for } \frac{x-\mu}{\sigma} \leq -\alpha \end{cases}$$

where,

$$A = \left(\frac{n}{|\alpha|} \right)^n \cdot e^{-\frac{|\alpha|^2}{2}}$$

$$B = \frac{n}{|\alpha|} - |\alpha|$$

¹J. E. Gaiser, Appendix-F, SLAC-R-255 (1982), p. 178

$$N = \frac{1}{\sigma(C+D)}$$

$$C = \frac{n}{|\alpha|} \cdot \frac{1}{n-1} \cdot e^{-\frac{|\alpha|^2}{2}}$$

$$D = \sqrt{\frac{\pi}{2}} \left(1 + F_{\text{err}} \left(\frac{|\alpha|}{\sqrt{2}} \right) \right)$$

The α , n , μ and σ are parameters which are fitted with the data. The N and F_{err} is a normalization factor and error function respectively.

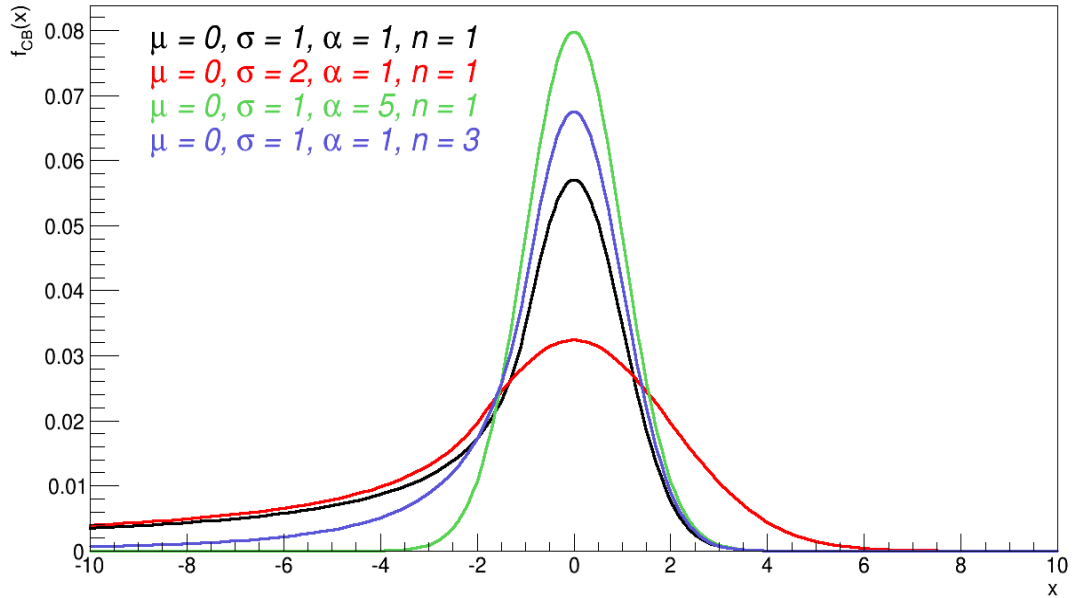


Figure 1: The Crystal Ball function with variation of parameters.

2. Extended Crystal Ball Function

The Extended Crystal Ball function (CB2) derives from the Crystal Ball function. While the CB has only one power-law tail for low x , the CB2 has two power-law tails (one for lower x and other for the higher x). The CB2 is defined by the following equation:

$$f(x; N, \mu, \sigma, \alpha, n, \alpha', n') = N \cdot \begin{cases} e^{-\frac{(x-\mu)^2}{2\sigma^2}}, & \text{for } -\alpha \leq \frac{x-\mu}{\sigma} < \alpha' \\ A \cdot (B - \frac{x-\mu}{\sigma})^{-n}, & \text{for } \frac{x-\mu}{\sigma} < -\alpha \\ C \cdot (D + \frac{x-\mu}{\sigma})^{-n'}, & \text{for } \frac{x-\mu}{\sigma} > \alpha' \end{cases}$$

where,

$$A = \left(\frac{n}{|\alpha|} \right)^n \cdot e^{-\frac{|\alpha|^2}{2}}$$

$$B = \frac{n}{|\alpha|} - |\alpha|$$

$$C = \left(\frac{n'}{|\alpha'|} \right)^{n'} \cdot e^{-\frac{|\alpha'|^2}{2}}$$

$$D = \frac{n'}{|\alpha'|} - |\alpha'|$$

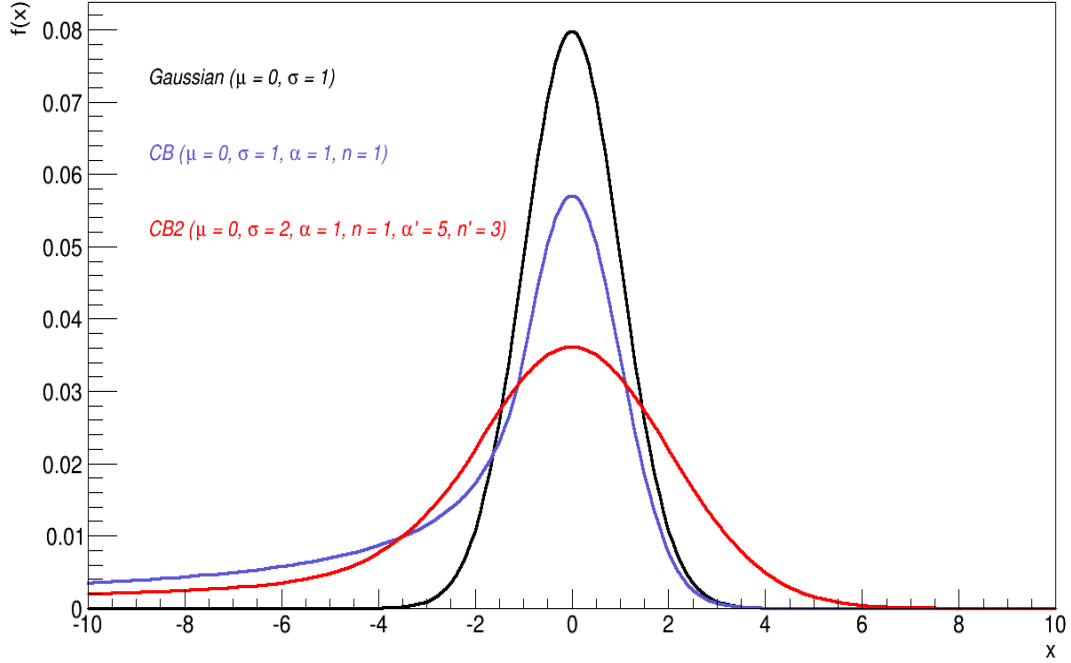


Figure 2: The Gaussian, CB and CB2 function.

3. Double Exponential Function

The double exponential function was used to fit the underlying continuum in the signal extraction and systematic uncertainty evaluation. This is the sum of two exponential function and can be written as:

$$f(x; \alpha, \beta, \gamma, \delta) = \alpha \cdot e^{\beta \cdot x} + \gamma \cdot e^{\delta \cdot x}$$

4. Double Power Law Function

The Double Power Law function is the sum of two power law function. It was used for the purpose of signal extraction. It can be written as:

$$f(x; \alpha, \beta, \gamma, \delta) = \alpha \cdot x^\beta + \gamma \cdot x^\delta$$